THESE DE DOCTORAT DE L'UNIVERSITE SORBONNE PARIS NORD
INSTITUT GALILEE

Mention **Sciences de l'Ingénieur**

Option **Sciences des Matériaux**

Présentée et soutenue publiquement par

Miguel SANCHEZ MENDEZ

Pour obtenir le titre de

Docteur de l'Université Sorbonne Paris Nord

Elaboration of mixed metal oxide nanoparticles for applications in photocatalysis

---

Directeur de thèse : Andrei KANAEV
Co-Directeur de thèse : Mounir BEN AMAR
Co-Encadrant : Mamadou TRAORE

Soutenue le 03/12/2021

Devant le jury composé de :

1	Samar ISSA	MCF HDR, Ecole de Biologie Industrielle	Rapporteur
2	Anatole KHODAN	Chief Scientist, Ac. Sci. Russie	Rapporteur
3	Christophe COLBEAU-JUSTIN	Professeur, Université Paris-Saclay	Examinateur
4	Andrei KANAEV	Directeur de recherche CNRS	Directeur de thèse
5	Mounir BEN AMAR	MCF HDR, USPN	Co-directeur de thèse
6	Mamadou TRAORE	MCF HDR, USPN	Co-encadrant de thèse
7	Mehrdad NIKRAVECH	Professeur, USPN	Invité
7	Alex LEMARCHAND	MCF, USPN	Invité

Laboratoire des Sciences des Procédées et des Matériaux CNRS UPR 3407

Acknowledgements

Si nos pintan como unos huevones

No lo somos

¡VIVA MÉXICO CABRONES!

"Molotov, 1997"

Acknowledgments

This PhD work was performed in the "Laboratoire des Sciences des Procédés et des Matériaux" (LSPM CNRS UPR 3407) of CNRS at the Université Sorbonne Paris Nord, and I would like to express my gratitude to the following people during all this years of work.

Primero que nada a mi familia que siempre me ha apoyado a lo largo de mi vida personal y profesional, a mi madre Leticia Méndez Romero por ser siempre mi guía, mi luz en mis peores momentos y siempre haberme dado ese amor maternal, a mi padre Miguel Sánchez Jiménez por siempre enseñarme algo nuevo a lo largo de mi vida, por haberme enseñado lo que es comenzar desde cero y ser humilde, a mi hermanita Matty Sánchez Méndez por siempre estar conmigo y seguirme en todas mis locuras. A mis mascotas: Januvia, Almendra, Punkito, Rocko, Coca y el Perico. A mi abuelo Don Félix Méndez Hernández

I would like to thank especially to my PhD supervisor Andreï Kanaev for accepting me and guide me through the doctorate, he is one of the best researchers I have ever known, my deeply respects to him as a person and as a mentor.

Thanks to my supervisors and persons who guided me in my experiments Mounir Ben Amar, Mehrdad Nikravech, Alex Lemarchand, a very and special thanks to Mamadou Traore for his patience, without him I would have been lost in many occasions and thanks to make the laboratory a more friendly environment.

Thanks to colleagues Christian Perruchot from Laboratoire Interfaces Traitements Organisation et Dynamique des Systèmes, Capucine Sassoye from Sorbonne Université, UMR 7574, Collège de France, Laboratoire de Chimie de la Matière Condensée de Paris, Mohamed Selmane from Fédération de Chimie et Matériaux de Paris-Centre (FCMat) for their help in characterization measurements on several prepared materials.

Thanks to the people in the lab that helped me in many occasions both technically and administratively like Greg, Chrystel, Nathalie, Sandrine, Daniel, Ludo, Nicolas, Valérie, Maria Konstantakopoulou, Rashid, Samir, Arlette, Dominique.

Thanks to my friends and colleagues in the LSPM laboratory like Ahmed, Enrico, Paola, Mine, Huyền, Tim, Annika, Amal, Lahcene, Julien, Roland, Zixian, Rania, Damia, Fatma, Hugo, Lino Martinez Soto, Ken Castillo Arvizu, Daniel, Iván, Marisol, Lounis, Assane, Rémi, Manoël. Jorge por haberme reclutado y haberme guiado a través del doctorado.

Grazie mille e dal cuore a Mary de Feudis per aver incontrato a una grande amica con cui parlare di qualcosa meno del lavoro e di darmi consiglie sulla vita, grazie mille anche a Sara D'Adorante, suo fratello Davide D'Adorante, a Magda Gomez, per la sua amicizia.

Thanks to the CONACYT for fundraising my PhD. To the Instituto Politécnico Nacional.

Acknowledgements

Gracias a mis amistades a lo largo de mi vida, pero tratando de ordenarlos por grupos los cuales consisten en haberlos conocido en etapas claves que me marcaron para llegar a la realización del doctorado, comienzo por esas amistades de la carrera como Gustavo Cedeño, Alejandro Carreón, Arturo Zecua, Jesús Resendiz, Hugo Cabrera, Sergio Cañete, Edgar, Ernesto, Carlos Sánchez, Cesar Mario, Jaime Osorio, Hector Sierra, Alejandro Gomez, Izuatl Garcia, Roberto, Israel Hernandez, Carlos Balcazar, Ricardo Arellano, Daniel Venegas.

Gracias a las amistades de la maestría como Isaac Capetillo, Alberto Soto, Edu Barragán, Solange Rivera, Luis Sánchez, Oscar García, Hugo Barragán, Susy Luna por haber todavía estado en contacto conmigo durante el doctorado.

Muchas gracias a mis amistades italo-venezolanas que conocí en una parte muy importante de mi vida que me marcó para hacer el doctorado y que hasta la fecha me han seguido apoyando, gracias a Carmen Espinosa, Nicola Furcolo, Giorgio Furcolo, Yleana Espinoza, Cesare Giovini, Christian Giovini, Claudio Giovini, Jessica Barbarino.

Gracias a mi hermana Alejandra Sánchez Roldán, a mis sobrinas Lilia Mendoza Sánchez y Leticia Mendoza Sánchez, a la familia Sánchez Ávila, un agradecimiento especial a mi tía Estela Méndez Romero (gracias por todo el apoyo), gracias a toda mi familia de Oaxaca, a la tía Carmela por esa inspiración.

Gracias a las siguientes personas: Alexandra Elbakyan, Aniceto Aguado, Anastacio Medas, Paco Gerlo, Alma Madero, Deborah Testa, Jorge Nitales, Larry Cañonga, Alcocer Delano, Aquiles Pico, Damesio Jon, Rosado de la Colina, Rosa Melcacho, Alma María, Memo Herdez, Benito Camelo, Jaime Costecho, Elver Galarga, Eleva Ginon, Lomas Turbadas y a Carmela Rosas. Esto va dedicado con mucho amor a la investigación.

Gracias a las diferentes amistades que he conocido en París, a Gabriela Castellanos por haberme apoyado en trámites de la beca y de la visa y de haber seguido en contacto en Francia.
A Mario Escobar, Cinthya Guerrero, Adilene Sánchez, Fernanda Hernández por todavía seguirme apoyando y ser parte de ese grupo especial.
Merci beaucoup à mes amis metalleux et bourrés, à Gretel Ortega, Ben, Patricia y Laurent Pinsivy, Stéphane Keldan, Pascale, Patrice et tous les autres amis avec qui je me suis saoulé.
A mis amistades que literalmente me salvaron en el Hellfest 2014, José Julio Hernández, Hugo Enrique Gil, Alexis Aguilar, Tulia de la Mora, Gringa, Saul, Margara Zayas, Edgar Cuauhtémoc, Victor (Force Fest Guadalajara)
A Gonzalo Pastrana y Lissette Rosales por haberme ayudado a sobrevivir durante el inhumano confinamiento de Marzo, Abril, Mayo 2020, gracias por esas conversaciones muy profundas e interesantes que me cambiaron la perspectiva de diferentes temas.
To my friends of the Mexican, German and Belgian residences in Cité Universitarie.
Gracias a Fernanda Machado por tu amistad y el cotorreo, a Claudia Avendaño por haberme "salvado" en el elevador y tu amistad, a Jose Antonio Beristain por haberme recibido cuando llegué a Paris. Muchas gracias a Pavel Rizo por esa ayuda brindada e invaluable y ser un guía en el doctorado.

Acknowledgements

Mis amistades especiales que fueron las primeras que hice llegando a Francia y que todavía me siguieron apoyando, los extraño mucho y con ustedes descubrí París y sus alrededores, tuvimos muchas pláticas interesantes y compartimos momentos irrepetibles y únicos, gracias a Ytel Garcilazo, Soledad López, Jorge Montero, Livier de la Rosa y Ziadany Mayoral.

Un agradecimiento especial a mis amistades que fueron las que me apoyaron desde un principio, que siguieron creyendo en mí y que fueron clave para que pudiera encontrar el doctorado, gracias a Kaleb Reséndiz (tantas anécdotas que tenemos y que ni siquiera nos la creemos), a Wendy Camacho por haberme mencionado sobre la feria doctoral de Francia y que me apoyó desde entonces, a mi asesor de la maestría, al Dr. Ángel de Jesús Morales Ramírez por su directo y continuo apoyo durante el doctorado y todos los invaluables consejos .

Special thanks to my friend Katya Pashova, for her friendship and to still be in contact with me through beers, to make the moments in the lab cooler and funnier, I still remember that time in the bar shouting at everyone майка ти да еба with Dimitar as well.

Agradecimiento muy especial a Kenzy Peña y a Franco Robles, por ese apoyo en lo académico y la vida social, les agradezco de mucho corazón esas veces que me apoyaron cuando yo estaba en mis peores momentos, esas excelentes comidas y platicas que tuvimos a lo largo del doctorado.

Especial agradecimiento a una de mis mejores amistades que he conocido, Carolina García, gracias por escucharme, por haberme apoyado en otro de mis peores momentos, gracias por toda la ayuda que me has brindado.

Especial agradecimiento a mi mejor amiga desde la preparatoria, mi amiga de viajes, conciertos y locuras, Amira Muhech, por platicar de todos esos temas en común que son extremadamente difíciles de conversar, gracias por todo el apoyo y sobre todo gracias darme motivación para superarme.

Table of Contents

Content

Figure Index

Introduction

Introduction

Nanotechnology is playing an increasing role in matter of science and research, as science continues to progress in the field of new technologies involving nanomaterials spreading in many industrials sectors such as engineering, medical, pharmaceutical, agriculture, environment and others. Among some specific applications, the use of titanium oxide in the production of cosmetics, surface coatings, some food products and water and air purifications while the research of silver nanoparticles has been directed to the field of disinfectants, bandages, and water purification systems. The worldwide investment in nanotechnology has been increasing since the 1997 reporting up to $US 4100 million in 2005 (Patila S. S. *et al.*, 2016) and up to $US 3 billion in 2017 expecting to exceed the $US 125 billion in 2024. (Intelligence, April 2018)

Environmental contamination has been addressed as one of the most important problems that need to be solved before there are serious consequences such as the contaminations of rivers and seas. Common pollutants in streams are chlorides and nitrates which are problematic if found in high concentrations as reported in indians rivers. (Jadhav S.D. *et al.*, 2013)

In the actuality, natural resources have reached high levels of pollution. Environmental pollution is a day-to-day problem that needs to be faced by developing and developed countries. Among all different types of pollution, air and water pollution contribute to the most important key in the balance of the ecosystems. Common pollutants are usually toxic organic compounds like dyes, detergents and surfactants, agrowastes like insecticides and herbicides, inorganic compounds, noxious gases; pathogens just to name a few. Hence the importance to address the problem with delicacy; the research community should focus into developing clean and green processes to degrade pollutants before they are discharged into the air and water contaminating the natural resources. (Vinu R. *et al.*, 2011)

Photocatalytic materials play a very important role in the elimination of toxic organic compounds. Photocatalysis is promotion of a light-activated reaction involving a semiconductor

illuminated with light of sufficient energy to excite electrons from the valence band to the conduction band. (Fox M. A. and Dulay M. T., 1993) During this process a redox-reaction can occur at the surface of the catalyst, this is oxygen reduction and water oxidation. The redox reactions result in the production of highly oxidizing reactive species (ROS) which have the ability to oxidize organic contaminants. (Min C. *et al.*, 2004) (Takashi T. *et al.*, 2009) (Konstantoinou, *et al.*, 2004)

Titanium dioxide nanoparticles have been widely used in the photocatalytic research ((Fujishima A. *et al.*, 1999) (Hashimoto K. *et al.*, 2005), since their effectiveness of the large surface area that can facilitate a fast rate of light-induced surface reactions. The problem with the use of only titanium oxide as a photocatalyst resides on the property that it only absorbs ultraviolet (UV) light. In the last decades, many studies have been conducted on the modifications of the material composition and structure, in order to improve the process efficiency and selectivity and extend the material activation to the visible spectral range ((Schneider J. *et al.*, 2014) (Zaleska A., 2008) There has been a strong investigation towards the strategy to change the optical absorption of TiO_2 towards the visible region by doping it with ionic species (Zhang H. *et al.*, 2009) But, the enhanced optical absorption does not always match to the photocatalytic activity in a previously inactive spectral range, meaning that the absorption spectrum of a photocatalyst does not match its corresponding photocatalytic activity spectrum.-An important method in this connection involves Ti cations replacement by other cations M, which can be referred as doping (at small level of insertion, ≤1 %) or mixing (at larger level). Moreover, when M forms oxides with a lower band gap energy (E_g) compared to that of TiO_2, there appears a potentiality for a desirable decrease of the process activation energy: $h\nu \leq 3.0$ eV. An insertion of vanadium (V) atoms, which pentoxide compound V_2O_5 has band gap energy of 2.2 eV, into the host matrix of TiO_2 solid creates such opportunities for the photocatalytic process improvement.

The problematic around the preparation of the photocatalysts with reproducible functional properties are the control of its homogenous composition at nanoscale, which is connected to

micromixing at the initial stage of the material preparation. Between different routes of the mixed metal oxides preparation, the sol-gel method occupies a special place in this connection (Brinker C. J. and Scherer G. W., 1990), (Pierre A. C., 1998). As it has been previously shown (Rivallin M. *et al.*, 2005) (Azouani *et al.*, 2010), this method can be adapted to achieve perfect micromixing at the particle nucleation stage, which is a key problem in size and homogeneity control of the dispersed solids (Bałdyga J. and Pohorecki R., 1995). In previous works carried out in our teams at LSPM, size-selected TiO_2 (Azouani *et al.*, 2007), N-doped TiO_2 (Azouani R. *et al.*, 2010) ZrO_2, (Labidi *et al.*, 2015) and $Zr_xTi_{2-x}O_2$ (Cheng *et al.*, 2017) nanoparticles with homogeneous composition have been prepared for an application in photocatalysis and catalysis.

In this work, we proposed to study synthesis of size-selective TiO_2-V_2O_5 nanoparticles by using the sol-gel method in a chemical reactor with ultra-rapid micromixing of the reacting solutions within a turbulent flow which will be favorable to obtain a homogenous solution and apply them for preparation of photocatalytic nanocoatings, which are active both under UV and visible light illuminations. The objective of this work is to synthetize TiO_2-V_2O_5 nanparticles with their respective precursors like titanium(IV) (TTIP) isopropoxide and Vanadium(V) oxytriisopropoxide (VOP) in n-propanol solvent. The reactor operates under the atmosphere and temperature control, which are important to achieve reproducibility of the nucleation-growth process kinetics and properties of the final material.

The PhD manuscript is organized in five Chapters, followed by General Conclusions and Perspectives.

Chapter 1 is devoted to the bibliography survey describing structural and physiochemical properties of TiO_2 and V_2O_5 solids, as well as of their mixed oxide TiO_2-V_2O_5 compositions. This Chapter introduced the nucleation-growth process in sol-gel method of the metal-oxo-alkoxy nanoparticles formation, laboratory micromixing reactor based on the turbulent fluids flow and in-situ monitoring of the preparation process by dynamic and static light scattering methods (DLS/SLS).

Introduction

Chapter 2 describes the principal techniques and methods used throughout this work for the prepared V-TiO_2 materials characterization. These analysis techniques include X-Ray Diffraction (XRD), Thermogravimetric Analysis (TGA) of mass loss and Thermal Differential Analysis (TDA) of heat flow, Transmission Emission Microscopy (TEM) and the DLS method.

Chapter 3 describes experimental studies of the nucleation and growth process of V_2O_5 and V-TiO_2 nanoparticles. The mixed oxide nanoparticles were prepared with different elemental compositions in the range of $0 \leq V/(V+Ti) \leq 1$. The in situ DLS/SLS measurements in the reactive solution of the micromixing reactor were applied in these studies using original optical fiber probe.

Chapter 4 presents the TDA-TGA, XRD and Raman characterizations of the prepared V-TiO_2 nanoparticulate materials with different elemental compositions in the range of $0 \leq V/(V+Ti) \leq 1$, as well as a discussion the obtained results.

Chapter 5 presents experimental results of the photocatalytic process of methylene blue (MB) decomposition in aqueous solutions under illumination with UVA and Visible Light lamps. The photocatalytic reactor is described. The photocatalysts were prepared in form of nanocoatings on glass beads of size-selective V-TiO_2 nanoparticles, which formation in the dedicated chemical reactor and subsequent heat treatments were studied respectively in Chapters 3 and 4.

The summary of the main obtained results and perspective of the accomplished studies are presented in General Conclusions and Perspectives. The list of publications, presentations at conferences issued of this work are given. References of previous scientific publication used in this work conclude the manuscript.

Chapter I Literature Review

This chapter will describe the structural properties of TiO_2, V_2O_5 and TiO_2-V_2O_5 as well as the technique to prepare the solid solution of the system. This first part is followed by the description of kinetics studies on the nucleation and growth processes of titanium and vanadium oxo-alkoxide nanoparticles synthesized manually or by using a micromixing sol-reactor. Finally, photocatalytic applications of materials are presented in the chapter.

1.1 Titanium oxide structural properties

1.1.1 Crystallographic structure

Titanium oxide, also known as titania, is an oxidation state of +4 of titanium, commonly used as a pigment in food coloring, sunscreens, and paints. Titanium oxide is an n-type semiconductor known for his broad band gap, and his surface, transport, and light absorption qualities. Titanium oxide has been lately part of a large focus of many different projects highlighting their photostable, photoactive properties,its advantages as the cost-effectiveness, and the stability. (Ramimoghadam D. *et al.*, 2014).

The titanium oxide TiO_2 presents three main different crystalline phases: anatase (tetragonal phase), rutile (tetragonal structure) and brookite (orthorhombic structure) (Jouanny I. *et al.*, 2010). In the Figure 1 (Jinfeng Z. *et al.*, 2014), it is shown the crystallographic structures

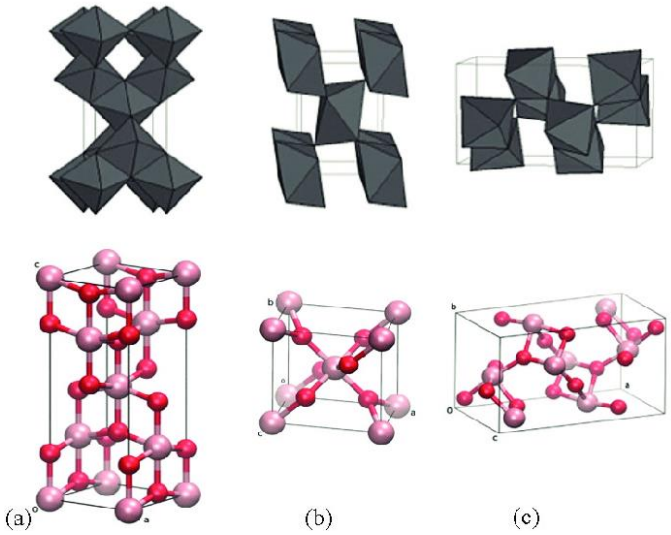

Figure 1 Crystallographic structures of TiO_2 (a) anatase, (b) rutile and c) brookite.

The anatase titanium oxide nanoparticles are the ones that are used more in the industry. This is mainly because of the properties of the material, like for example: the contribution of the titanium oxide nanoparticles on new functionalities to materials increasing the self-cleanliness pollution removal quality better through photocatalytic activation by UV light. (Constantinides, 2013)

In the Figure 2 it is shown the XRD patterns of prepared TiO_2 nanoparticles a) anatase b) rutile and c) brookite, the reference line patterns correspond to the JCPDS: No 21-1272 (Reyes-Coronado D. *et al.*, 2008)

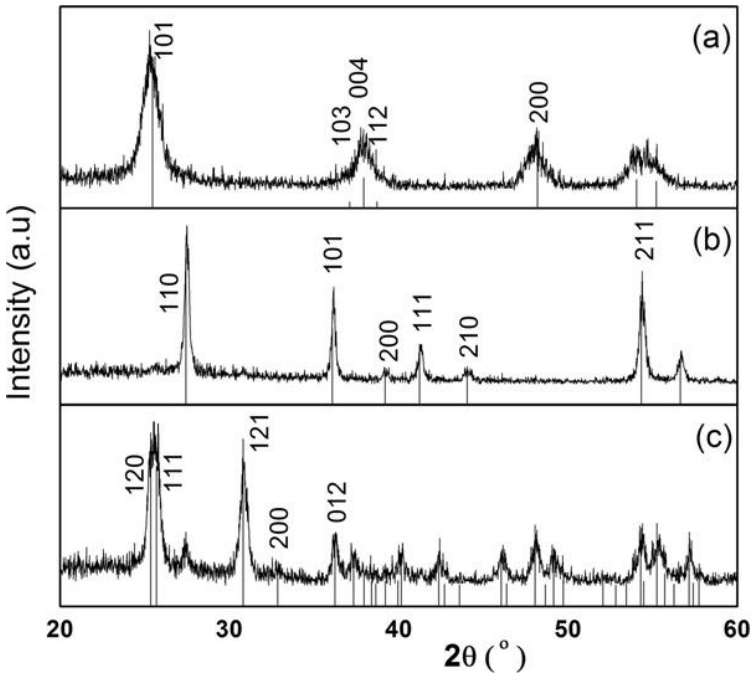

Figure 2 XRD patters of TiO_2 a) anatase b) rutile c) brookite (Reyes-Coronado D. *et al.*, 2008).

The band gap is the minimum amount of energy required for an electron to break free of its bound state. The band gap is important to keep in mind to study the photocatalytic power of the materials. The band gap of the TiO_2 can vary from 3.0 eV for the rutile phase and 3.2 eV for the anatase phase.

1.1.2 Vanadium oxide properties

Vanadium oxide or commonly named as Vanadia, is an inorganic compound that can be presented in various forms, that will depend on the oxidation state of the vanadium metal. Vanadium oxides, in special the following ones:

- Vanadium (III) oxide (vanadium trioxide) V_2O_3,
- Vanadium (IV) oxide (vanadium dioxide), VO_2,

Vanadium (V) oxide (vanadium pentoxide), V_2O_5.Vanadium oxides have gathered some special interest because of their application in catalysis such as cathode materials for batteries, electrochromic systems (Chernova N. A. *et al.*, 2009), optical switching devices (Boukhalfa S. *et al.*, 2012) and memory elements (Son M. *et al.*, 2011). Vanadium is a multivalent transition metal that can create different forms of stable oxides. In the following phase diagram (Figure 3), it is

emphasized the complexity of the vanadium-oxygen system (Hiraga K. and Hirabayashi M., 1975) (Rempel D. A. *et al.*, 2009) (Kosuge K., 1967) (Cao Z. *et al.*, 2015).

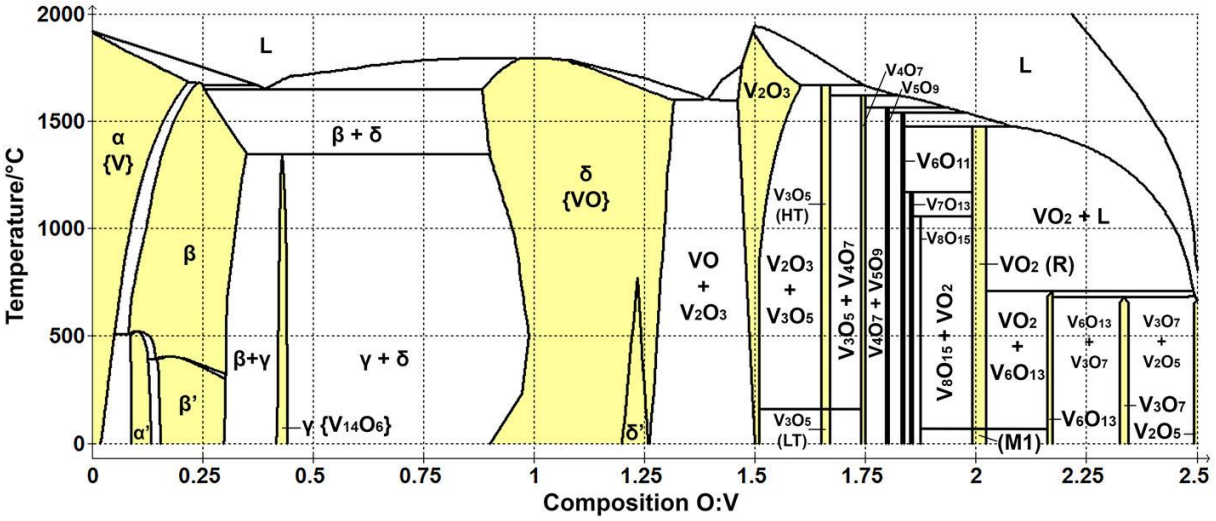

Figure 3 A vanadium-oxygen phase diagram (Shvets P. *et al.*, 2019).

In the following Figure 4, it is shown the XRD of the vanadium dioxide (VO_2) and vanadium trioxide (V_2O_3) at different temperatures as reported by (Pham V.-H. *et al.*, 2019)

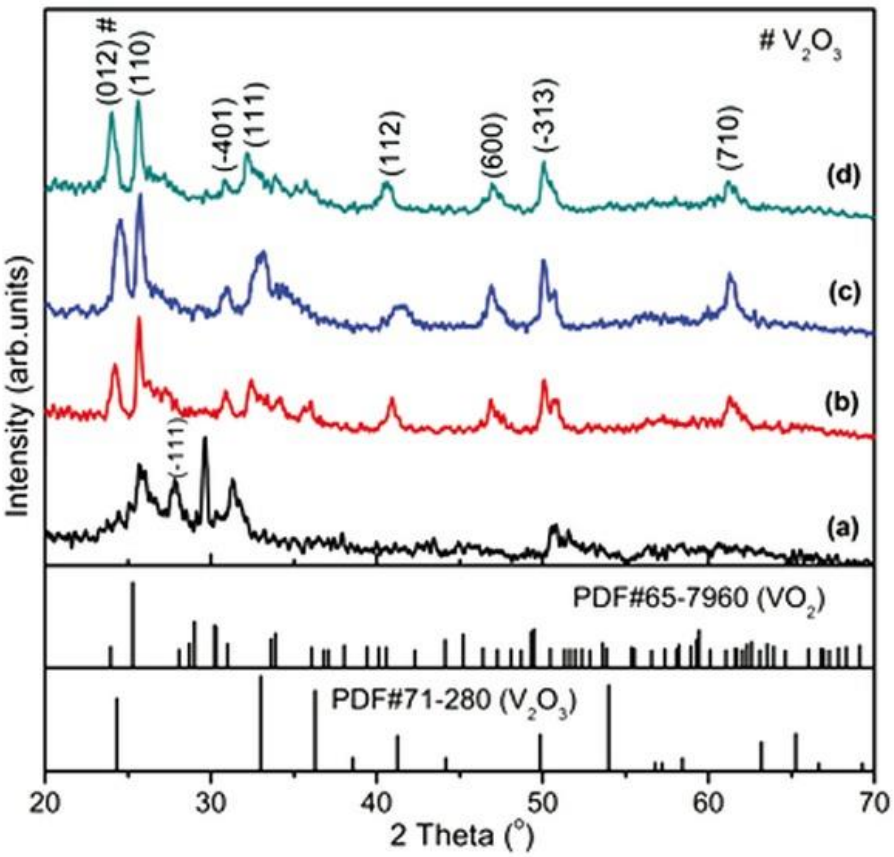

Figure 4 XRD patterns of VO2 (B) nanoparticles synthesized at different temperatures: (a) 100°C, (b) 150°C, (c) 180°C and (d) 200°C. (Pham V.-H. *et al.*, 2019).

V_2O_3 has a corundum structure with space group R_3c and lattice constants of a = 5.467 Å and α = 53.74° (rhombohedral notation) or a = 4.942 Å and c = 13.99 Å (hexagonal notation). (Andersson, 1954). Raman spectra have been reported for high and low temperature phases. (Kuroda N. and Fan H. Y., 1977).

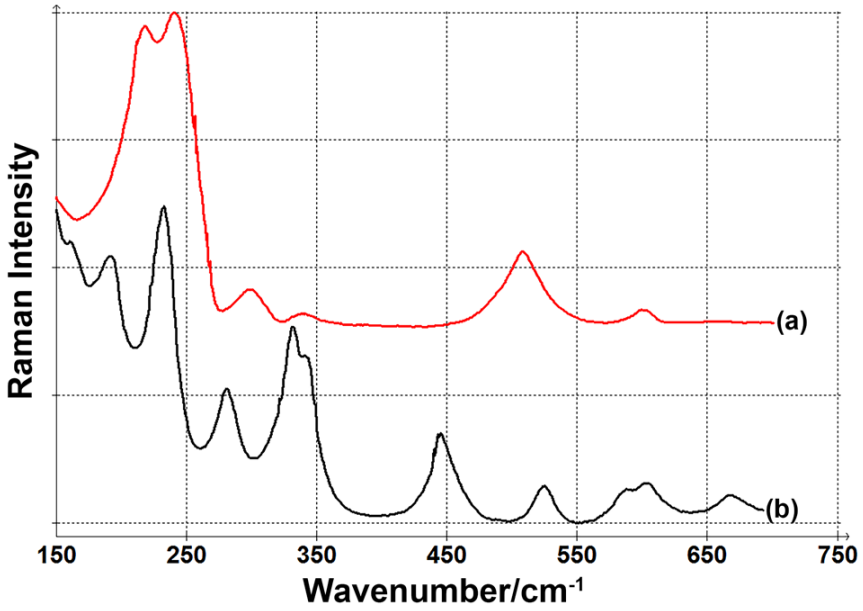

Figure 5 Raman scattering in corundum-type V_2O_3 (Shvets P. *et al.*, 2019).

The simple local spin density approximation (LSDA) is known to be unable to give a band gap for the insulating phases of V_2O_3 (Mattheiss L. F., 1994). But according to (Guo Y. *et al.*, 2014) they report a calculated band gap of 0.63 eV which agrees well with the experimental optical gap of 0.50–0.66 eV.

VO_2 (M1). Its space group is P21/c, a = 5.35 Å, b = 4.52 Å, c = 5.38 Å, and β = 115.2° (Andersson, 1956). A reversible phase transition into a metallic state is observed at temperatures above 68°C. In this state, the lattice is tetragonal and rutile resemblance.

For the rutile structure, there are four Raman-active modes (A1g + B1g + B2g + Eg). All of them are linked with the only motion of oxygen atoms

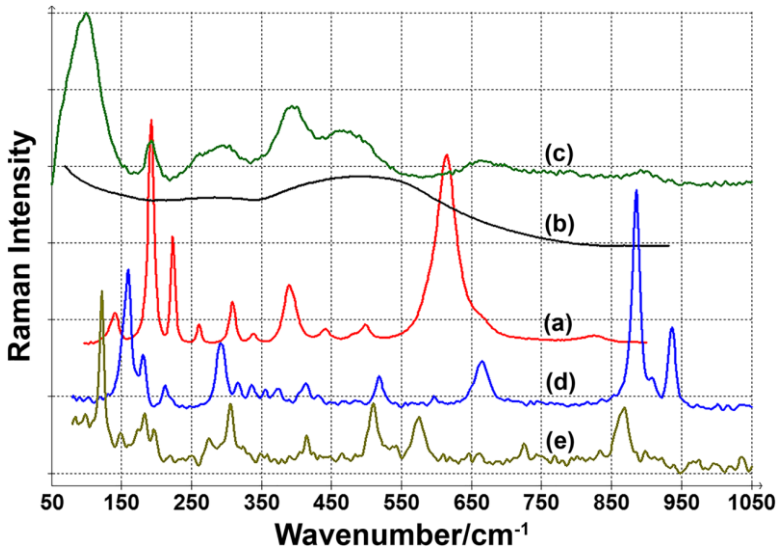

Figure 6 Raman scattering in VO_2 polymorphs: (a) VO_2 (M1), (b) VO_2 (R), (c) VO_2 (B), and VO_2 (A) measured at 30°C and 220°C (Shvets P. *et al.*, 2019).

The optical bandgap obtained in the VO_2 is of 0.6 ± 0.05 eV for monoclinic (M1) phase. (Lee S. *et al.*, 2015)

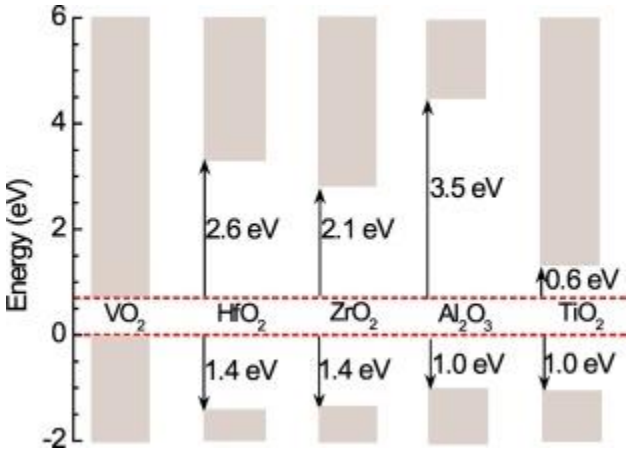

Figure 7 Schematic band alignment diagram of VO2 with different dielectrics (Zhang Z. *et al.*, 2019).

From all these types of vanadium oxides, V_2O_5 is the most stable and common form of vanadium (V) oxide, also known as vanadic anhydride.

V_2O_5 presents an orthorhombic structure with lattice parameters a = 3.563 Å, b = 11.510 Å, c = 4.369 Å (Fiermans L. *et al.*, 1980). Orthorhombic α- V_2O_5 is built-up by layers of corner-sharing and alternating edge VO_5 square pyramids linked together through Van der Waals interactions. (Verrelli R. *et al.*, 2018)

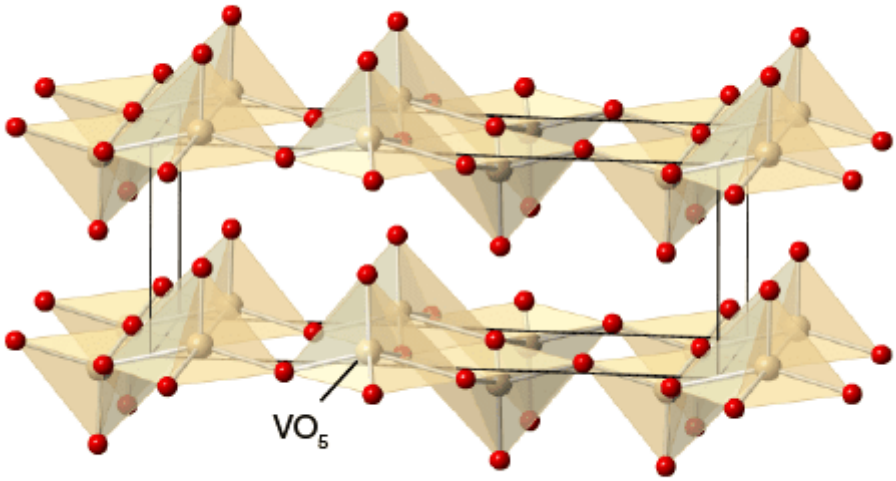

Figure 8 Structure of V_2O_5 consists of linked VO_5 square base (ChemTube3D, 2008-2021).

Vanadium oxide (VO_x) has been a relevant subject lately due to a multitude of catalytic reactions (Wachs I.E. *et al.*, 2003). It is used widely as a catalyst in many industrial chemical reactions due to its many applications which can be used like the following:

- In manufacturing some ceramics and some kinds of alloys,
- In optical applications like for example, the manufacture of laser crystals,
- For applications which involves nanofiber and nanowire (Dispersions, 200-2021).

In Figure 9, it is shown the XRD pattern which can be indexed to JCPDS no. 60-0767 (Chan Y.-L. *et al.*, 2014)

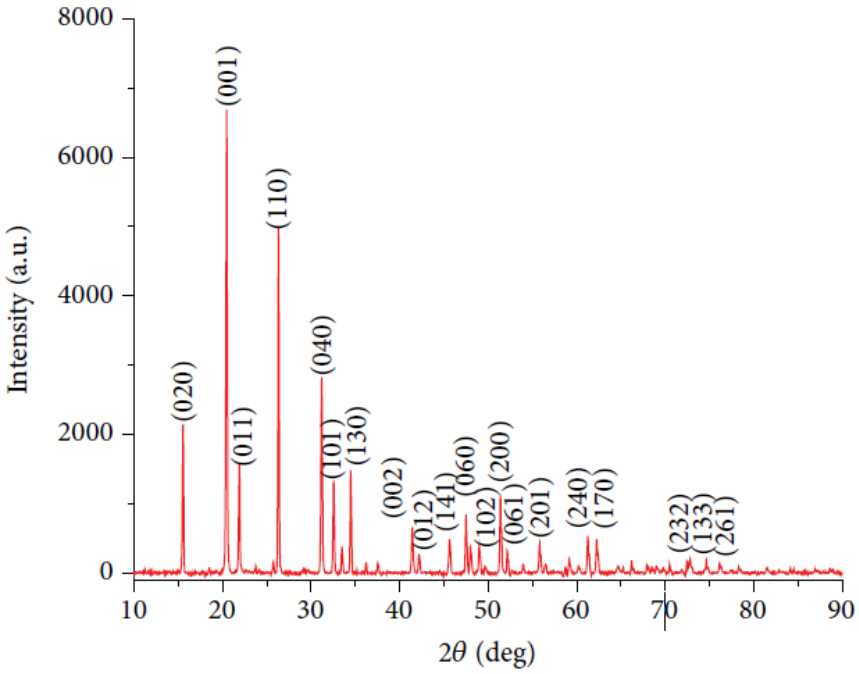

Figure 9 XRD Patten of V_2O_5 nanoparticles.

There are at least six polymorphs of V_2O_5, including α-V_2O_5, β-V_2O_5, δ-V_2O_5, γ′-V_2O_5, ζ-V_2O_5, and ε′-V_2O_5. The most common one is α-V_2O_5, which crystallizes into orthorhombic space group (Pmmn) with lattice constants of a = 11.51 Å, b = 3.564 Å, and c = 4.368 Å (Enjalbert R. and Galy J., 1986)

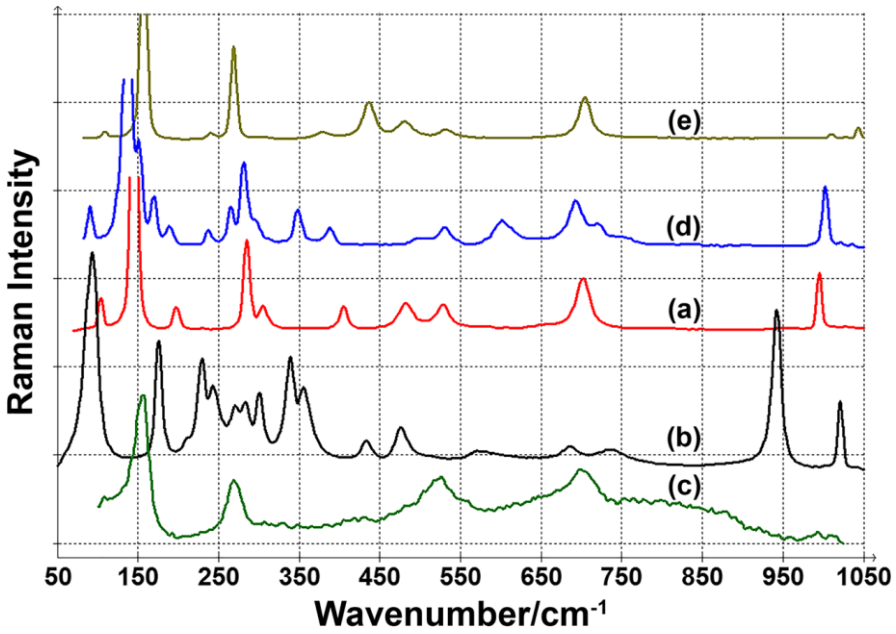

Figure 10 Raman scattering in V_2O_5 polymorphs: (a) α-V_2O_5,(b) β-V_2O_5, (c) δ-V_2O_5, (d) γ′- V_2O_5, and ε′-V_2O_5 (Shvets P. *et al.*, 2019).

The optical absorption coefficients of V_2O_5 single crystals using incident polarized light with wavelengths in the range of 0.47–1.8 µm and unpolarized light with wavelengths from 1.5 to 7.5 µm. Fundamental absorption was observed at incident photon energies of 2.15, 2.22 and 2.17 eV for E - a, E - b and E - c, respectively. (Kenny N. *et al.*, 1966)

1.1.3 Mixed-oxide Titanium – Vanadium: V-TiO_2

In contrast to a composite material, which is a combination of two or more single constituent materials, the mixed-oxides solids are characterized by high composition homogeneity at nanoscale due to the fine elemental mixing. An example of such $Zr_xTi_{1-x}O_2$ solid prepared via bottom-up approach, i.e. from nanoparticle to bulk solid could be given (Cheng *et al.*, 2017). These materials, including homogeneously doped solids (avoiding ad-element clustering) and solid solutions, have different chemical and/or physical properties and are merged to constitute a new material with properties different from the original individual materials. In some particular cases, when dopant concentration exceeds the solubility limit, the material segregation can lead to a nanocomposite, which constitutes a special class of composite materials, largely used in many industrial applications such as transport structures and buildings, some of the properties and characteristics that are optimized are the strength and stiffness, the resistance against fatigue, the resistance to corrosion and helping into the manufacturing of complex shapes (see e.g. Mousumi, 2020). In this connection, mixing of vanadium and titanium precursots could lead to the novel class of V-TiO_2 solids with high composition homogeneity. Furthermore, estimates based on the experimental band gap energy of 2.05 eV obtained in V_2O_5 semiconductor showed that visible light with wavelength < 605 nm may be used to initiate photocatalytic reactions in this material (Jianhua L. *et al.*, 2006). Therefore V-TiO_2 solids could be expected to possess a reduced activation energy in a photocatalytic process compared to that of prestine TiO_2.

Previous studies of the mixed oxide and nanocomposite V-TiO_2 solids are numerous but not conclusive. In particular, optimum material composition in the photocatalytic process in connection with the morphology and elemental composition at nanoscale has not been yet provided, although the reasons of high effectiveness and underlying mechanisms were discussed. (Bettinelli M. *et al.*, 2007) have synthetized V-doped TiO_2 photocatalysts via a modified sol–gel process reporting that the activity was significantly affected by preparation conditions. They have explained that the surface vanadium caused the pollutant (methylene blue, MB) degradation, while the bulk vanadium did not influence the activity. At the same time, surface vanadium also caused the deactivation, suggesting the presence of poisoning effects. (Chang P-Y. *et al.*, 2009) have reported a red-shift of the absorption onset energy of V-TiO_2 nanoparticles with V content up to ~2 wt% prepared via sol-gel method. They have observed a moderate decrease of the MB decomposition rate under UV light illumination (305 nm). At the same time, a significant increase of the decomposition rate was observed under the solar simulator illumination with the optimum attained at the V content of 0.5-1 wt%. Lin and Lin (Lin W-C. and Lin Y-J., 2012) have shown that an optimal vanadium content of 5% enhanced the pseudo first order photocatalytic kinetics of MB degradation under the visible light irradiation, which was explained by the migration of photogenerated electrons to vanadium, thus improving the electron-19 hole separation. Moreover, V-doping of TiO_2 increased the crystal grain size affecting specific surface areas of powders and extended the material absorption in the spectral range of 400-800 nm. (Khan H. and Berk D., 2013) have reported a successful incorporation of V_5^+ ions into the TiO_2 crystalline lattice that resulted in a decrease of the band-gap energy and a decrease in photogenerated electrons and holes recombination rate. These and other recent studies on V-TiO_2 have indicated an optimal material composition for the best photocatalytic performance (Al-Mamun M.R. *et al.*, 2019). While optimisation of the photocatalyst composition and morphology advances, the relevant problem concerns development of the photocatalysis preparation process (Meramo S. I. *et al.*, 2018) (Stoller M. *et al.*, 2019). A chemical reactor with ultrarapid micromixing of the reactive fluids has been previously developed in our group for the mass-fabrication of size-

selected pure, doped and mixed metal oxide nanoparticles, and its performance has been demonstrated on the preparation of TiO_2, $ZrxTi_1$-xO_2 photocatalytic nanoparticles and nanocoatings (Azouani R. *et al.*, 2009) (Azouani R. *et al.*, 2010) (Cheng K. *et al.*, 2017) (Cheng K. *et al.*, 2018). In this work, we extend studies to the photocatalytic activity of V-TiO_2 nanoparticles prepared via sol-gel method in the dedicated chemical reactor.

1.2 Preparation Methods

1.2.1 Sol-Gel Method

The application of novel methods for the synthesis of some materials was modified with the coming of the Sol-Gel method. (Brinker C. J. and Sherer G.W., 1990) (Kakihana M., 1996) have defined Sol-Gel as the obtaining of oxide materials by preparing a sol and removing the solvent. Sol-Gel is defined as a dispersion of solid particles in a liquid phase where the particles are small enough to remain suspended, having at least one dimension in the range of 1-100 nm, in a liquid medium. A gel is a colloidal system, wherein the continuous phase is a liquid and the dispersed phase a solid, wherein the solid phase forms a network that entraps and immobilizes the liquid part. A gel is formed when the homogeneous dispersion present in the initial sol rigidifies, this process is called gelation, preventing the inhomogeneous development of the material.

Particle growth can take place by diffusion across boundaries to form agglomerates. The surface conditions between particles will determine the diffusion process of molecules or atoms. Besides, the presence of impurities on the surface can change the mechanism of the processes. Glass for example is an amorphous colloid with silica and aluminum, which is formed when silica modifies its surface by interaction with aluminate ions, exchanging $Si(OH)_4$ ions for $Al(OH)_4$ ions.

Figure 11 Behavior of the particles during the Sol-Gel process.

The Figure 11 shows in more detail how the particles are arranged in such a way that from a sol, it becomes a gel.

To form a colloid, it is necessary to stabilize it so that the particles do not agglomerate. The propensity of colloids to agglomerate is due to attractive van der Waals forces. Colloids can be stabilized by charge and entropically (by energy), a stabilization mechanism that involves the presence of lyopophilic polymeric molecules, or molecules that have a high affinity for the solvent, which adsorb on the surface of the colloidal particles and prevent them from agglomerating.

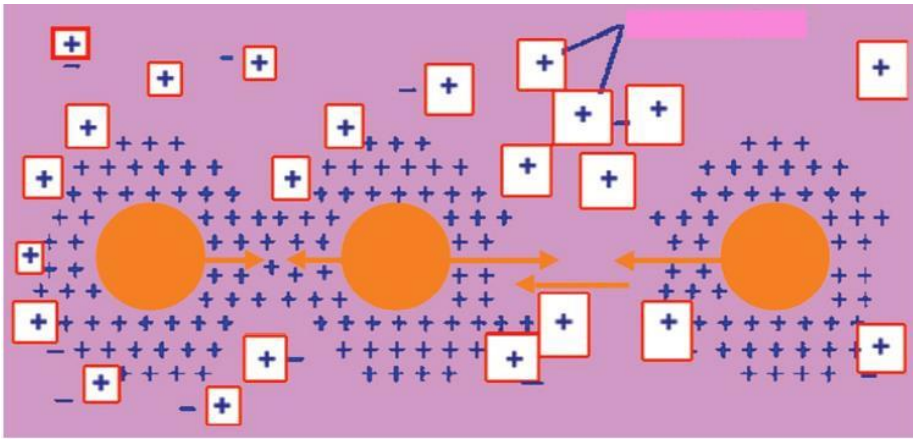

Figure 12 Colloid Stabilization.

A sol can be transformed into a colloidal gel, which is a rigid network interconnected with pores of submicrometer dimensions and polymeric chains whose length is larger than a micrometer, by passing through the so-called gel point. This point is where the sol abruptly changes from a viscous liquid state to a solid phase called gel. As the gelation consists of stabilizing the bonds between the

sol particles to form the three-dimensional solid network, the sol-gel process can be used to obtain ceramic powders and films.

There are three main routes depending on whether the precursor is an inorganic salt in aqueous solution, an aggregate solid formed by colloidal subunits, or an array forming agent in organic solution.

Ionic precursor solutions are destabilized by changes in solution, such as pH or temperature, initiating the process of hydrolysis followed by condensation. In the second case, it starts with aggregates of colloidal particles in a solvent (suspension), to which some electrolyte or other solvent is added, with the possibility of subsequent re-aggregation. The fundamental physicochemical effect in operation is the change in the surface zeta potential and hence the interaction energy between the colloidal particles. Metal alkoxides are the most important precursors for the formation of oxides.

In the sol-gel process the following parameters are of vital importance, since they are responsible for the final physicochemical characteristics of the synthesized nanomaterials:

- The H_2O/alkoxide ratio (hydrolysis ratio),
- The pH of the reaction,
- The influence of the solvent,
- The gelation time,
- Reaction temperature,
- The different alkyl groups of the type of precursor used.

In the sol-gel process there are several steps: mixing, gelling, aging, drying and sintering (Kakihana M., 1996) (Vennila R. *et al.*, 2014) (Miller H. *et al.*, 2000).

Mixing:

The possibility of designing unique materials is one of the aspects of the sol-gel process that are considered most important, especially when done by polymerization of a metal-organic compound to form a polymer gel. The key is to design the appropriate monomer that will polymerize to form the M-O-M structures. M(OR)n metal alkoxides - where M is the metal and R an alkyl radical - meet this requirement. These reactions occur simultaneously and are usually incomplete, but the desired oxide is achieved. The result of the reactions is a colloidal dispersion of extremely small particles (1-2 nm) that eventually form an entangled three-dimensional network of the corresponding inorganic oxide.

Hydrolysis and polycondensation can be accelerated or slowed down using the corresponding acid or base catalyst.

$H_2O + M – O – R \rightarrow H – O – M + R – OH$ (Hydrolysis reaction)

At low pH the particles aggregate to form polymeric structures, whereas at high pH the particles increase in size; this effect is due to the variation of solubility with surface curvature and pH. Depending on the amount of water present, the hydrolysis reaction may be completed or stopped when the metal is partially hydrolyzed. In the case where various cations are used to form mixed oxide networks, an initial step is necessary to form the mixed complex. When the alkoxy precursors have different hydrolysis rates, a pre-hydrolysis of the alkoxysilane is preferable.

The oxolation is when two partly hydrolysis precursors react with each other and they release a water molecule in the process, the reaction of the of the oxolation can be written as it follows:

$M – O –H + H –O –M \rightarrow M –O –M + H_2O$

The general form of this equation is the following:

$(RO)_{n-x}M(OH)_x + (RO)_{n-Y}M(OH)_Y \leftrightarrow (RO)_{n-x}(OH)_{x-1}M–O–M(OH)_{y-1}(OR)_{n-y} + H_2O$

The alkoxolation is when the precursor molecule and the partly hydrolyzed precursor reacts, the reaction mechanism of the alcoxolation can be written as follows:

M – O – H + M – O – R → M – O – M + R – O – H

After the complex operation of polymerization, sol formation, and gelation, a microporous gel with high specific surface area consisting of very small particles (approx. 2nm) is formed.

Advantages of the Sol-Gel method: (Vennila R. *et al.*, 2014).

The sol-gel method is an alternative in the preparation of nanomaterials. Some of the potential advantages of this method with respect to traditional synthesis techniques are presented below:

1.- Very high homogeneity and purity.

2. Total control of particle size.

3. High surface areas (Brunauer – Emmett – Teller, (BET) theory) and regulated pore size.

4. Higher thermal stability.

5. Ease in the addition of elements in the nanomaterial network.

6. Control of nanocrystallinity, manipulating the porosity.

7. Minimization of thermal degradation, due to the low temperatures at which all the stages are carried out.

8. Possibility of controlling the functionalization, by modifying the precursors and the hydrolysis and condensation rates.

9. Control of pore size and mechanical strength by regulating drying and aging conditions.

1.3 Nucleation and Growth Process

1.3.1 Nucleation Growth Models

There have been many studies about using different precursors while (LaMer V. K. and Dinegar R. H., 1950) proposes that the monomers nucleation takes place when the hydrolysis is completed and at the moment when the concentration overcomes a critical value, (LaMer V. K. and Dinegar R. H., 1950) proposed some conclusions regarding the formation of monodispersed hydrosols. The relationship between the concentration of sulfur and the volume of fraction of water at one critical point of sulfur-ethanol-water has been studied. Another point of his research was the sols prepared by his method has been investigated as to dispersion of wave length in their angular scattering of visible light and their transmission as a function of wavelength. Lamer also did research on the rates of growth obtained and have been reproduced from previous theoretical considerations which allow the estimation of value of the diffusion coefficient in alcohol-water and acetone-water mixtures. (LaMer V. K. and Dinegar R. H., 1950)

Other studies concerning the the TiO_2 synthesis via Sol-Gel, one of these precursors has been the TTIP (Titanium Tetraisopropoxide), mixed with water, has been studied by (Chappell J. S. *et al.*, 1990), (Rivallin M. *et al.*, 2005), (Azouani R. *et al.*, 2010)

There have been results with zirconium oxo-alkoxide nanoparticles (ZOA) in alcohol in micromixing sol-gel reactor by (Tieng S. *et al.*, 2012) and (Labidi S. *et al.*, 2015) (Labidi S., 2015). They both investigated the effect of precursors and solvents on the particle growth and proposed a model.It was confirmed that particle sizes are monodisperse and equal to 4.7 nm of diameter and in parallel the growth is like the titanium oxo-particles growth.

(Chappell J. S. *et al.*, 1990) proposed the following hierarchical growth in Figure 13:

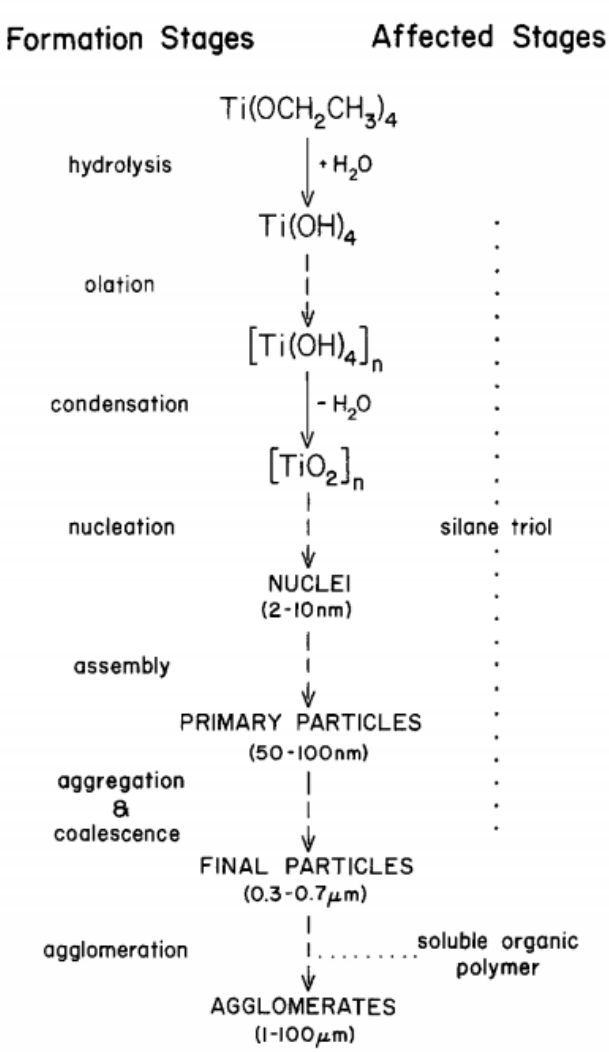

Figure 13 The stages of the particle size achieved from the TTIP hydrolysis in presence of silane triol (Chappell J. S. *et al.*, 1990).

Monomehtyl silane triol was used as a condensation inhibitor for the study of growth particle of titanium oxide. According to the results, the growth process which takes place after the hydrolysis has several steps to be considered. These stages could be placed in the following order: Inorganic polymerization by condensation, which drive to the nuclei formation from 2 nm to 10 nm. Then this newly formed nuclei give place to primary particles formation stage which size varies from 50 nm up to 100 nm and finally an stage where larger spherical particles from 0.3 µm to 0.7 µm could be formed.

(Soloviev A. *et al.*, 2001) studied the nucleation and the growth kinetics of titanium oxo-alkoxide particles synthesized by sol-gel method using the Static Light Scattering (SLS) and the Dynamic Light

Scattering (DLS) using isopropanol as a solvent. The Figure 14 shows the evolution of the particle's radius and the scattered light intensity.

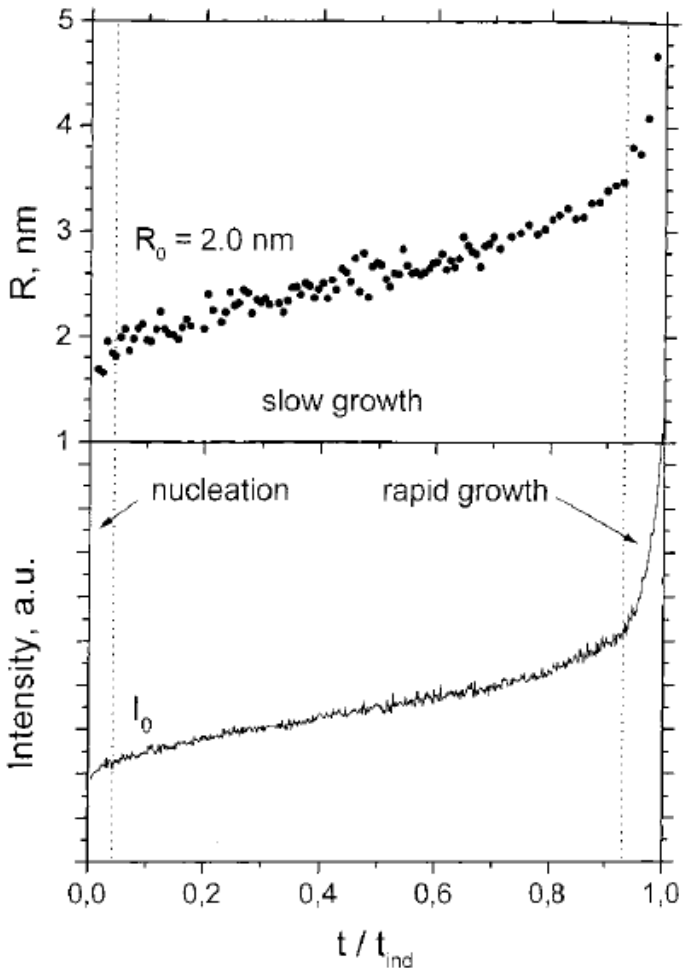

Figure 14 Evolution of the particle radius and the scattered light intensity at the time of the sol-gel way (Soloviev A. *et al.*, 2001).

According to the results presented by (Soloviev *et al.* 2001), particles up to 2 nm diameter start to appear at the beginning of the sol-gel process followed by a relatively long period of their slow growth. It is also noticed that when the nanoparticles size increases the double, the scattered light intensity also increases in a sudden way.

As a conclusion of these results, the almost spontaneous nucleation after the mixing of the reagents process has been attributed to the primary hydrolysis-condensation reactions and in the other side is the induction period to the nuclei aggregation because of the secondary surface hydrolysis

condensation reactions between the nanoparticles. During this time, the solution remains transparent. When the nanoparticles start to lose stability and to precipitate, the solution becomes white and opaque. (Soloviev A. *et al.*, 2001) proposed the following derived equation based in the analysis of induction time (t_{ind}) as a function of isopropoxide (c_t) and water (c_h).

$$t_{ind} \propto C_t^{-\propto} \cdot (C_h - C_t h_0)^{-\beta}$$

Equation I-0-1

With parameters as h_0=1.45, α = 1.5 and β = 4.7. The value h_0 corresponds to the nucleus condensation ratio, which matters for its structural composition.

(Azouani R. *et al.*, 2007) studied the effect of the hydrolysis ratio on the particle size change. It can be noticing a particularity regarding in the high initial homogeneity of the local fluid mixture composition. The bulk reactions then proceed in low polydispersity of the produced nanoparticles and eventually clusters.

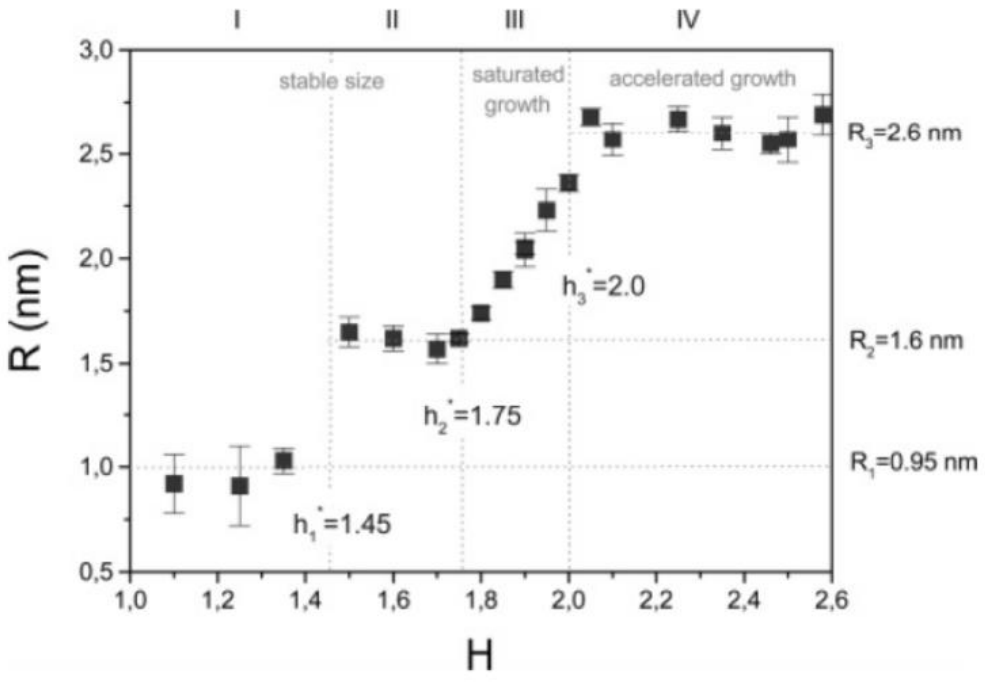

Figure 15 Domains of the TiO_2 nanoparticles growth during sol-gel method (TTTP=0.146M, T=20°C) (Azouani R. *et al.*, 2007).

The four domains observed in the Figure 15 are the following:

Domain I: Where H<1.45. This domain corresponds to the stable size units where small clusters are formed. The smallest stable particles size is R=0.95±0.1 nm, and they may be assigned to the Keggin-type structure for $Ti_{17}O_{24}(O^{i}Pr)_{20}$ oxo-alcohoxy described by Steunou *et al.* (Steunou N. *et al.*, 1999).

Domain II: Where 1.45<H<1.75. This domain corresponds again to the stable size units where larger clusters sizes are formed and remains stable. These spherical clusters have a radius of R=1.60±0.05 nm.

Domain III: Where 1.75<H<2.0. This domain is defined by the cluster instability, because they quickly agglomerate in short chains, where limit size depends on the H. This domain belongs to a period known as “growth limitation”.

Domain IV: Where H>2.0. This domain corresponds to the induction period of the accelerated nanoparticles growth, after they reach a size of 2.69 nm, nuclei are formed, and they are exposed to an irreversible growth until TiO_2 solution precipitates at the induction time.

1.3.2 Micromixing Sol-Gel Reactor

The micromixing is a very important factor that impacts when is observed the particle size distribution. The effects of mixing can be the stirrer speed, feed time, feed location and viscosity (Chen J. *et al.*, 1996) (Bałdyga J. and Pohorecki R., 1995). There have been several studies regarding the understanding of nanosized solids precipitations. (Schwarzer H. C. and Peukert W., 2004) (Schwarzer H. C. *et al.*, 2006) (Wang L. and Fox R.O., 2004) (Artelt C. *et al.*, 2006) (Gradl J. *et al.*, 2006) (Marchisio D. L. *et al.*, 2006). These studies emphasize the development of a relevant numerical model of turbulent mixing in accordance with the particle size distribution.

In order to reach a homogeneous reaction condition, high reaction order (Soloviev A. *et al.*, 2003) and the rate of hydrolysis condensation reactions (Livage J. *et al.*, 1988) have to be considered into

account, because they establish some severe constraints, which are very important in order to achieve particles monodispersity and reproducibility on the process kinetics.

To obtain a reproducible synthesis of size selected monodispersed nanoparticles, it needed the design of a sol-gel limit reactor with a fast micromixing was needed. This was obtain through a series of previous research.

The design and set-up of the micromixing reactor has been studied and described previously in some research studies. (Rivallin M. *et al.*, 2005) (Azouani R. *et al.*, 2010) The Figure 16 shows the diagram of the micromixing reactor

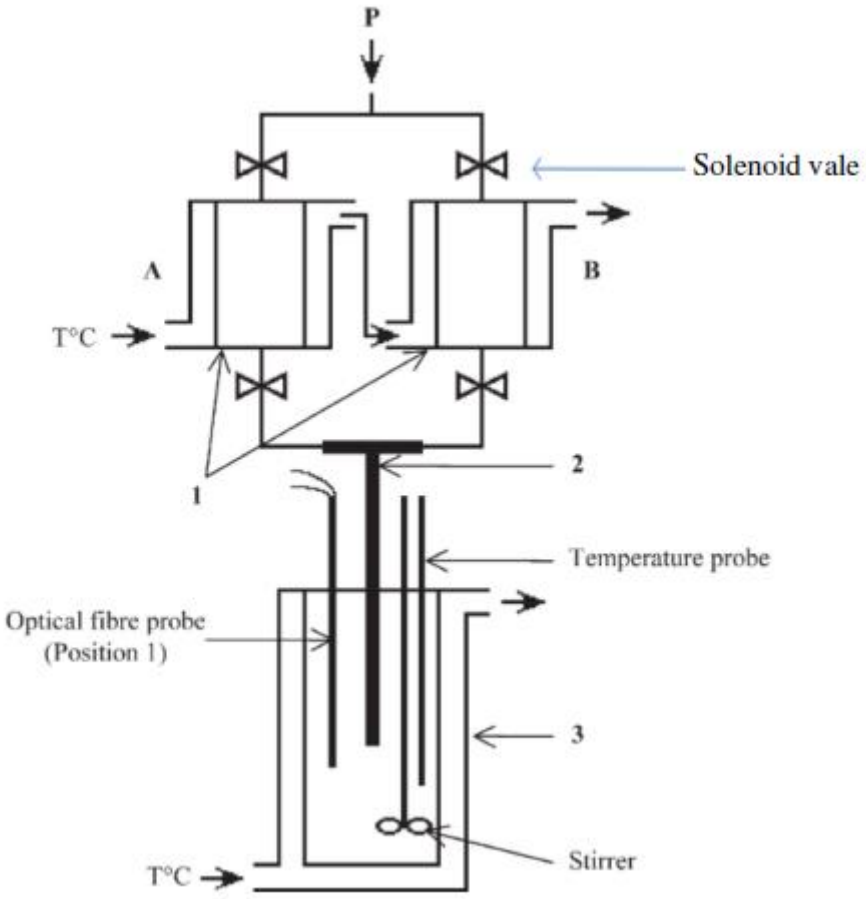

Figure 16 General diagram of the micromixing reactor 1) (A) Precursor container (B) Water solution container 2) T-Mixer 3) Thermostatic reactor.

The micromixing reactor consists of three main parts: two Thermostatic containers, one T-mixing element and one container for the prepared solution.

The thermostatic containers are made of stainless steel (inner and outer covers) each one with a capacity of 100 mL. This thermostatic or reservoirs are placed at the upper part of the setup. Temperature is regulated via a thermostat. The isopropoxides and the water in n-propanol have be previously prepared inside a glove-box under strict conditions (≤0.5 O_2 ppm and ≤0.5 H_2O ppm). As TTIP is very sensitive to the humidity, any contamination from the environment must be avoided. Then the prepared reagents solutions are transported in syringes of 50 mL, to their respective container. A permanent flow of nitrogen allows the reactor to be under controlled conditions, meaning that we avoid any humidity that could enter to the system. A supply of nitrogen with water less than 5 ppm is connected to both stocks solutions. The solenoid valves are used to control the period of gas applied into the containers. The pressure from the bottle of nitrogen can be controlled so we can have the best Reynold number to obtain monodisperse nanosized particles.

Then we have the T-Mixer, which consists of two inlets, with an internal diameter of 1 mm and a 20 mm of length, and one outlet part of 2 mm diameter and 200 mm of length as shown in Figure 19. The importance of the diameters have been decided upon the importance of controlled conditions (Reynolds Number) $Re = \frac{4Q\rho}{\mu\pi d}$, where Q = fluid flow ($m^3.s^{-1}$), ρ = density ($kg.m^{-3}$) μ = dynamic viscosity (Pa.s) and d = outlet diameter (m).

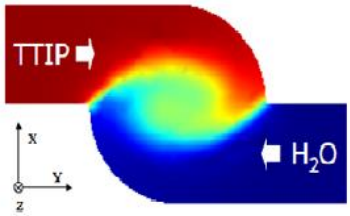

Figure 17 Representative scheme of the turbulent fluid flow injection in T-mixer at mixing zone point (Azouani R. *et al.*, 2010).

(Azouani R. *et al.*, 2010) made research concerning the effect of the Reynolds number on the particle size when the injection of the isopropoxides, solvent and water get combined in the T-Mixer. Experiments were performed with different injection rates.

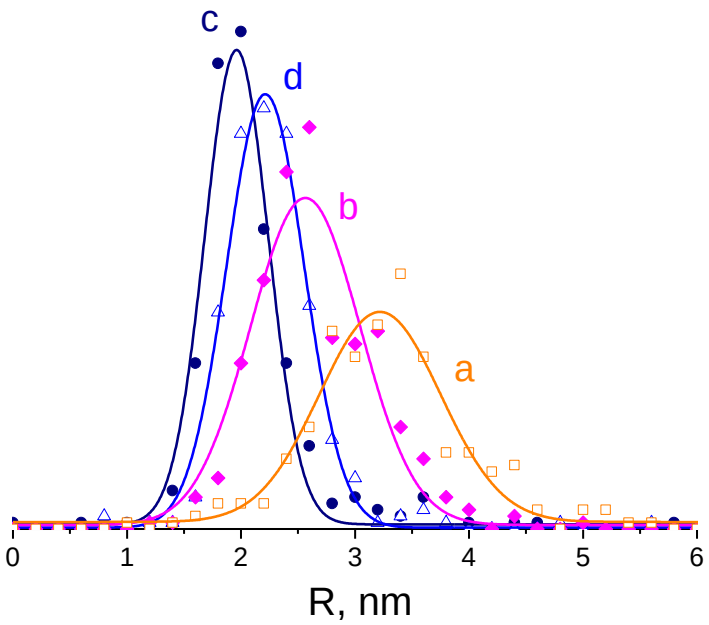

Figure 18 Distribution of TOA particle sizes according to their mixing number Reynolds a) 2 x10^3, (b) 3 x10^3, (c) 6 x10^3, (d) 8 x10^3 (Azouani R. *et al.*, 2010).

In the Figure 18 it shows that at different injection rates Re=2.10^3 (a), 3.10^3 (b), 6.10^3 (c), 8.10^3 (d) at the following experimental conditions: H=1.9 C_{Ti}=0.146 mol/L and T=20°C. According to these results the mean particle size and the width of the distribution curve decrease, for a very high Reynolds number Re= 8.10^3 (d). The distribution of size particle is narrow, but the reproducibility is low. The best optimal condition found is with Reynolds Number), 6.10^3 (c).

There have been studies where it shows that the time of mixture is based on the neutralization of the reaction between a strong base and a strong acid with the help of a color indicator and the design of the internal volume of the T-Mixer permits the formation of tangential inlet jets. For this reason, there is a formation of a vortex that leads to the micromixing. (Pohorecki R. and Baldyga J., 1983) (Li K. T. and Toor H. L., 1986)

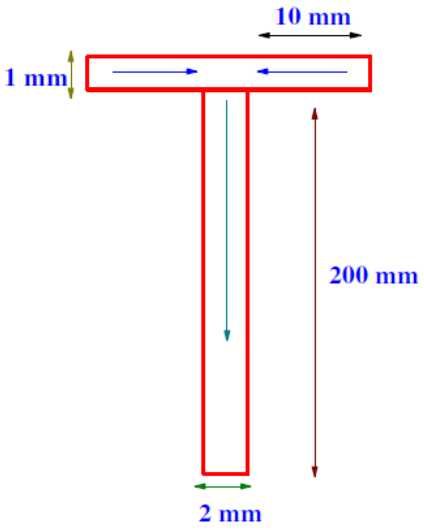

Figure 19 Diagram of the T-Mixer.

The container that holds the final solution is a double walled cylindrical glass with an inside diameter of 5.5 cm and it holds a volume of 250 mL. The temperature for the whole system is regulated via a thermostat (Haake, DC10K15), which allows a regular circulation of the coolant water.

There is a especial space where an optical fiber probe is placed to measure the nanoparticles in-situ.

1.4 Monitoring of growth process

There are two spectroscopy analysis that grants the corresponding measurement of the light intensity scattered and size particles suspended in a sol from 1 nm up to 500 nm. Moreover, the light effect can provide two kinds of information: The intensity of diffused light by particles is given by the Static Light Scattering (SLS) and the particle's hydrodynamic radius is given by the Dynamic Light Scattering (DLS), both are non-destructive analysis techniques. Therefore, the result becomes that four domains of the nanoparticles/clusters stability and growth kinetics can be appreciated.

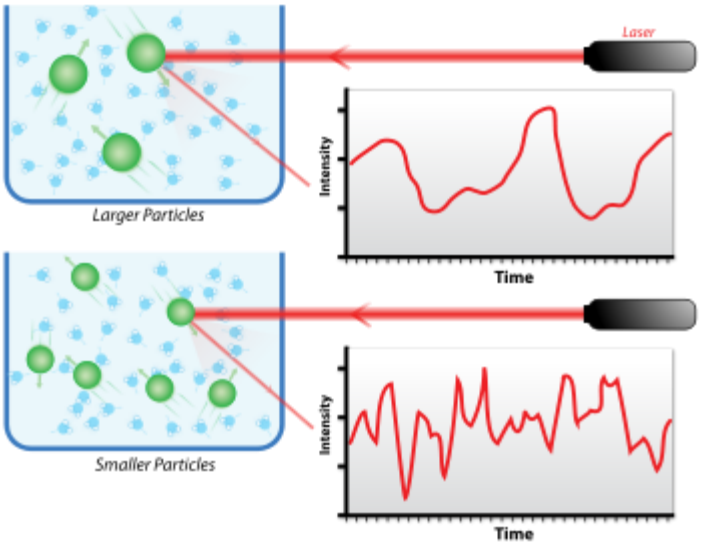

Figure 20 Dynamic light scattering of large and small particles.

When is given the condition that the particles radius is smaller than the incident light wavelength, the next relation could be written like this:

$$\frac{2\pi nR}{\lambda} \ll 1$$

Equation I-2

Where n is the particle refractive index. Rayleigh and later Van de Huslt, have developed a theory for diffusion. The intensity of the diffused light depends on the observation angle, and it can be described as it follows

$$I(\theta) = I_0 \frac{9\pi^2 n_0^4}{\lambda^4} \frac{V^2}{R^2} \left[\frac{m^2-1}{m^2-2}\right]^2 \frac{1+\ cos^2(\theta)}{2}$$

Equation I-3

Where θ is the diffusion angle, I_0 is the initial intensity of the incident beam, n_0 is the refractive index of the medium, V is the real volume of the particle, R is the distance between the particle and the observation point, $m=n/n_0$ is the relative reflective index

There are some observations that should be pointed out:

1. - Only when the intensity of the incident light is changed, the relation between I and λ is the following one

$$I\ \alpha\ \frac{1}{\lambda^4}$$

Equation I-4

2. - The scattered intensities front (θ=180°) and back (θ=0°) diffused intensities are the same:

$$I(\theta) = I(\pi - \theta)$$

Equation I-5

3. – The diffused light intensity is proportional to the square of the particle volume:

$$I\ \alpha\ V^2$$

Equation I-6

This relation is correct if it is assumed that the particles consisted of the same number of molecules (N) and an electrical component of electromagnetic field (E) diffused by every molecule is a constant value. If the particle size is very small compared to the wavelength of the incident light, the scattered waves of N molecules are in phase. In this case, the total diffused electric field (E_T) is presented by the sum of elemental electric fields scattered by each molecule: $E_T = N*E$.

Because the intensity of q radiation is proportional to the square of the electric field, then the scattered intensity equation is the following:

$$I\ \alpha\ E_T^2 = N^2E^2\alpha N^2$$

Equation I-7

In view of homogenous particles, the density is the same at different points, its volume V is proportional to N

$$I\ \alpha\ V^2$$

Equation I-8

Up to here, there is no dependence between the form of the particle and the relation of its volume with the intensity of the diffused light. The particle form shape does not matter, it could be spherical, or it could be open structure (fractal). In case of a dense spherical particle of Radius, we can obtain:

$$I \; \alpha \; R^6 \qquad V = \frac{4}{3}\pi R^3$$

Equation I-9

Moreover, (Soloviev A. *et al.*, 2003) and (Rivallin M. *et al.*, 2004) have proved that for a particle with fractal dimension D_f, the intensity of the scattered light I is proportional to the average radius R of particles raised to the power D_f.

$$I \; \propto \; R^{D_f}$$

Equation I-10

Hydrodynamic radius particles measurements

The hydrodynamic radius of the nanoparticles can be measured from the intensity of the DLS. In a perspective, this method is based on the Doppler Effect. When a particle is in Brownian motion; a particle can influence the spectrum of diffused light broadening the spectrum because of the Doppler Effect. When the particles gets closer to the observation point, diffuse light with $\lambda' < \lambda$, and in contrary case, molecules moving at different direction they will diffuse light with a different wavelength $\lambda'' > \lambda$.

As a result, the heterogeneity of the total light diffused will produce the broadening of its spectrum produced by molecules in Brownian motion. The value of the spectrum depends on the velocity of the particles: The higher the particle velocity has, the higher the broadening effect will increase and observed.

In case of spherical particle observation, the relation between the particles radius and the diffusion coefficient is described by the Stokes-Einstein equation. (Einstein, 1905)

$$D = \frac{k_B T}{6\pi\mu R}$$

Equation I-11

Where μ (Pa.s) is the dynamic viscosity of the medium, T (K) is the medium temperature and k_B (1.3806.10 $^{-23}$ J*molecule^{-1}K^{-1}) is the Boltzmann constant. This relation demonstrates that the diffusion coefficient is proportional to the inverse of the particles radius when the temperature is constant.

Theoretical approach in dynamic light diffusion

There are two parameters that induce the fluctuation of the light diffusion spectrum, the particles in Brownian motion and the particles number in the observed diffusion volume. Consequently, the temporal correlation function will give the information about the spectrum light diffusion intensity and the particle size (Berne B. J. and Pecora R., 1977).

(Pike H. Z. *et al.*, 1974), (Pecora *et al.*, 2000) and (Glauber R. J. *et al.*, 1963) have established the relationship between the diffusion coefficient and the form of the spectrum of light diffusion intensity using the help of the autocorrelation functions of the intensity and the electric field value of diffused light. The following equation presents the function which includes the intensity of the diffused light and the electric field value.

$$G^{(1)}(t') = \langle E_D^*(t) \cdot E_D(t+t') \rangle$$

Equation I-12

Where $\langle\langle E_D^*(t) \cdot E_D(t+t')\rangle\rangle$ corresponds to the average value of measurements and t' is the correlation time.

The relation of $G^{(1)}$ with spectral intensity I(w) is:

$$I(w) = \frac{1}{2}\int_0^\infty G^{(1)}(t') \cdot e^{iwt'} \cdot dt'$$

Equation I-13

The relation between normalized autocorrelation function $g^{(1)}$ of electric field diffused by particles in Brownian motion and coefficient of diffusion D can be described as the following equation (Pecora, 2000)

$$g(t')^1 \propto exp(-Dq^2t' - iw_0t')$$

Equation I-14

- $g^{(1)}$ is a normalized form of $G^{(1)}$ in respect to the initial time and is defined by the following equation

$$g^{(1)}(t') = \frac{G^{(1)}(t')}{G^{(1)}(0)}$$

Equation I-15

- ω_0 is the angular frequency and v is the frequency, represented in the following equation:

$$\omega_0 = {}^{2\pi}/_{v} \cdot v - frequency$$

Equation I-16

- The module of the diffusion vector is the following equation:

$$q = \frac{4\pi n_0}{\lambda} sin({}^{\theta}/_{2})$$

Equation I-17

- The observation scale of the system is represented by the inverse of the wave vector module q^{-1}, which is fixed by the observation angle θ.

The spectral intensity has the form $\Gamma=Dq^2$ at its half-width Lorentzian form:

$$I(\omega) \propto \frac{\Gamma}{(\omega - \omega_0)^2 + \Gamma^2}$$

Equation I-18

The autocorrelation function of the intensity I could be represented as the following equation:

$$G^2(t') = \langle I_D(t) \cdot I_D(t+t') \rangle \; with \; I_D = E^2$$

Equation I-19

Its normalized form is the following:

$$g^{(2)}(t') = \frac{G^{(2)}(t')}{G^{(2)}(0)}$$

Equation I-20

Based on the experimental data obtained by DLS, the autocorrelation function of the diffused intensity $g^{(2)}$, In the case when the light diffusion presents the Gaussian form (in case of particles concentrations in the diffusion volume is high), $g^{(1)}$ and $g^{(2)}$ are described by the Ziggert relation (Glauber R. J., 1963)

$$g^{(2)}(t') = \left|g^{(1)}(t')\right|^2 + 1$$

Equation I-21

And finally it is obtained for $g^{(2)}$

$$g^{(2)}(t') = 1 + e^{-2\Gamma t'}$$

Equation I-22

Based on the experiments of DLS, the measured function is presented as:

$$\tilde{G}^2(t') = A + B \cdot e^{-2\Gamma t'}$$

Equation I-23

For easier purposes $\hat{G}^{(2)}$ is replaced by G

When t' tends to 0, the value of G is equal $\langle I^2(0) \rangle$. When $t' \longrightarrow$ 0, intensity time t is the same as the initial time. After enough time (when t' tends to infinity), the correlation at the initial time becomes 0, it means that it disappeared. This phenomenon is caused because of the particles that are in Brownian motion. In this case G(t') is equal $\langle I^2(0) \rangle$. The constants A and B depend on the light coherence and the accumulation time of the autocorrelation function.

$$A = \langle I_D(\infty)\rangle^2 \; and \; B = \langle I_D^2(0)\rangle - \langle I_D(\infty)\rangle^2$$

Equation I-24

The constants A, B and D from the autocorrelation function become obtainable and finally with the aid of the Stokes-Einstein equation, we can obtain the value of the average radius of the particle.

Chapter II Characterization Methods

This chapter will explain the different techniques employed during the duration of the project, the explanation also includes the principal function, how they work and what results can give.

2.1 XRD

X-ray Diffraction (XRD) is a non-destructive analytical technique mainly used for phase identification of a crystalline material and it gives information about structures, phases, texture, and structural parameters like for example average grain size, crystallinity, strain and crystal defects.

Crystals are considered an array of atoms, and X-rays can be imagined as waves of electromagnetic radiation. So, when the incident X-ray beam reaches a crystal lattice, the electrons or scatterers start oscillating and they emit the same frequency electromagnetic wave. If scatterers are ordered in a symmetrical way with a separation, these waves will be in synchronization, in that case, part of the incoming beam is deflected by an angle 2θ, creating a reflection spot in the diffraction spot. The distance the X-ray reflects from successive planes changes by a natural number n of wavelengths, which is determined by the Bragg's law.

$$n\lambda = 2dsin\theta$$

Equation II-0-1

n is the diffraction order

λ is the wavelength of the incident ray

d is the spacing between diffracting planes hkl

θ is the angle

These specific directions show themselves as spots in the diffraction pattern, the atomic position within the lattices determines the peak intensities, In consequence, the XRD pattern is the fingerprint of periodic atomic rearrangements of a material.

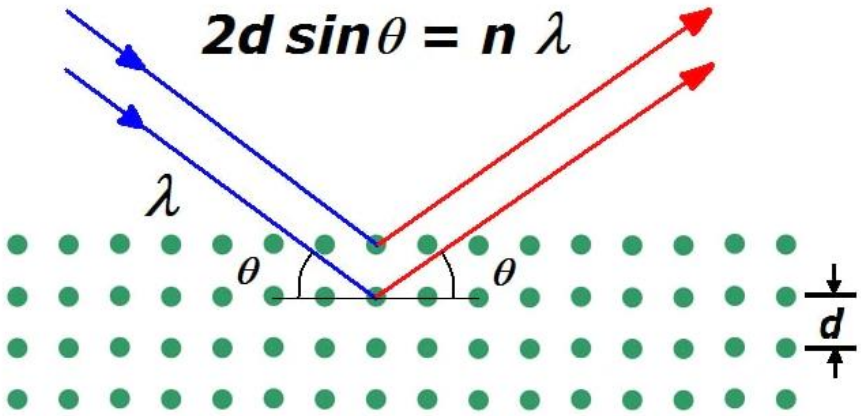

Figure 21 X-Ray Diffraction principle.

The samples were structurally characterized by XRD on INEL XRG 3000 installation using Co-K1 (=1.789 Å) radiation source

The diagram depends on the structure (peak intensities and positions) and sample microstructure (peak widths), crystallite size and microstrain. The peak width is related to the crystallite size by the Scherrer law :

$$\beta(2\theta) = \frac{\lambda}{T_{hkl} cos\theta}$$

Equation II-0-2

Which β is the full width of the peak, λ is the wavelength of the incident X-ray beam, T_{hkl} is the average apparent size of the crystallites and θ is the Bragg angle. The peak width is thus inversely proportional to the particle size in the power sample. In the case of spherical particles, T_{hkl} is constant and the particle could be obtained by multiplying it by 4/3. Microstrains also induce a peak enlargement according to the following equation:

$$\beta(2\theta) = \eta tan\theta$$

Equation II-0-3

With β the full width of the peak, η the apparent microdeformation and θ the Bragg angle. The samples were structurally characterized by X-ray diffraction (XRD) method with two diffractometers:

- Phase characterization: INEL XRG 3000 installation using Co-Kα1 (=1.789 Å) radiation source.

- Structural analysis and Rietveld refinement: D8 Discover equipped with a Copper source ($K_{\alpha1}$ = 1.54056 Å: $K_{\alpha2}$ = 1.54439 Å, I_2/I_1 = 0.5) and a Lynxeye XE-T detector (1D mode). Measurements were done in collaboration with Dr. Capucine Sassoye and Mohamed Selmane from the Laboratoire de Chimie de la Matière Condensée de Paris (UMR CNRS 7574).

To get the structural (cell parameters, atomic positioc, etc.) and microstructural information (size, microstrian, etc.) about the powder samples, data treatment was performed using the Rietveld method. (Rietveld H. M, 1969) (Young R. A., 1995) Refinements were performed using the Fullprof software (Rodríguez-Carvajal J., 1993). The principle of the method is to fit a diffractogram calculated from a structural and microstructural model to the experimental diffractogram using the least squares method. The refined parameters are the cell parameters, the atomic positions, the atomic displacement factors, the scale factor, the phase percentage, the continuous background, and the line profile. To model the line profile, we used the pseudo-Voigt function, which is a linear combination of a Gaussian function (G) and a Lorentzian function (L), defined by the following equation:

$$pV=(2\theta)+(1-\eta)G(2\theta)$$

Equation II-0-4

where G is a Gaussian function and L is a Lorentzian function. In the Thompson-Cox formulation the mixing parameter η is calculated from the Gaussian (Γ_G) and Lorentzian (Γ_L) widths of an equivalent Voigt function with:

$$\Gamma G=(Utan2\theta+Vtan\theta+W+Zcos2\theta)^{1/2}$$

Equation II-0-5

$$\Gamma L=X\ tan\theta+Y/cos\theta$$

Equation II-0-6

The analysis was performed by fixing V and W to zero, and refine U, X, Y and Z which have a meaning respectively in terms of strains (U, X) or size (Y, Z). The contribution of the continuous background is modelled by a polynomial function of order 12, whose coefficients can be refined. The CIF structure file used for the refinement procedure were obtained from for anatase TiO_2 and from for α-V_2O_5. (CrystallographyOpenDatabase, 2010)

2.2 TGA-TDA

The Thermo Gravimetric Analysis (TGA) is a thermoanalytical technique where an electronic microbalance with a furnace and a temperature controller measures the variation of the selected sample as a function of time and temperature. This technique is commonly used to determine the characteristics of materials, for example their thermal stability, adsorption- desorption and kinetics of chemical reactions. Also is used to study the material weight loss due to oxidation or decomposition.

The Thermal Differential Analysis (TDA) is a technique where it measures the temperature difference between a sample and a reference as the temperature is increasing over time. Then a thermogram (plotting of the temperature difference) is shown where it reveals the exothermic and endothermic reactions they could happen in the sample. It can determine the temperature of thermal phenomena like for example, crystallization temperatures, melting points and phase transitions.

In this work, the thermal studies were performed on two equipments due to technical situations. The first one is a Thermoanalyzer SETARAM TG92 between temperatures of 100°C and 1000°C with an air flow and a rising speed of 10°C min^{-1}. The other equipment carried out with Labsys Evo SETARAM with the same conditions (temperatures and air flow) described above.

2.3 Raman

The Raman Spectroscopy is a spectroscopic technique that gives detailed information about vibrational modes of molecules, in chemistry it is commonly used to provide a structural fingerprint where molecules can be identified.

The Raman used in the laboratory is a type Jobin-Yvon HR800, it is equipped with a motorized X-Y stage that allow to do the imaging and an adjustable aperture confocal slit system. The excitation wavelenghts that can be used are 632.8 nm thanks to a laser He/Ne incorporated to the equipment and where the wavelengths go from the visible (514 and 448 nm) up to the ultra-visible (363.8 nm) using high power ionized Argon laser (30mW).

2.4 UV-VIS Spectroscopy

The UV-Vis Spectroscopy is a quantitative technique used in the laboratories to measure how much a material or a substance can absorb light. This is possible by measuring the intensity of the light that passes through the sample in comparison to the intensity of light through a blank or reference sample. This technique can be applied for measuring different kinds of samples, including solids, thin-films, glass, and liquids.

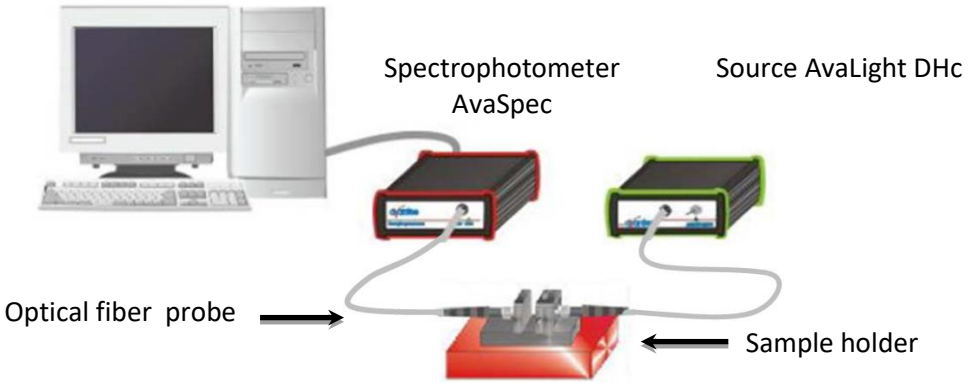

Figure 22 Scheme of the Spectrometer UV-Visible Avaspec.

In the present work, the UV-VIS specters were measured using an AvaSpec UV-visible spectrometer with spectral resolution of 0.5 mm 2048x14 with a CCD sensor (2048X14 pixels) operating in a range of 200-1160 nm. With a slit opening of 50 µm, the spectral resolution is 2.4 nm, the signal to noise ratio is 500:1. The spectrometer is connected to the source and to the sample holder using optical fibers of 400 µm of diameter and 2 m of length. The AvaLight-DHc compact source is of Deuterium and Halogen lamp emitting between 2000 to 2500 nm. The acquisition of the data recollected during the experiments were done using AvaSoft software version 7.4.

2.5 Data Treatment of the autocorrelation function

The intensity of light, when is measured in the Rayleigh conditions, is the sum of all intensities scattered by every single particle present in the suspension studied.

The Brownian motion of particles influence on the evolution of the diffused intensity.Its fluctuation is shown on Figure 23 a. In consequence the autocorrelation function of intensity can be calculated with the correlator, t' is a fixed constant value and represents delay between two intensities measurements. Lastly, the product of intensity values can be found with this method: $I_D(t) * (t+t')$. This operation must be repeated for many values of t', the Figure 23 b shows the autocorrelation function of intensity, that has been calculated in function of time.

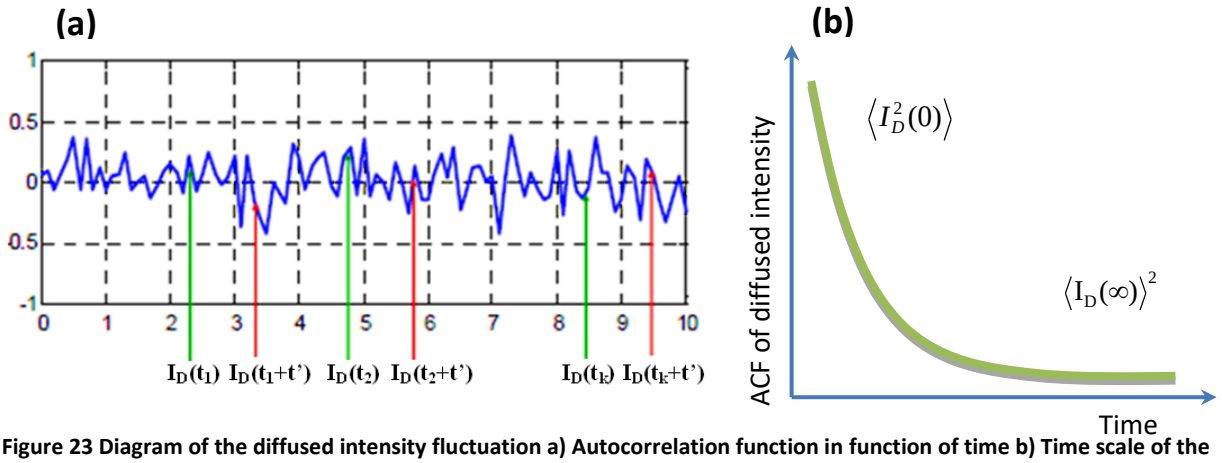

Figure 23 Diagram of the diffused intensity fluctuation a) Autocorrelation function in function of time b) Time scale of the fluctuation depends on the particle's diffusion coefficient which is in inverse proportional to the particle's radius.

The G value can be measured in the photocounting regime, when the intensity is measured by a photomultiplier, as series of photon impulses. The number of photons $N_{ph}(t)$ between t and (t + dt) is in accordance with the intensity value I(t)*dt. Assuming that the process is a Gaussian like, the mean integral value can be obtained with the following equation:

$$G = \lim_{T\to\infty}\left(\frac{1}{T}\int_0^T N_{ph}(t)\cdot N_{ph}(t+t')\cdot dt\right)$$

Equation II-7

T time defines the accumulation time, which is a finite value, and when the G value increases the time Ti increases as well.

Data acquisition of the experimental set-up

The schematic diagram representation for the experimental set for the DLS measurements; used during the kinetic nucleation-growth studies of the nanoparticles is shown in the Figure 24

The set consists of three main parts:

1. A laser light source with the following characteristics: 20 mW, He-Ne laser spectra physics, λ = 632.8 nm
2. An optical system equipped with two optical fibers
3. Equipment used for the data acquisition such as a photomultiplier, an amplifier, a discriminator, a digital correlator, and a computer for data treatment.

The optical fiber: The incident light from the laser (20mW He-Ne laser Spectra Physics) is focalized on the observation zone with the aid of an emission fiber probe. This experimental set-up allows the measurements in-situ after the reaction begins. Two fibers are fixed on the sides of the probe, one optical fiber is the emission optical fiber and the other one is the reception optical probe. These two optical fibers are placed in an order that they form an angle of 90°. The observation volume is extremely small (10^{-6} mL) is enough to avoid any impact because of external contamination like dust. The diminished data accumulation period considered equal to 60 seconds.

From time to time, the fiber probe is calibrated using a water solution of Latex-Polystyrene particles, which size is equal to 50 nm.

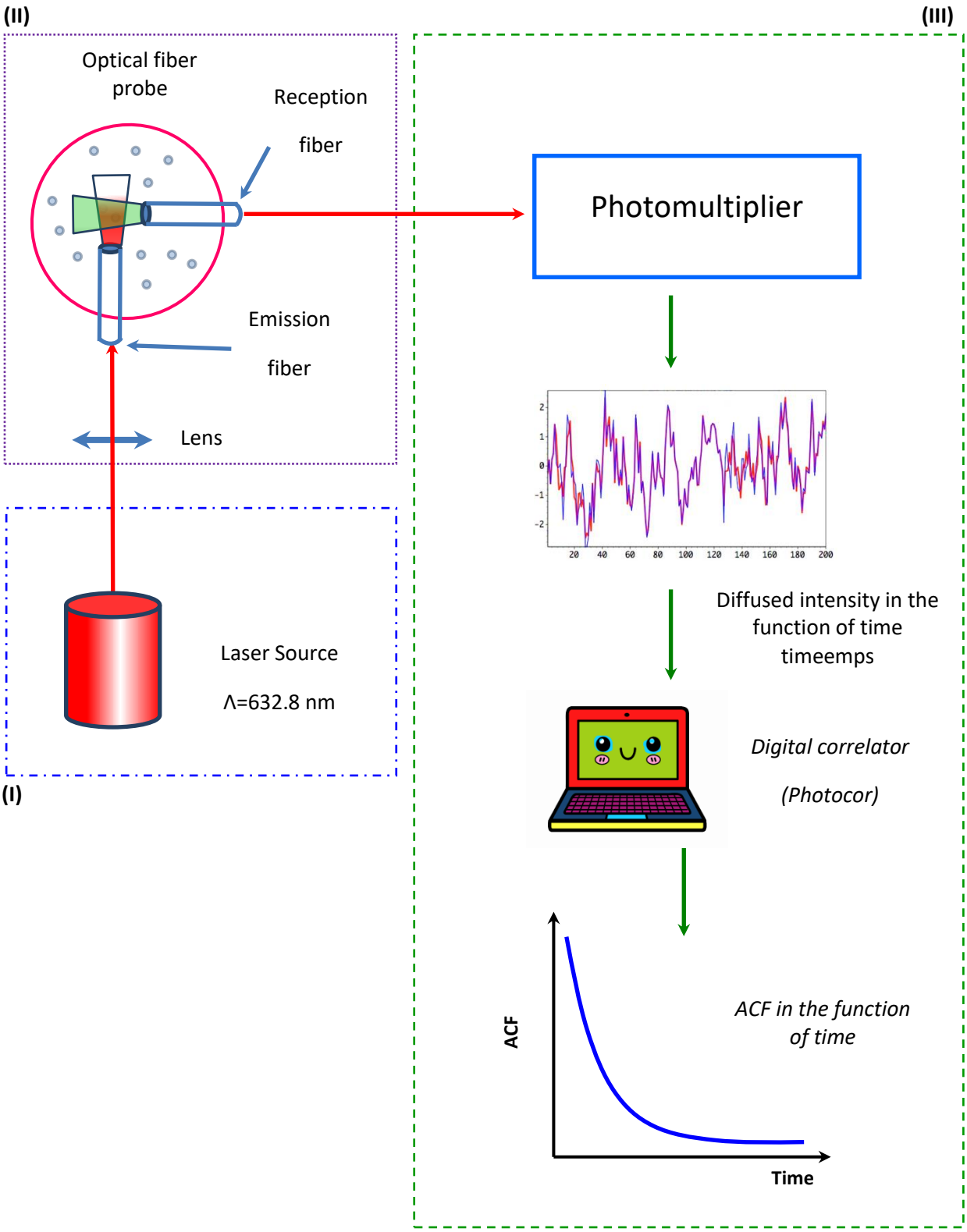

Figure 24 Diagram of the experimental setup for the DLS measurements.

Hydrodynamics radius determination

The Figure 25 shows an autocorrelation curve obtained with a water solution with Latex-Polystyrene, during a DLS experiment.

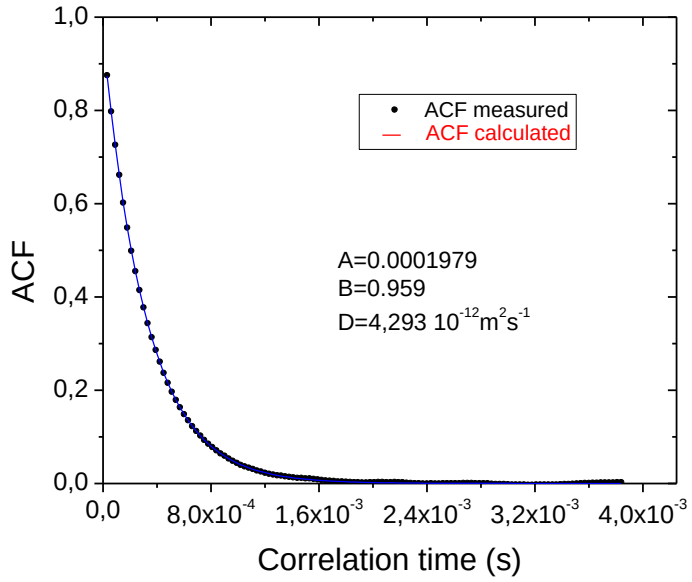

Figure 25 Autocorrelation function of the scattering light taken from a Latex-Polystyrene suspension in water.

The determination of the coefficients A, B and D are given by using a non-linear less square fit using the equation $G = A + B^{Dq^t t'}$.

The experimental parameters are the following:

- Refraction Index of water n_0 = 1.33 at 20°C
- Diffusion angle θ = 90°C
- Laser wavelength λ = 632.8 nm
- Dq^2 = k and $q = \frac{4\pi n_0}{\lambda}\sin\left(\theta/2\right)$, the diffusion coefficient is delivered by the ACF function, $D=4.29X10^{-12}\ m^2s^{-1}$

The particles average radius is obtained by using the Stokes-Einstein equation and the value of the diffusion coefficient D.

Chapter III Preparation of size selected VTOA

In this part, we will expose the different steps with the preparation of size selected V-TOA, and discuss the results obtained from the measurement in-situ of the V-TOA nanoparticles from the first steps of the reaction

3.1 Experimental Setup

a) Chemicals

The chemicals that were used during the duration of the work were the following:

The titanium tetraisopropoxide (TTIP, 98 % purity, Sigma-Aldrich) and vanadium(V) oxytripropoxide (VOP, 98 % purity, Sigma Aldrich) precursors, n-propanol solvent (99.5 % purity, Sigma-Aldrich), and distilled twice-filtered water (syringe filter 0.2 lm porosity PALLs Acrodisc) were used in the preparation procedure. To avoid any kind of contamination, overall, the contamination from the external humidity, all chemical manipulations were done inside a LABstar glove box workstation MBRAUN (strictly traces of oxygen and humidity ≤0.5 ppm)

b) For the preparation of the solution, all the glassware was washed and left to dry in the oven at 100°C for 1 hour to avoid any humidity, then we introduced the materials inside the glove box needed to prepare the solution A which is the oxypropoxides with solvent and B the amount of water with solvent which will determine the hydrolysis ratio.After the preparation of the 2 solutions in 2 syringes of 50 mL each, they were transported to the stocks of the T-mixer and then mixed at 6 bar. When obtaining the final solution, we proceeded to put inside the optical probe to measure the nanoparticle size.

c) The solvent we chose for the experiments was n-propanol. At the beginning of the thesis work, we experimented with different solvents by mixing manually V-TiO_2.The solvents we used were: n-propanol, isopropanol, butanol, 1,2 butanediol, methanol and ethanol. The results are observed in the following Table 1.

Solvent used with a solution of V-TiO_2 manually prepared	Observations
Isopropanol	Clear solution and stable
n-Propanol	Clear solution and stable
Butanol	Clear solution but it deposited material in the bottom of the glass.
1,2 Butanediol	Too much viscosity
Methanol	It didn't mix
Ethanol	Quick degradation

Table 1 Observations on different solvents.

One important noticed remark is that working with a higher molar ratio concentration of 20% of vanadium(V) oxytripropoxide, it left a film very hard to clean, meaning that it could contaminate the interior of the T-Mixer if more than 25% of vanadium(V) oxytripropoxide was used.

3.2 Results and Discussion

Before addressing the mixed-oxide system, the nucleation-growth process of the single oxides must be documented as a reference point. The similar approach has already proven its effectiveness in studies of $Zr_xTi_{1-x}O_2$ solids in a broad range of compositions $0 \leq x \leq 1$ (Cheng K. *et al.*, 2017). The nucleation-growth of titanium-oxo-alkoxy (TOA) species has been previously reported (Azouani R. *et al.*, 2010) (Cheng K. *et al.*, 2017). At the same time, no related information concerning VOA species is available in literature. First observation of the nucleation-growth process of VOA species is presented below.

As it has been shown, inhomogeneous reaction conditions of the sol-gel process generally lead to the appearance of strongly polydispersed species. In contrast, point-like reaction conditions in chemical reactors with ultrarapid ($t<10$ ms) micromixing permit the process with low Damköhler numbers

(Da≤1) resulting in the formation of size selected nanoparticles, among which a nucleus (basic unit of the growing solids) can be firmly identified. For example, DLS and TEM measurements have evidenced the basic TOA unit with radius of R_{TOA}=1.6 nm (Cheng K. *et al.*, 2017). Because only general information exists about reactivity of metal-oxo-alkoxy species (Livage J. *et al.*, 1988), different injection conditions in a T-mixer were tried, leading to the nucleation of VOA species. The size evolution of VOA species prepared manually and in the reactor at different Reynolds numbers (Re) of the injected fluids is shown respectively in Figure 26 a, and b.

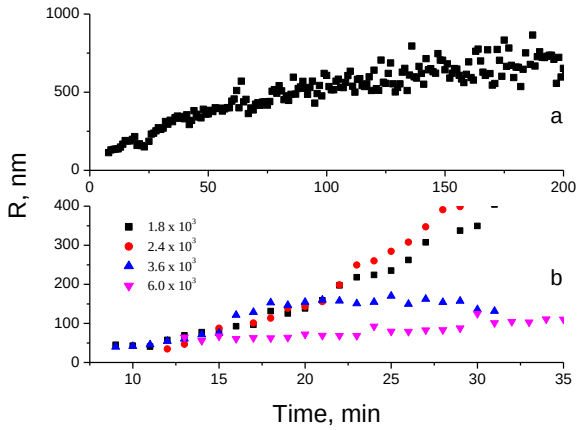

Figure 26 Mean radius of VOA particles prepared manually (a) and in micromixing reactor (b) with different Reynolds numbers (inset) of the injected reactive fluids (CV=0.30 mol/l, H=1.9, 20 °C).

As one can see, the radius of VOA particles prepared manually evolves from ~120 nm at the beginning to ~1 μm at the precipitation point. In contrast, the VOA particles prepared in the reactor are significantly smaller and have R_0=40 nm after injection; however, their growth kinetics depends on Re value. For relatively low Re<$3.6 \cdot 10^3$ the particles grow up to ~1 μm and precipitate (like with manual preparation), while at higher Re the particles remain much finer (R<100 nm) and stable for a long time (days) in colloids. This may infer the homogeneous nucleation of VOA species. We therefore concluded that Re=$6 \cdot 10^3$ correspond to the criteria of Da≤1 and conduct further experiments in these injection conditions.

The zoom on the very process beginning permits to define a VOA nucleus that begins the growth process: the extrapolation of experimental kinetics in Figure 27a to a common starting point provides

the particle radius of R_0=20 nm. The VOA growth kinetics confirms the mechanism of the sol-gel process earlier validated on Ti, Zr and Ti-Zr oxo-alkoxy species (Rivallin M. *et al.*, 2005) (Azouani R. *et al.*, 2010) (Labidi S., 2015) (Cheng K. *et al.*, 2017). The induction stage takes place at H above a critical value h^*, which is apparently smaller than the experimental values 1.80, 2.20 (Figure 27 b).

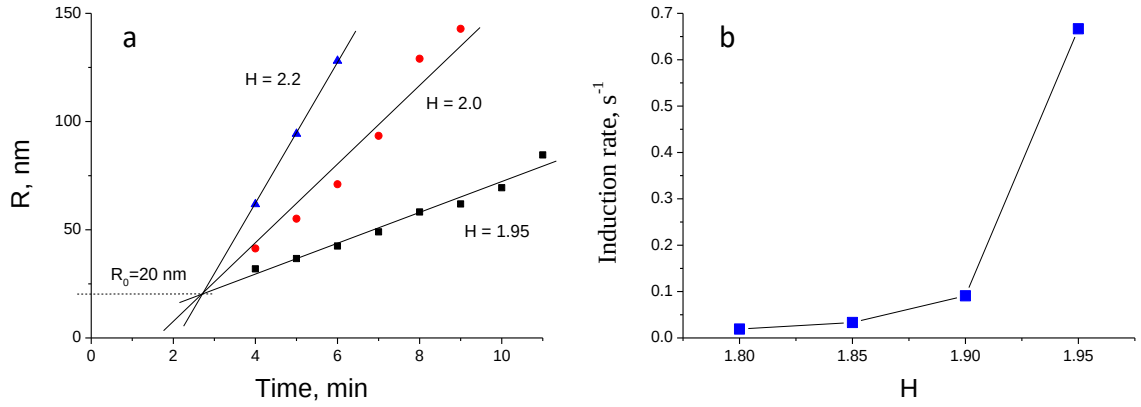

Figure 27 Growth kinetics of VOA nanoparticles in micromixing reactor: particle size versus time for different H (a) and induction rate versus H (b) (CV = 0.30 mol/l, 20 °C, Re=6000).

Afterwards, the first synthesis of mixed-oxide VTOA nanoparticles in micromixing conditions was carried out. The measured auto-correlation curves (ACF) in reactive media containing pure V and V-Ti precursors are shown in Figure 28. The ACF in the mixture Ti:V=0.05:0.95 (Figure 28a) fitted with two-exponential decay indicates the bimodal population with particle sizes of R_1=7.9 nm and 75 nm. Comparing the respective amplitudes A_1 and A_2 and considering that the scattering light intensity $I \propto R^6$ in the Rayleigh domain of particle sizes, one can conclude the population ratio $p(R_1) / p(R_2) \approx 2 \cdot 10^6$, which shows a strong preference of the small nanoparticle's formation in the reaction conditions. In contrast, removal of Ti precursor in similar reaction conditions (Figure 28b) results in a very weak (noisy) signal corresponding to rare particles of radius R_0=160 nm. We also notice that using pure Ti precursor in similar reaction conditions lead to the formation of monodispersed TOA particles of radius 1.6 nm (Azouani R., 2007). The observed difference indicates a strong interaction between the two V and Ti systems apparently leading to the nucleation of mixed oxide VTOA

nanoparticles. Most probably, because of the strong reactivity and rapid formation, Ti species nucleate first and serve condensation centers for V species.

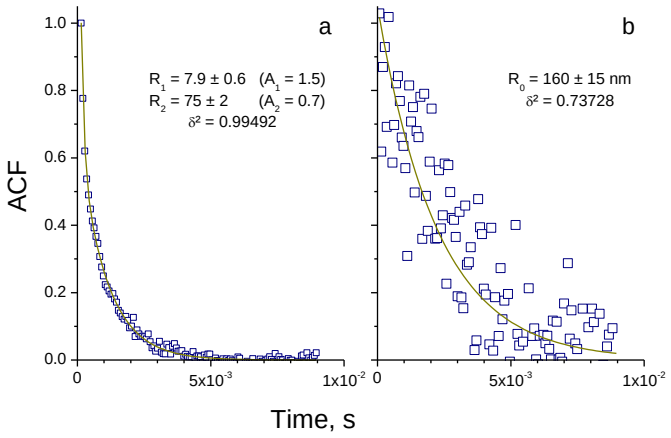

Figure 28 ACF curves of VTOA (a) and VOA (b) nanoparticles in reactive solutions: CTi=0.285 mol/l, CV=0.015 mol/l (a) and CTi=0 mol/l, CV=0.015 mol/l (b) (H=1.6, n-propanol solvent, 20°C).

The pure TOA and VOA systems show strongly different reaction kinetics and particles polydispersity. While TOA nanoparticles appear almost instantaneous after the reactive fluid's injection forming nucleus of size $2R_{TOA}$ = 3.2 nm. The population of VOA species of a large size ≥200 nm steadily grows after the injection. At the same time, preliminary experiments have indicated a strong interaction between TOA and VOA systems when the respective precursors are introduced in the same n-propanol solution (Sanchez Mendez M. *et al.*, 2019)

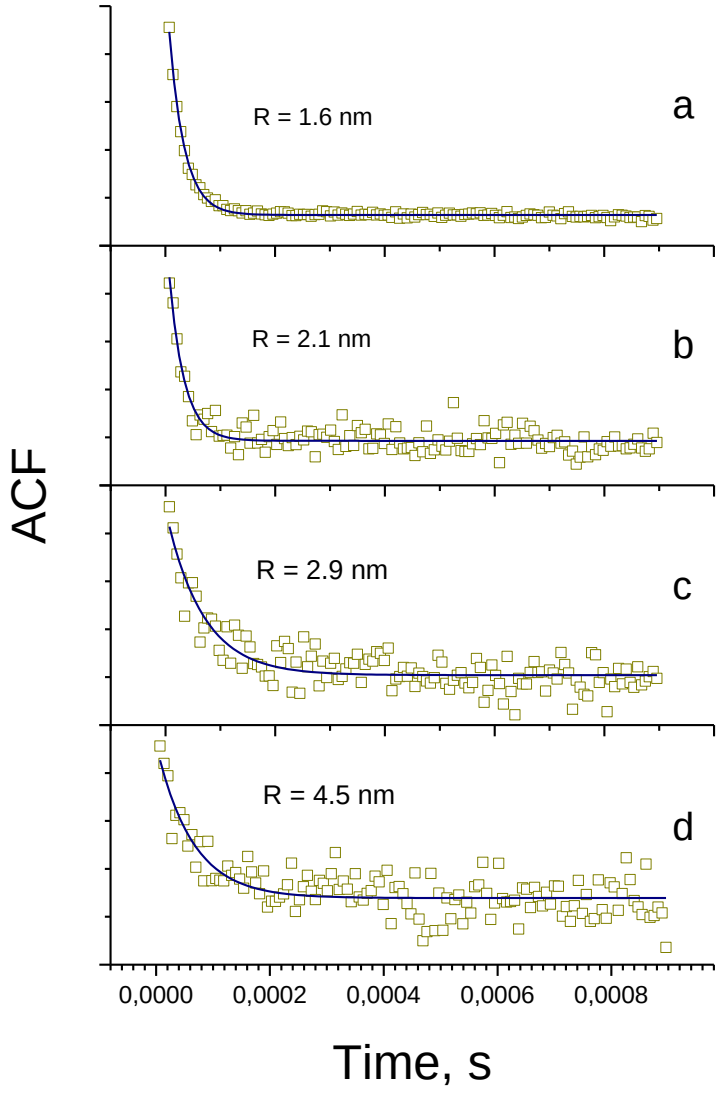

Figure 29 ACF curves of TOA, (a) and VTOA nanoparticles with vanadium content 2 mol% (b), 5 mol% (c) and 10 mol% (d). Preparation conditions: C_0 = 0.146 mol/l, n-propanol solvent, Re = 6000, T = 20◦C and H = 1.6 (a), 2.5 (b), 3.2 (c), 3.7 (d), Accumulation time 50 x 1 min.

Our DLS measurements in Figure 29 showed that the decay time of ACF curves increases with an increase of the vanadium content, which according to the Stokes-Einstein relation signifies an increase of the particles size (2R) and mass (m). At the same time, in contrast to the expected stronger light intensity (I) scattered from larger particles ($I \propto m^2$ in the Rayleigh domain $\lambda >> R$), the signal-to-noise ratio significantly decreased. This clearly indicates a decrease of the nanoparticle's concentration, once more surprising since the vanadium addition was relatively small (≤10 mol %) and the hydrolysis ratio was larger than that critical one h* = 1.5 needed for the homogeneous TOA nucleation (Azouani R., 2007). This can be explained by a competitive water consumption of Ti and V

precursors. Indeed, at the complete hydrolysis vanadium (V) precursor with d = 2 mol% can consume about all excessive water above that required for the TOA nucleation: 5d/100 = 0.1=H-h*; the hydrolysis of d = 10 mol% vanadium (V) precursor consequently decreases the free water concentration in the solution by 5d/100 = 0.5 mol% down to H'≈1.2 < h* suppressing TOA nucleation (Azouani R. *et al.*, 2007). This is supported by a progressive decrease of the signal-to-noise ratio of ACF curves in Figure 29 from a (d = 0) to d (d = 10 mol %). We notice that the faster hydrolysis kinetics of V species compared to that of Ti species agrees with the elements electronegativity on the Pauling scale: respectively 1.63 (V) and 1.54 (Ti). Based on these observations, conclusions can be drawn that (i) vanadium species effectively hydrolysed, strongly consuming free water in the solution, and preventing homogeneous TOA nucleation and (ii) mixed oxide VTOA particles nucleate owing to the condensation reactions between hydrolysed titanium and vanadium molecular bonds. Moreover, since only rare large VOA species appeared in the absence of the titanium precursor (iii) at d≤10 mol% TOA particles nucleate first, serving an attractor for hydrolysed vanadium molecular species; the nucleus size therefore increases with the vanadium content in the reactive solution. In contrast, (iv) at high vanadium concentrations above 20 mol% VOA species percolates by imprisoning sub-nucleus TOA species, which prohibits observation of the small nanoparticles.

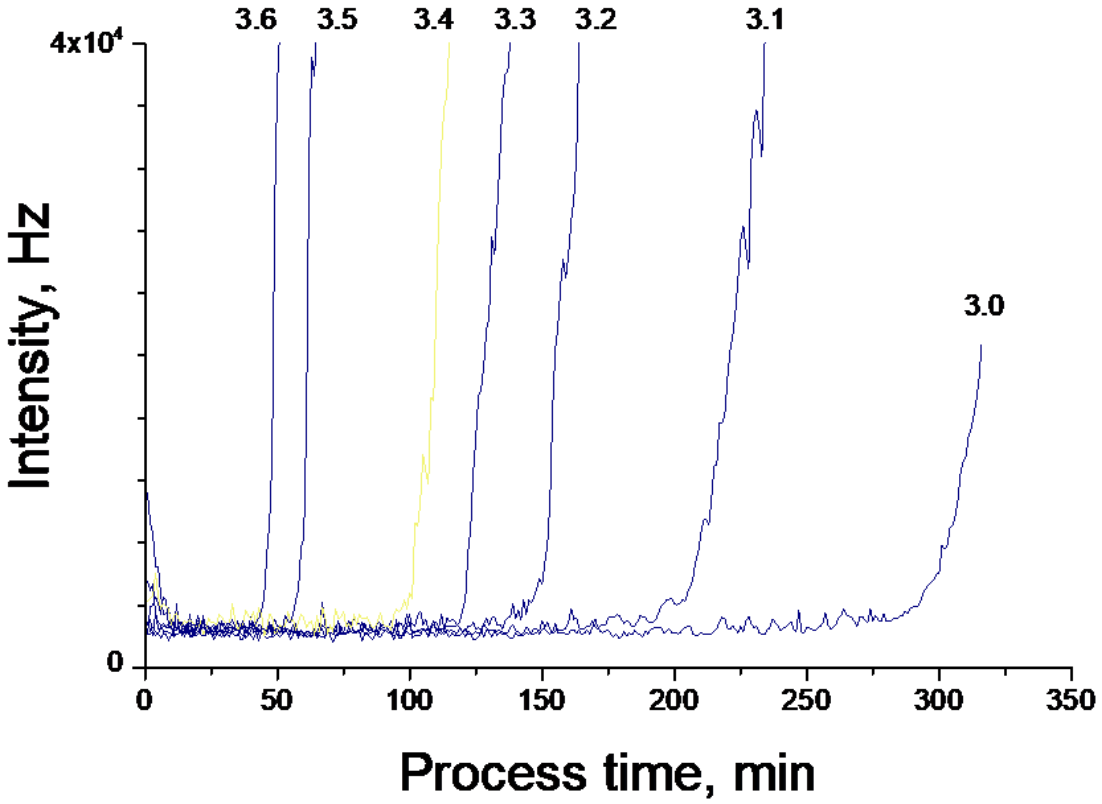

Figure 30 Scattered light intensity during induction period of VTOA nanoparticles growth (C0 = 0.15 mol/l, 2 mol% V, n-propanol solvent, Re = 6000, 20◦ C). Hydrolysis ratios are indicated. Accumulation time 1 min.

Further confirmation of the proposed hypothesis can provide measurements of the induction kinetics of the sol-gel process involving VTOA species. The solutions remained highly transparent during this common stage of the sol-gel process and became abruptly opaque at the end, indicating powder precipitation. The temporal evolution of the scattered light intensity in the solutions with 2 mol% V and different H is shown in Figure 30. In agreement with the general picture of the sol-gel process, the induction period t_{ind} shortened with an increase of H, which can be ascribed to agglomeration of metal oxo-alkoxy nanoparticles. In situ DLS measurements of the particles size shown in Figure 31 confirmed the appearance of nanoparticles and their slow growth during the induction period. The induction time t_{ind} can be empirically evaluated as a time when the scattered light intensity from the solution increases 5 times over that in the process beginning after the nucleation: $I(t_{tind}) = 5I(0)$ (Soloviev *et al.*, 2000).

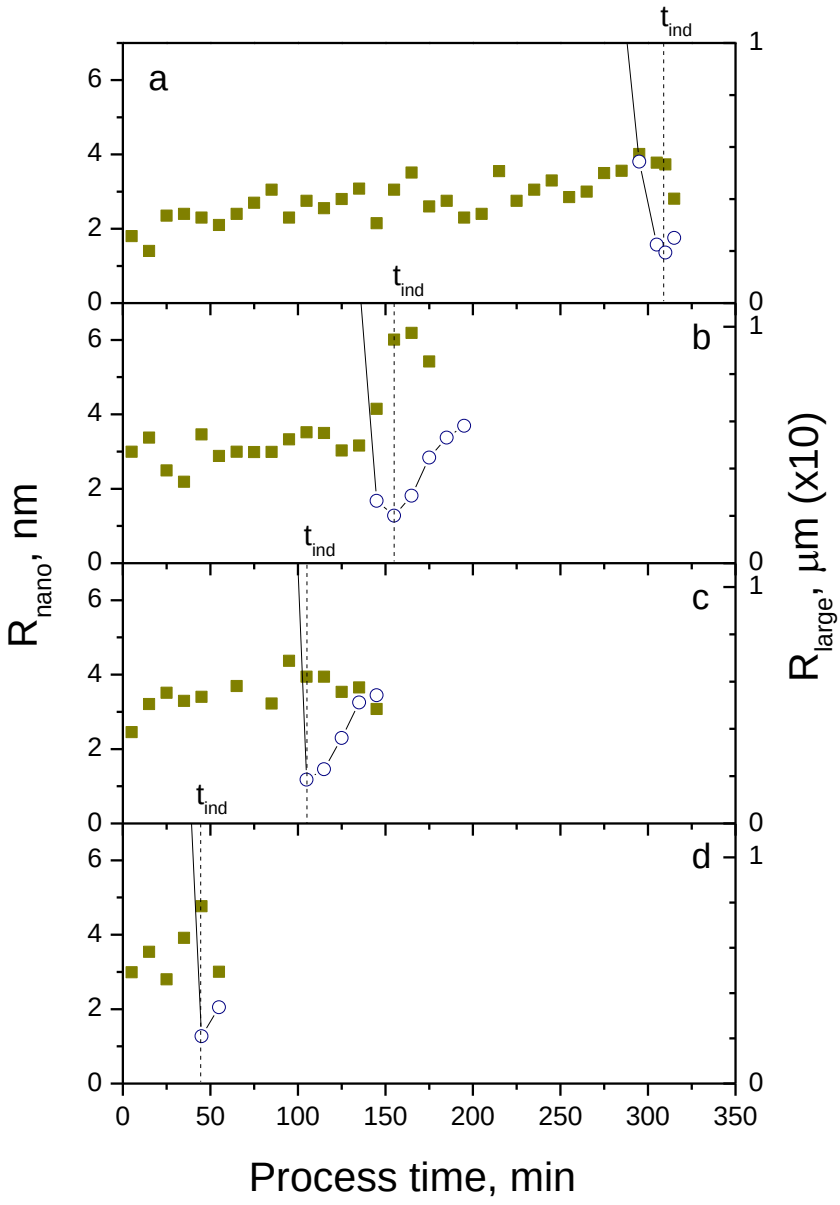

Figure 31 Evolution of radius of VTOA nanoparticles (Rnano,▪) and appearance of large agglomerates (Rlarge, ◦) on the induction stage of the growth. Preparation conditions: C0 = 0.15 mol/l, 2 mol% V, n-propanol solvent, Re = 6000, 20◦ C, and H = 3.0 (a), 3.2 (b), 3.4 (c) and 3.6 (d). Accumulation time 10 x 1 min.

At this moment the bimodal particle size distribution appeared, with the smallest particles being weakly aggregated nuclei and large particles of radius above 200 nm grown by feeding from the small nanoparticle's population. We notice that few very large (µm size) dust particles can contaminate the solutions at the early process times, which however do not affect the process kinetics. The attachment of small to large particles makes appearing the smallest nucleus fraction which is generally screened by the aggregates. This can be seen in Fig. 31 as an effective decrease of the small

particles size at $t > t_{ind}$. The correlation between the induction rate defined by rind =tin1 and initial slope of the particles growth kinetics dR/dt will be discussed below. The mechanism of the nanoparticle's agglomeration in the sol-gel process proposed by (Rivallin M. *et al.*, 2004) (Rivallin M. *et al.*, 2005) consists in n condensation between surface hydroxyls of two contacting nanoparticles:

$(\ldots) - OH^i + OH^i - (\ldots) \leftrightarrow / \rightarrow H_2O + (\ldots) - O^i - (\ldots)$

Which is partially reversible: the process is at equilibrium (↔) at i < k and becomes irreversible (→) after i ≥ k consecutive condensation steps, where k is the critical step. This sufficiently simple assumption has provided a successful explanation of the experimental induction rates empirically approximated by

$$r_{ind} \propto kC_{Ti}^{\beta}(H - h^*)^{\alpha}$$

Equation III-0-1

Where h* stands for the critical hydrolysis ratio, which permits nucleation. This h* corresponds to the condensation ratio of the smallest particle (nucleus) assembling about thousand atoms, which elementary chemical composition in case of TOA (h* = 1.5) can be represented by $TiO_{1.5}OR$. This model has been initially proposed for TOA species ascribing α = 2n-k-1 and β=α+1 with the solution in integer values n = 3 and k = 2 (Azouani R. *et al.*, 2007). Later, the validity of the model has been confirmed for ZOA and mixed oxide ZTOA (Cheng K. *et al.*, 2017) species.

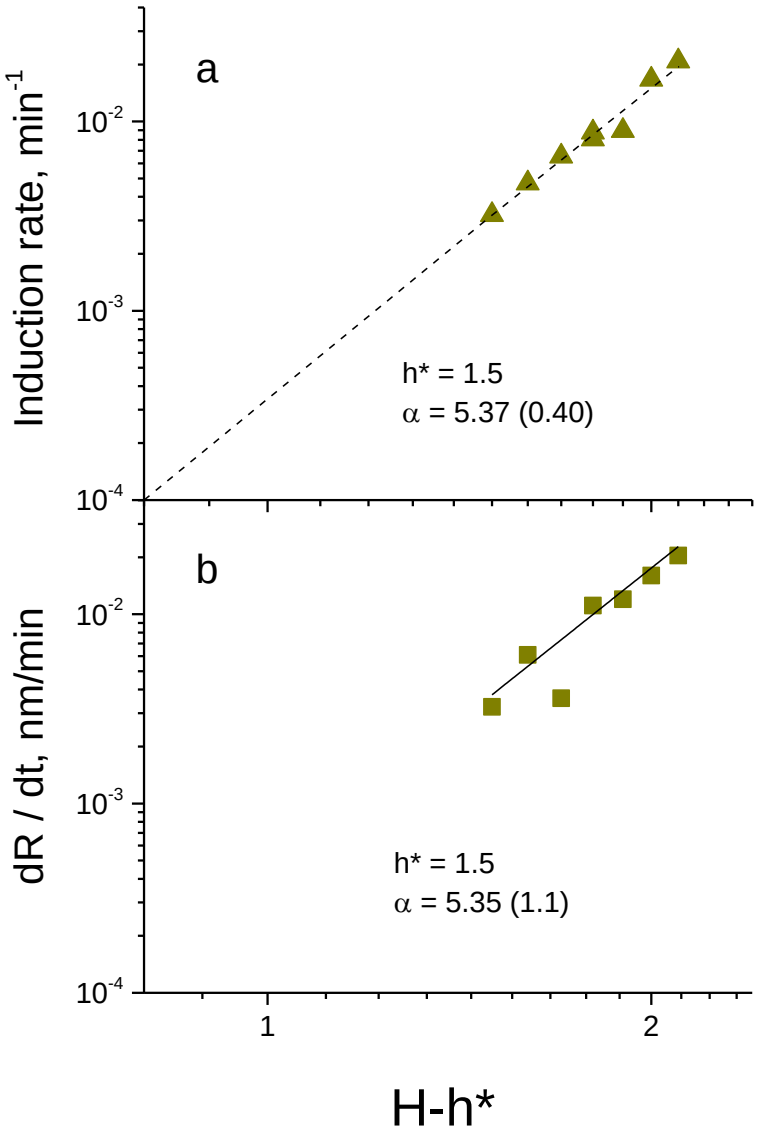

Figure 32 Induction rate (a) and rate of the particle growth (b) versus excessive hydrolysis ratio H-h* over critical one h* = 1.5, which leads to TOA nucleation (C_0 = 0.15 mol/l, 2 mol% V, n-propanol solvent, Re = 6000, 20◦ C).

The induction rate (r_{ind}) and nanoparticle growth (dR/dt) rates versus the overcritical hydrolysis ratio H-h* are plotted in the logarithmic frame in Figure 32a, and Figure 32b. In both cases, the power law was confirmed with h* = 1.5 and power factor α≈5, which are characteristic of the TOA nanoparticles aggregation and therefore support the assumption of TOA nucleation. However, absolute values of the induction rate were more that an order of magnitude smaller compared to those of TOA nanoparticles in similar experimental conditions. In fact, for H = 2.3 (which corresponds to H-h* = 0.8

in Figure 32) TOA induction rate of 0.1 min1 has been observed (Cheng K. *et al.*, 2017), while the extrapolation of our experimental data predicts the rate of ~10-4 min1, which according results in a much smaller induction rate of ~0.006 min1 in the experimental conditions with 2 times higher Ti precursor concentration (similar to that of VTOA). One can conclude that VTOA induction kinetics is significantly slower than that of TOA.

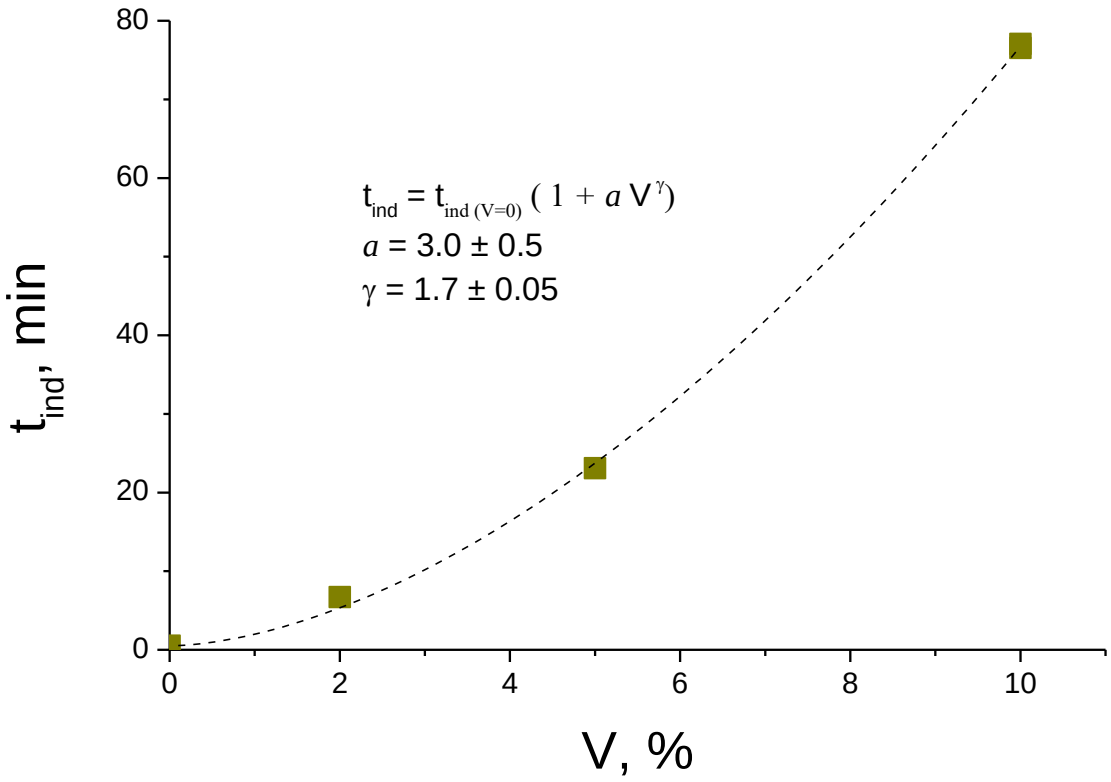

Figure 33 Dependence of induction time on V content (C_0 = 0.15 mol/l, H = 4.5, n-propanol solvent, Re = 6000, 20 °C).

In confirmation of this conclusion, Figure 33 shows measured induction times as a function of the vanadium concentration in the solution, which was clearly increased with an increase of CV. The least squared fit of the experimental data permitted to approximate the induction rates by a power law of CV and, consequently, rewrite the following equation as:

$$r_{ind} = k\, C_{\beta i}\, (H - h^*)^{\alpha}\, C_{V\gamma} / (c + C_{V\gamma})$$

Equation III-2

with α = 5, β = 6 and γ = 1.7 obtained from the experiment. While power factors α and β were explained in the model, physical meaning of the empirically introduced parameter γ must be understood. We also notice that the factor $1/(c + C_V^{-\gamma})$ was introduced in the previous equation to avoid singularity at $C_V = 0$.

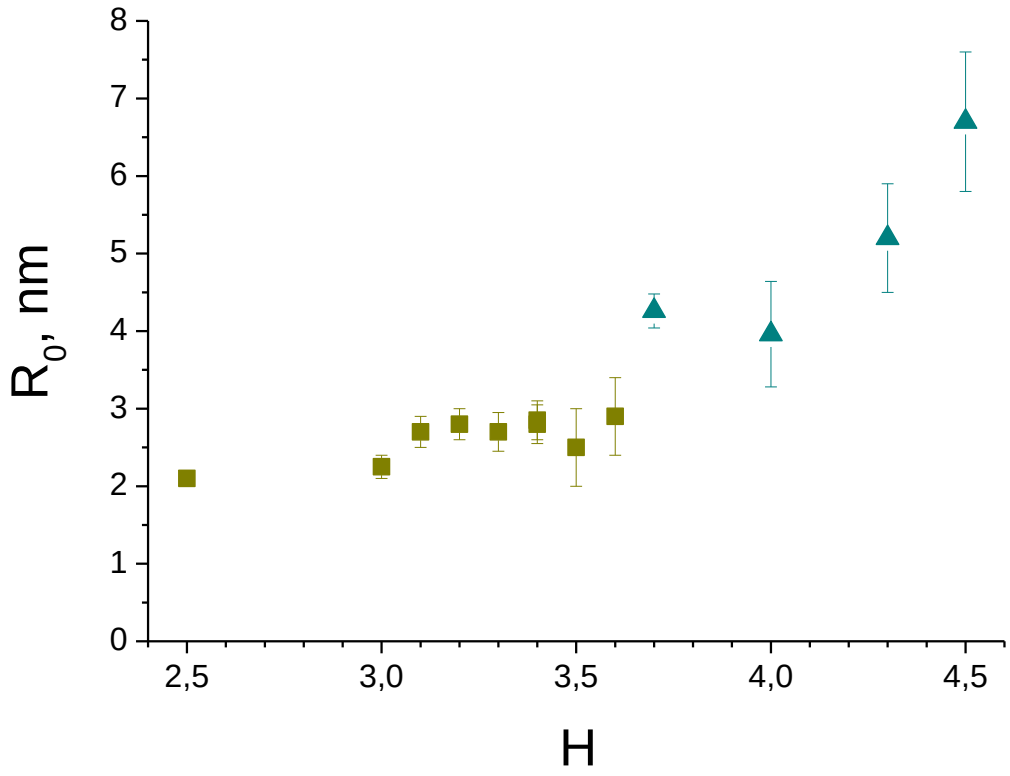

Figure 34 Initial radius of VTOA particles at the induction stage in n-propanol solvent with C0 = 0.15 mol/l and vanadium content of 2 mol% (▪) and 10 mol% (▲) (Re = 6000, 20◦ C).

The particle size underwent a small evolution with the water addition above the critical value h* = 1.5 enabling the nucleation. Two experimental series with 2 mol% and 10 mol% vanadium are shown in Figure 34. After 2 mol% V addition, the initial radius of the produced particles was about R0 = 2.1 nm for H ≤ 3.0 and seemingly increased by 0.4 nm with the following increase of H to 3.6. In contrast, the series with the higher vanadium content of 10 mol% showed significantly increased initial particle

radius of R0 = 4.3 nm. We notice rather large error bars in this last series, except for the first point accumulated for a long time from an almost stable solution (t_{ind}>6 h). According to the model (Rivallin M. *et al.*, 2004) (Azouani R., 2007), free water remaining after the nucleation stage promotes the particle aggregation; the influence of water content on size and composition of the elementary nucleus is almost negligible. Apparently, these smallest VTOA particles fit the nucleus definition, remaining stable with the moderate change of H. More confirmation to an assignment of the hydrodynamic radius 2.1 nm to VTOA nucleus provide experiments performed at a very low hydrolysis ratio close to the critical one, H = 1.6 presented in Figure 35. These series were performed with a higher precursor concentration 0.3 mol/l, to increase the nucleus number density, and the very long period of the colloid stability (almost infinite in our experimental conditions) permitted a long ACF data accumulation with a high signal-to-noise ratio. These results indicated that an addition of vanadium above 1 mol% in the sol-gel solution resulted in a stable nucleus of radius R_{nuc} = 2.1 nm, which corresponds to that measured in experiments at high H>>h* in the beginning of the induction period. The induction period can thus be assigned to the aggregation of VTOA nuclei, which confirms the general picture of the sol-gel process described by the Rivallin's model (Rivallin M. *et al.*, 2005).

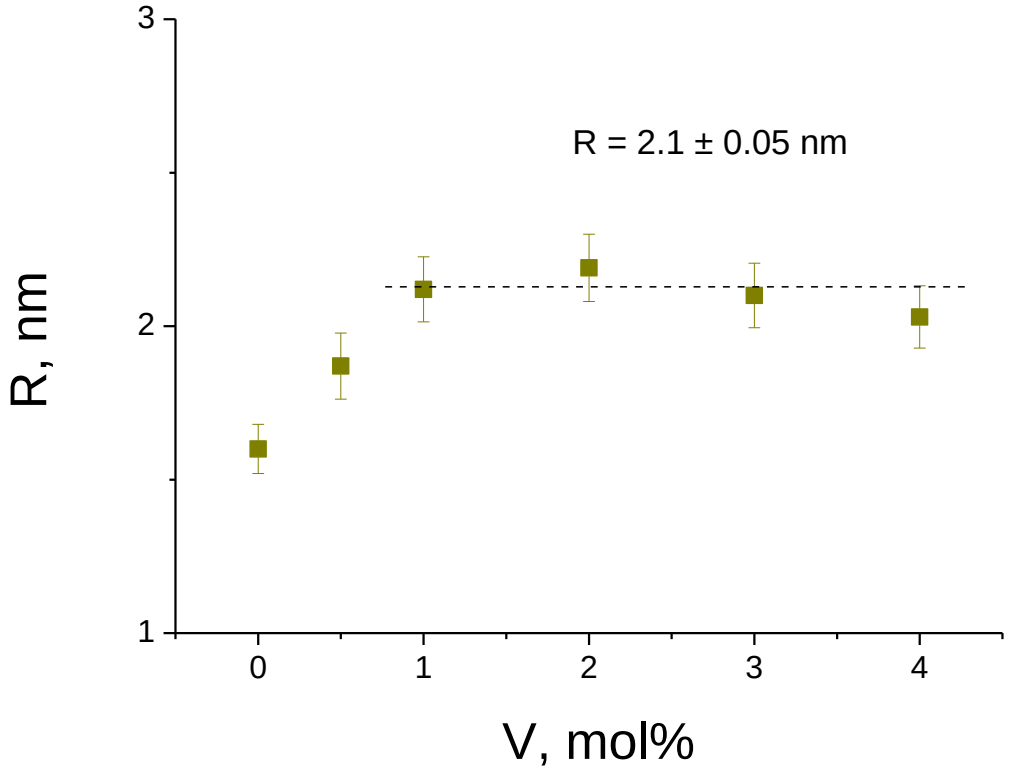

Figure 35 Radius of stable VTOA nanoparticles (nuclei) for different V content (C_0 = 0.3 mol/l, H = 1.6, n-propanol solvent, T = 20 ◦ C, Re = 6000).

A further inspection of the model predictions was realized in experiments with an increase of the total precursor concentration, by keeping fixed all other experimental conditions. The experimental SLS data presented in Figure 36 were realized with the vanadium content of 10 mol%, two hydrolysis ratios of H = 4.3 and 4.5 and the total precursor concentration increased from C_0 = 0.150 to 0.165 mol/l. The small difference in H in these series is explained by the very high sensitivity of the induction time to this parameter. The observed elongation of the induction period with the increase of H perfectly fitted the model prediction. On the other hand, the induction time was unexpectedly increased with the increase of precursor concentration by 25 ± 5 % in these experiments, which is in a seeming contradiction with the model predicted the induction time shortening at higher precursor concentration. The Rivallin's model is however based on the assumption about fixed nucleus size, which required verification in case of VTOA species. Our complementary DLS measurements showed an increase of radius of the initially formed VTAO nanoparticles with the increase of C_0 from R0 = 5.2

± 0.7 nm to 7.6 ± 0.7 nm (H = 4.3) and from 6.7 ± 0.9 nm to 8.8 ± 1.1 nm (H = 4.5). Considering the increase of a precursor concentration and nucleus volume, the nucleus concentration is expected to decrease by a factor of ~2.2. In these conditions, the equation predicts a slowing of the induction rates by ~30 %, which corresponds to the experimental observations. The performed experiments suggest that an empirically introduced parameter γ in equation (3) is linked to modifications of the nucleus size with an increase of the vanadium concentration. At the same time, the understanding of chemistry background for these modifications requires further studies.

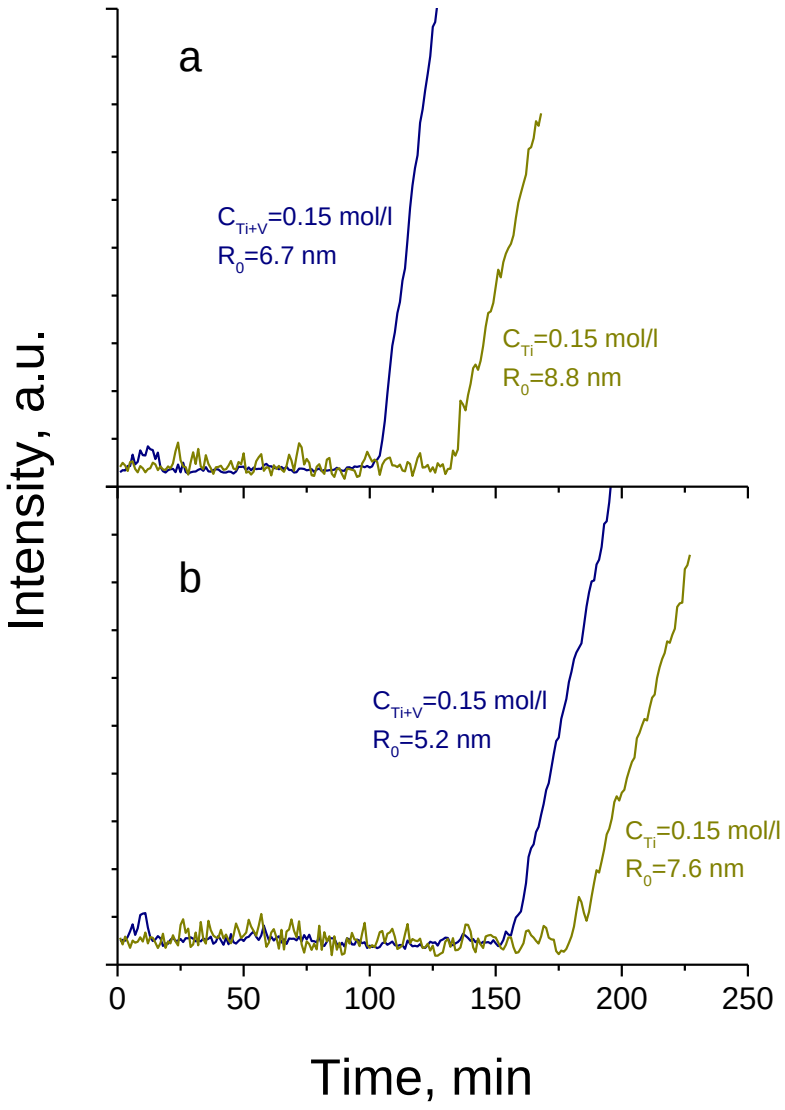

Figure 36 Scattered light intensity during induction period of VTOA nanoparticles growth (Ti:V = 9:1, 20◦ C) in n-propanol solvent at H = 4.5 (a) and H = 4.3 (b).

We point out that present results may serve first experimental validation of a new paradigm of the sol-gel process proposed by Kessler (Kessler V.G., 2009) in the range of relatively large oxo-alkoxy nanoparticles (R > 1 nm). They indicate that VTOA nucleus is adapting to the environment conditions: its size increases with an increase of water (weakly) and precursor (strongly) concentrations. This process, linked to structural modifications, may have consequences on the electronic structure and functional properties of the derivative solids. The work is in progress to provide more information about functional properties of the obtained mixed metal oxide solids.

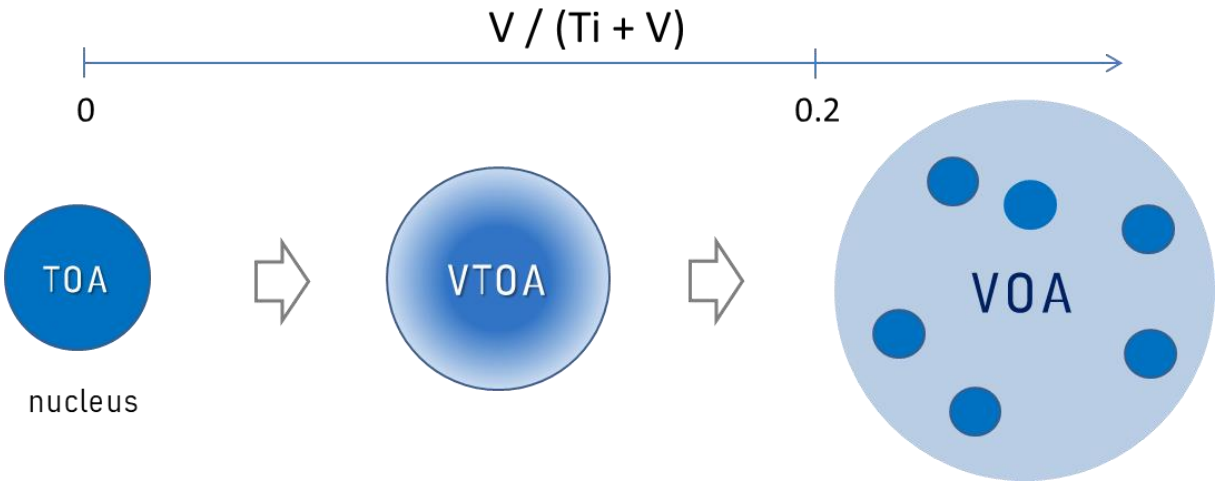

Figure 37 Scheme of VTOA species formation.

Based on the obtained results, the picture of the nucleation process is the following. At a small vanadium content ≤10 mol%, TOA nucleates accommodating hydrolyzed molecular species of VOA forming nucleus of size, which increases with an increase of the V/Ti ratio. In contrast, at a large vanadium content >20 mol%, hydrolyzed vanadium species trap sub-nucleus species of TOA, prohibiting the appearance of small nanoparticles; in these conditions large TOA-including VOA species with a poor defined size are formed. This picture is schematically presented in Figure 37. Because a net correlation between ZTOA nucleus composition, size and the crystalline phase of $Zr_xTi_{1-x}O_2$ solid solutions has been previously established (Cheng K. *et al.*, 2017), an absence of a well-

defined nucleus of VTOA for compositions x = V/Ti>0.25 also correlates with non-observed $V_xTi_{1-x}O_2$ solid solutions at the ambient pressure and temperature (Yang Y. *et al.*, 2017). Further studies in this field may emerge a valuable prediction method of stable nanocrystalline solids.

3.3 Conclusions

In conclusion, the mixed vanadium-titanium oxo-alkoxy (VTOA) nanoparticles were synthesized via sol-gel method in a rapid micromixing reactor, permitting point-like reaction conditions and narrowest particle size distribution. The particles nucleation and growth kinetics were monitored in situ via home-made monomode optical fibre probe, using static and dynamic light scattering methods. The vanadium addition worsened the coherent component of the scattered light prohibiting the particle size analysis at high vanadium content. However, at relatively low vanadium content ≤10 mol% an analysis of the experimental data permitted to conclude about nucleation of the mixed VTOA particles of 2.1 nm radius. We showed that titanium oxo-alkoxy (TOA) species appear first and serve to be centres of attraction for hydrolyzed vanadium oxo-alkoxy (VOA) species at the nucleation stage. In contrast, at high vanadium content VOA species percolate by imprisoning sub-nucleus TOA species prohibiting the nanoparticles appearance. This is connected to stronger hydrolysis and weaker condensation abilities of VOA species compared to TOA. The experimental VTOA kinetics at the induction stage agreed with the Rivallin's model and extended it to the case of non-conservation of the nucleus number density (under fixed total mass of the nuclei). The analysis of the experimental data validated an increase of the VTOA nucleus size with an increase of hydrolysis ratio (weak) and vanadium content (strong); this corresponds to a decrease of the nucleus number density in the reactive solution resulting in the unusual induction time lengthening. The experimental data support the new paradigm of the sol-gel process proposed by Kessler (Kessler V.G., 2009), which assumes a profound restructuring of oxometallic species during their association at the nucleation stage. This restructuring, quite appreciable in heterocationic species M_1M_2OA (M_1=M_2=Zr, Ti, V, etc.), can be followed at the particle's nucleation stage as a function of the elemental composition.

Chapter IV Preparation of mixed-oxide $V_xTi_yO_z$ photocatalyst

In this chapter the preparation of the V-TiO_2 photocatalysts with different vanadium concentrations will be described. Results of its characterization via TGA-TDA, XRD and Raman methods will be discussed.

4.1 Preparation of the powders

The mixed oxide V-TiO_2 nanoparticles with different vanadium content V/(V+Ti) between 0 and 20 mol% were prepared in a laboratory chemical reactor with ultrarapid micromixing of the titanium and vanadium precursors, followed by the reactive colloid deposition on glass beads and heat treatment. The vanadium-titanium-oxo-alkoxy (VTOA) nanoparticles were generated using sol-gel method. The two stock solutions (each of 50 mL) injected into the reactor contained respectively A) mixed vanadium oxytripropoxide (98%, Sigma Aldrich) and titanium tetraisopropoxide (TTIP, 98%, Sigma-Aldrich) precursors in n-propanol (99.5%, Sigma Aldrich) and B) twice filtered distilled water (syringe filter 0.1 µm porosity PALLs Acrodisc) in n-propanol. The titanium precursor concentration in the reaction volume was C_{Ti}=0.3 mol/l and water concentration C_w was adjusted in order to maintain the hydrolysis ratio $H=C_w/(C_{Ti}+C_V)=1.5$, which according to our previous results assures the particles nucleation but prohibits their mutual aggregation and growth. The reactor was maintained at the temperature of 20.0 °C using a thermo-cryostat Haake DC10K15. The reactor operated at the Damköhler number Da≤1, which means that the reaction medium was perfectly homogeneous before the chemical reactions leading to nucleation of species occurred, which permits the narrowest polydispersity of the produced nanoparticles. To prepare the powders for their analysis, the solution obtained from the T-Mixer was left under a hood for 24 hours until all the alcohol dried up, remaining only the desired powders, after obtaining the powders, they were put under heat treatment at 450° C at 4 hours. The following Table 2 indicates the molar concentration used in the present experiments:

%Ti	%V
100	0
99.5	0.5
99	1
98	2
97	3
95	5
93	7
90	10
85	15
80	20

Table 2 V-TiO_2 molar concentrations.

4.2 Results and Discussion

As we have recently shown (Sanchez Mendez M. *et al.*, 2019), at a relatively low V content of ≤0.20 mol% the VTOA nanoparticles are formed via the condensation of titanium oxo-alkoxy (TOA) species, which attract hydrolyzed vanadium species at the surface. In contrast, at the higher V content above 20 mol% the hydrolyzed vanadium oxo-alkoxy (VOA) species imprison subnucleus condensed TOA species prohibiting the nucleation. The obtained species in this range of vanadium loadings are not well defined: they appear to be strongly polydispersed with the size exceeding 1 μm. Moreover, our data indicate the solubility limit of vanadium in TOA ~15-20 mol% V (Sanchez Mendez M. *et al.*, 2019). To keep the material in the most photocatalytically efficient anatase crystalline phase, the vanadium content in these studies was limited to 20 mol%.

The results of TGA-TDA measurements of the prepared nanopowder probes identical to nanocoating samples from Table 2 are shown in Figure 38. In all presented patterns, the broad endothermic peak between 50 °C and ~200 °C with the maximum at 150 °C was observed, which is due to desorption of solvent release from the particles surface, followed by another broad exothermic band with the maximum at ~250 °C due to the residual organics burning. We can notice comparable fractions of the desorbed surface species in the mixed oxide and pure titania nanoparticles, which indicates a comparable retention of the adsorbed solvent and, by consequence, similar specific surface area of

the produced nanomaterials. We would like to attract an attention to significant modifications of the strong exothermic peak due to the anatase phase crystallization, which appeared at T_c=414 °C in pure titania (Figure 38a). When even a small amount of vanadium of 0.5 mol% was introduced to the system, the crystallization peak broadened and shifted to the low temperatures of 382 °C. Further on, at 1% mol% V it flattened (almost vanished). At 2 mol% V this peak reappeared, progressively intensified, narrowed, and shifted back to higher temperatures, attaining T_c=440 °C at 20 mol% V. This modification clearly shows a strong interaction of vanadium atoms with TiO_2 host matrix.

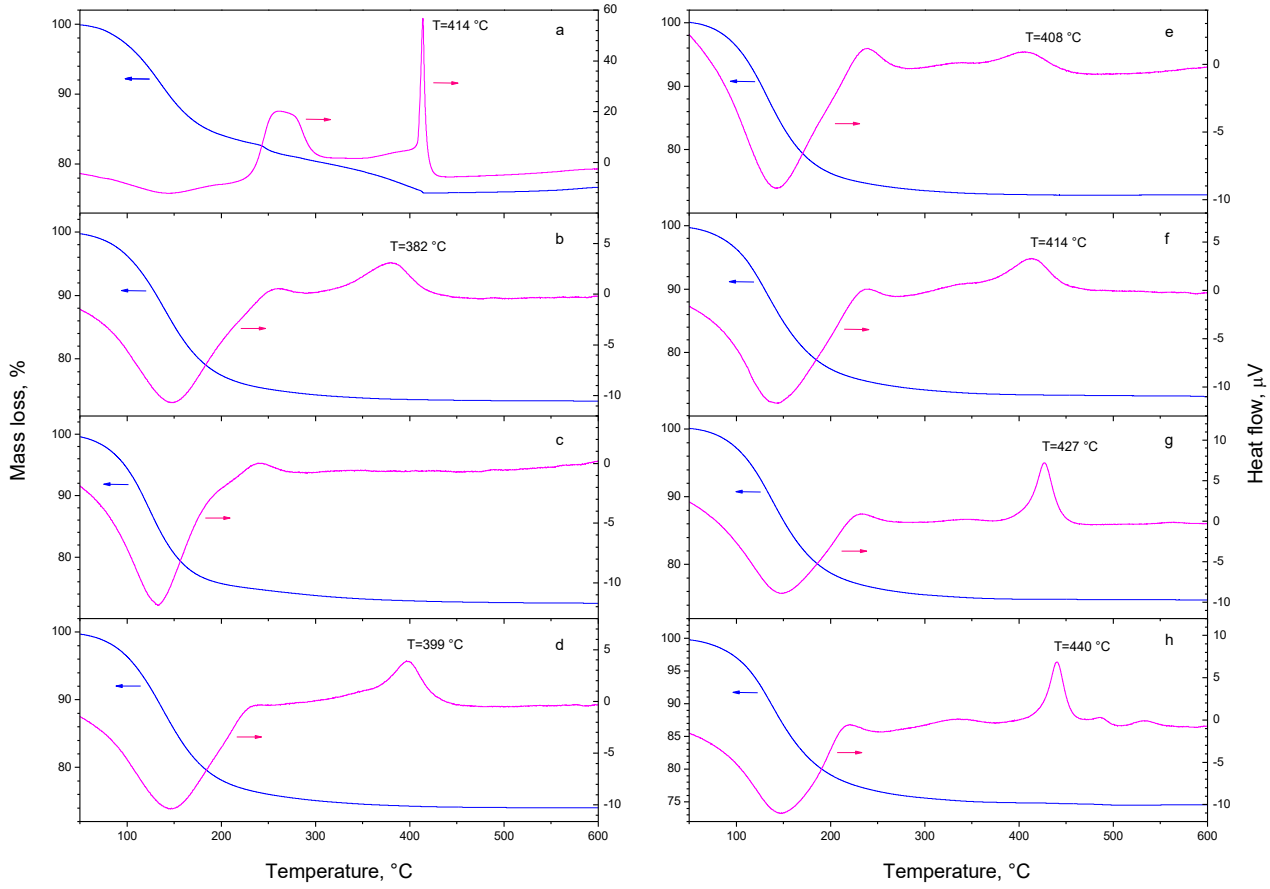

Figure 38 TGA (left axis) and TDA (right axis) measurements of V-TiO_2 samples with 0 (a), 0.5 (b), 1 (c), 2 (d), 5 (e), 7 (f), 10 (g) and 20 (h) mol% vanadium content.

A very limited number of TGA-TDA measurements of V-TiO_2 mixed oxide materials exists in literature. The most relevant one to our studies has been published by (Shao G. N. *et al.*, 2015), who

synthetized V-TiO_2 powder via sol-gel method. They have reported in V-TiO_2 powder with 5.8 mol% V the principal mass loss due to the solvent/water desorption below 300 °C associated with endothermic heat flow followed by a broad exothermic band with the maximum at ~250 °C due to the residual organics burning, which agree with our results. A broad exothermic peak associated with the material crystallization between 380 and 560 °C has been observed in these studies, which merged anatase, brookite and rutile phase transitions. Unfortunately, no detailed analysis of samples with different vanadium content has been presented in the earlier studies. The well-resolved exothermic crystallization peak observed in our studies, which shifted with an increase of the vanadium content (see Figure 38), was attributed by us to the produced size-selected V-TiO_2 nanoparticles in strict micromixing conditions of the laboratory chemical reactor (Azouani R. *et al.*, 2010).

According to the above TGA-TDA measurements, the heat treatment temperature of 450 °C is sufficient to crystalize all prepared samples from Table 2. Therefore, in the following XRD analysis was performed on probes heat treated at 450 °C for 4 hours. Here, we are interested in the modification of the structural and microstructural characteristics of the V-TiO_2 samples in function of the initial V molar percentage. To do this, high quality XRD powder patterns were recorded on a wide 2theta range (10-110°) with a short 2theta step (0.02°) and a high counting rate (384s per step). Measurements were done in collaboration with Dr. Capucine Sassoye and Mohamed Selmane from the Laboratoire de Chimie de la Matière Condensée de Paris (UMR CNRS 7574) on D8 Discover equipped with a Copper source ($K_{\alpha1}$ = 1.54056 Å: $K_{\alpha2}$ = 1.54439 Å, I_2/I_1 = 0.5) and a Lynxeye XE-T detector (1D mode). The XRD patterns of V-TiO_2 nanopowders samples with various vanadium content (in mol%) are shown in Figure 39.

The pure anatase phase was observed in all prepared samples, except for the one synthesized with 20 mol% vanadium, which is biphasic with the contribution of both TiO_2 anatase phase and α-V_2O_5 orthorhombic phase. This feature means that Vanadium is inserted in the anatase up to 10 mol% without major structural modification and without demixion. For higher mol%, the excess of

vanadium crystallizes into α-V_2O_5. For the pure TiO_2 sample, we can notice a large and low intensity bump in the 2theta range from 28° to 35° which could be related to a residual amorphous TiO_2 phase. This contribution could be related to an uncompleted crystallization of the sample. We also notice a very weak brookite peak appeared in samples with 2, 3 and 5 mol% V content, which agrees with XRD patterns reported by (Shao G. N. *et al.*, 2015) in V-TiO_2 sol-gel powders heat treated at 450 °C; this peak weakened at higher vanadium contents. The Scherrer size of the brookite domain ~5 nm ($\Delta 2\theta$=1°) corresponds to that of elementary V-TiO_2 nucleus (Sanchez Mendez M. *et al.*, 2019), while that of anatase domain ($\Delta 2\theta$=0.3°) to that of the coating width (15-20 nm); this permits to suppose that the smallest (occasionally not sintered) V-TiO_2 nanoparticles crystallize into brookite phase. Complementary measurements are required to verify this assumption. For all the samples, the peak width remains relatively large after the heat treatment at 450 °C confirming the small size of the nanoparticles. To confirm the above conclusions, Rietveld refinements were performed which permit obtaining more precise structural and microstructural information.

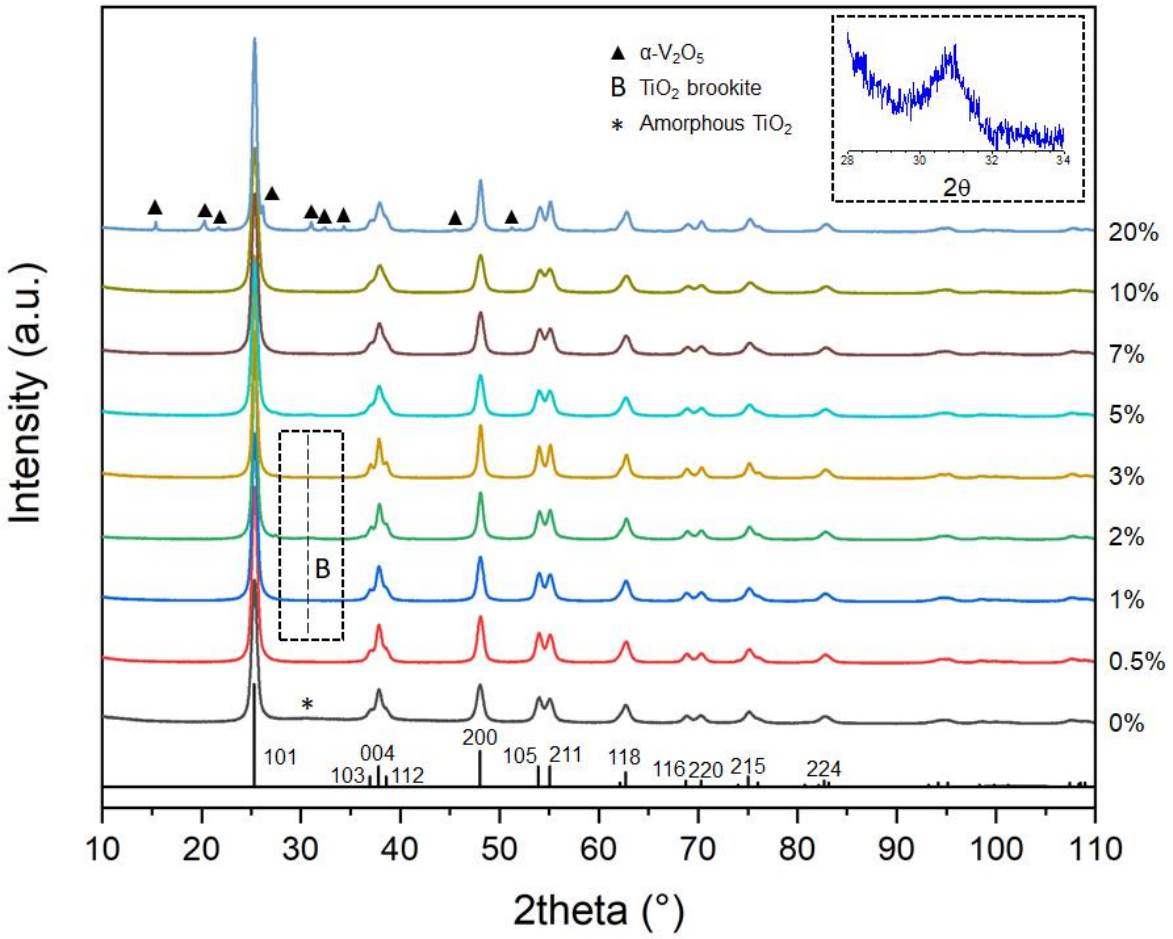

Figure 39 XRD patterns of V-TiO_2 samples with different vanadium content (in mol%). Vertical bars show positions and heights of anatase TiO_2 peaks. Brookite phase of TiO_2 (B) and orthorhombic phase of V_2O_5 (▲) are indicated.

The structural and microstructural parameters extracted from the Rietveld type refinement procedure are summarized in Table 3. These parameters correspond to a negligible number of strains in all V-TiO_2 samples. The nanoparticle size was the main contribution to the peak enlargement. A typical result of the fitting procedure for the sample with 1 mol% V shown in Figure 40 confirms, as expected, the anatase structure of V-TiO_2 lattice.

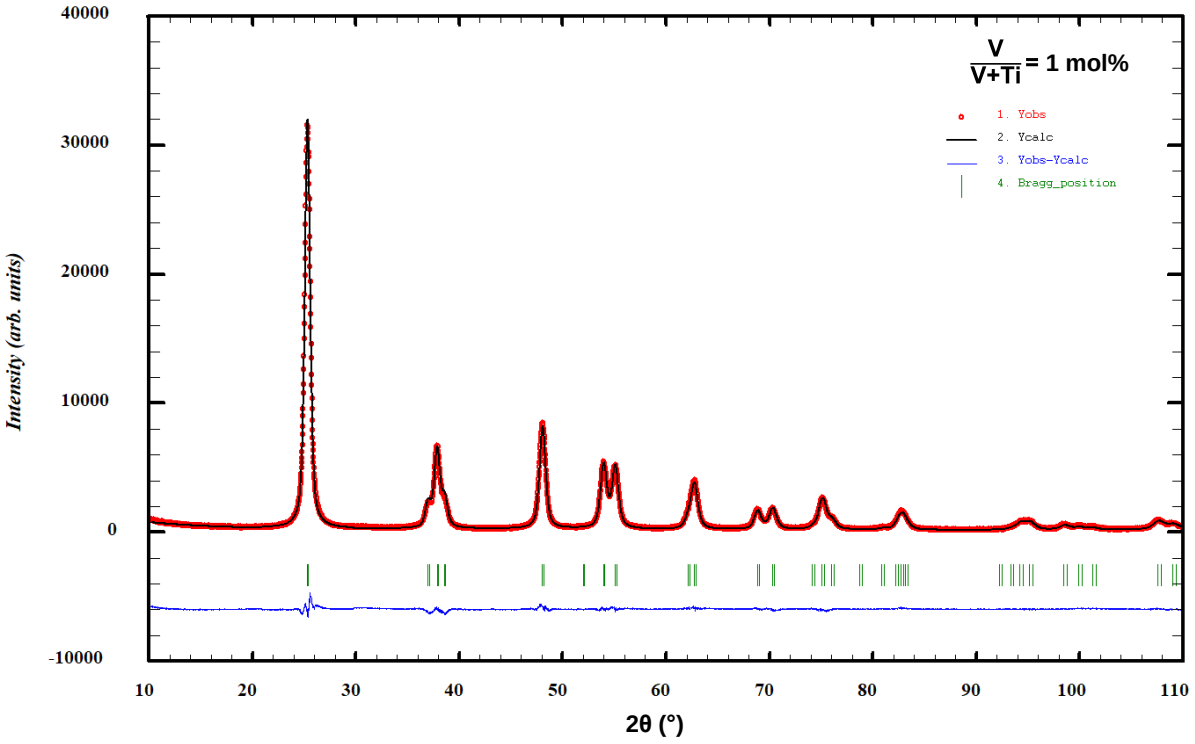

Figure 40 XRD powder patterns and Rietveld refinement with the anatase model for V-TiO_2 sample with 1 mol% of Vanadium.

For all the samples, we observe that the cell parameters (a, c) remain constant, respectively around a = 3.78 Å and c = 9.50 Å, which are in good agreement with the one expected for the anatase structure. No major structural modifications were thus highlighted when the mol% of vanadium increased. For the 20 mol% V sample, the refinement was performed considering the presence of α-V_2O_5. The phase percentage was thus estimated around 90 % for anatase TiO_2 and 10% for α-V_2O_5, which corresponds to the 10 mol% V still being inserted into TiO_2 matrix and the remaining 10 mol% V segregated into α-V_2O_5. This set the solubility limit of V atoms into anatase TiO_2 nanopowders to ~10 mol%, which is in a general agreement with expectations, while remains sensibly lower than the previously reported data of 21 mol% (Le Roy D. *et al.*, 2012). This decrease of solubility in nanomaterials is not surprising. In fact, considering that in 5-nm particles about 50 % of cationic sites belong to the surface, one can conclude that a half of the inserted vanadium atoms in 20 mol% V sample appear at the surface and, therefore, tend to form α-V_2O_5 domains at the heat treatment. Further investigations via Transmission Electronic Microscopy, could be interesting to perform to

characterize the V segregation phenomenon when the solubility limit is exceeded, that is between 10 and 20 mol% V.

An interesting trend can be also observed in the anatase crystalline size evolution with vanadium content within the solubility range: the size sharply increased at 2-3 mol% V, where brookite phase appeared, and remained twice smaller at the higher and lower vanadium contents. Furthermore, for 20 mol% V, which corresponds to the TiO_2/V_2O_5 phase segregation phenomenon, the particles coarsen to attain the size of ~18 nm. Concerning the α-V_2O_5 particles size, it appears to be far bigger than that of TiO_2, which supports our previous conclusions about the precursor VTOA species nucleation in the sol-gel process (Sanchez Mendez M. *et al.*, 2019).

Structural and microstructural parameters	**TiO_2 anatase[(1)]**	**Determined by refinement**							
		V/(V+Ti)							
		0%	**0.5%**	**1%**	**2%**	**3%**	**5%**	**7%**	**10%**
Cell parameters a, b (Å)	3.79	3.788	3.784	3.785	3.783	3.784	3.785	3.784	3.784
Cell parameters c (Å)	9.50	9.504	9.505	9.503	9.493	9.501	9.503	9.498	9.491
Apparent Size (nm)	/	12.0	12.9	13.4	20.4	21.5	11.5	11.4	10.7

Structural and microstructural parameters	**TiO_2 anatase[(1)]**	**α-V_2O_5[(2)]**	**Determined by refinement**	
			V/(V+Ti)	
			20%	
			TiO_2 Anatase	**α-V_2O_5**
Cell parameters a (Å)	3.79	11.51	3.784	11.512
Cell parameters b (Å)	3.79	3.56	3.784	3.565
Cell parameter c (Å)	9.50	4.37	9.491	4.382
Apparent Size (nm)	/		17.8	48.5
Phase percentage			89%	11%

Table 3 Rietveld analysis of V-TiO_2 nanopowders. Reference data: (Rezaee M. et al, 2011) (1), (Enjalbert R. and Galy J., 1986) (2).

In order to follow crystallization of the material with the highest level of vanadium, close to the expected solubility limit of 21 mol% (Le Roy D. *et al.*, 2012) we performed XRD measurements on 20 mol% V probes treated with different temperatures from 300 to 1000 °C during 4 hours. The results are shown in Figure 41. The XRD patterns after heat treatment below 400°C showed an amorphous state of V-TiO_2 material. At 500°C we observed the anatase phase related to TiO_2, which transformed

to pure rutile at 700 °C and higher temperatures. At the same time, we observed many peaks of a smaller intensity at 600 °C (a very weak contamination of XRD patterns by these peaks can be also noticed after heat treatment with 500 °C and 700 °C). These peaks more probably belong to the orthorhombic α-V_2O_5 phases, which would indicate the material segregation at intermediate heat treatment temperatures; in contrast, the dissolution of vanadium in anatase and rutile titania takes place at respectively lower and higher temperatures. The mechanism of this phenomenon is not clear now. Alternatively, these peaks may be due to a metastable $V_xTi_yO_z$ solid, which decays after its formation at high temperatures. More work is required to understand their origin.

Our observations of the anatase crystalline cell stability with an addition of vanadium agree with those of (Khan M. *et al.*, 2013), who have studied V-doped TiO_2 with V/Ti ratio of 1-5 mol% synthesized by hydrothermal method: the positions and intensity of XRD peaks in this study was found unchanged, which shows that crystallinity is not significantly affected by the V. We notice no appreciable weakening of anatase XRD peaks in our samples with an increase of vanadium content, which disagrees with that reported by (Ren F. *et al.*, 2015) in V-doped TiO_2 prepared via solid state sintering method and explained by a poor crystallization of powders. Our result also disagrees those of (Zhou W. *et al.*, 2010) reporting that vanadium doping restrains the crystal growth and promotes the phase transition from anatase to rutile compared with pure titania.

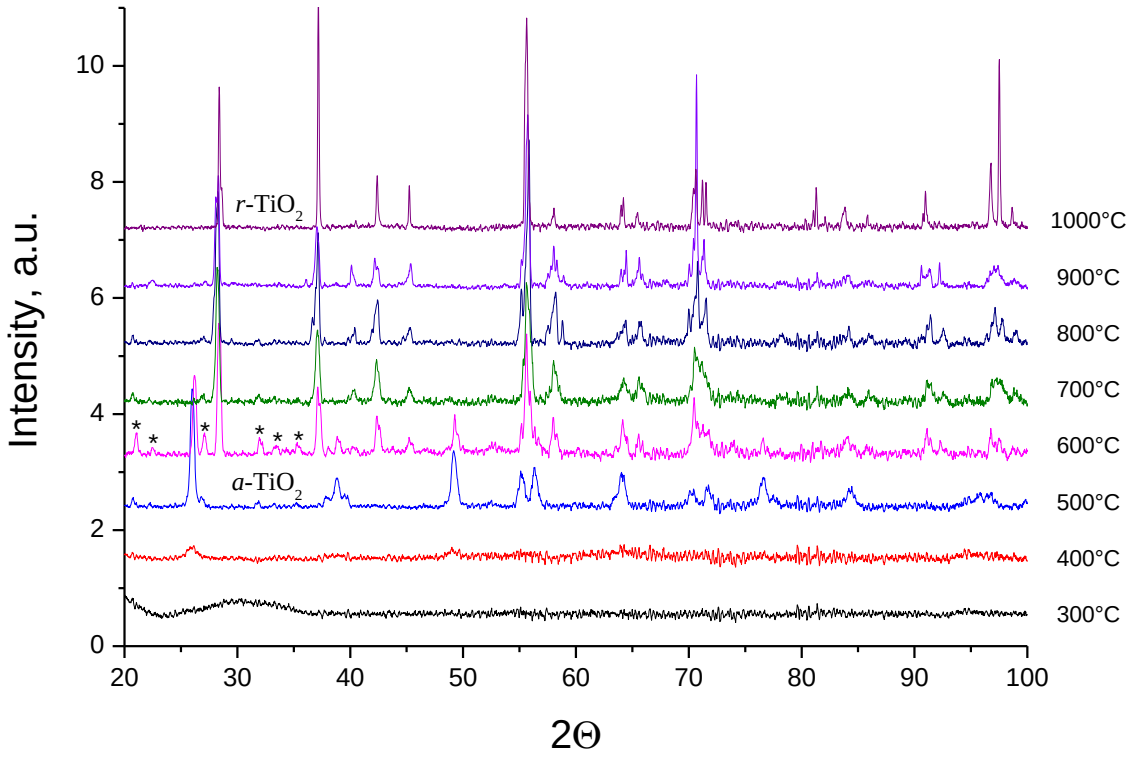

Figure 41 XRD powder patterns of V-TiO_2 samples with 20 mol% vanadium content heat treated at different temperatures for 4 hours.

The Raman spectra of V-TiO_2 samples with different vanadium content, calcinated at 450 °C for 4 hours are shown in Figure 42. The spectra with 0, 0.5, 1, 2, 5 and 7 mol% V showed frequencies of the bands maximum at 147 cm^{-1} (E_g), 198 cm^{-1} (E_g), 396 cm^{-1} (B_{1g}), 515 cm^{-1} (A_{1g} /B_{1g}) and 637 cm^{-1} (E_g), which correspond to anatase TiO_2, in agreement to literature (Balachandran U. and Eror N.G., 1982). At the same time, samples with 10 and 20 mol% V showed significant deviations: the band at 515 cm-1 weakened while the bands at 396 cm-1 and 637 cm-1 shift respectively to high and lower frequencies and new bands appeared at 280 cm-1, 300 cm-1 and 690 cm-1. These modifications correspond to the short-range structural rearrangements. We notice that according to the XRD pattern in Figure 39, TiO_2 with 20 mol% V after calcination at 450 °C contained a small amount of orthorhombic phase of V_2O_5, which could explain for these modifications (Shvets P. *et al.*, 2019).

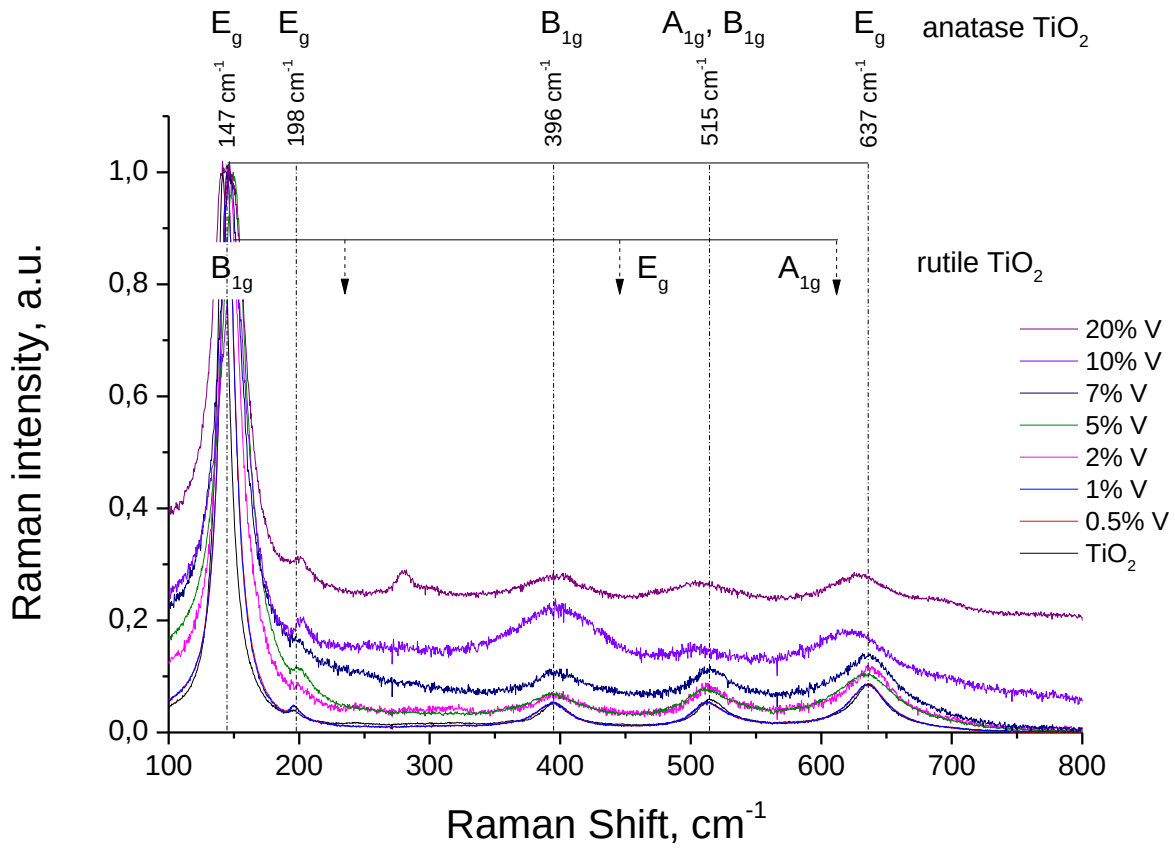

Figure 42 Raman spectra of V-TiO_2 samples with different vanadium content. The positions of anatase and rutile TiO_2 bands are indicated by vertical dashed lines.

The Raman spectra of V-TiO_2 samples with 20 mol% V heat treated at different temperatures are shown in Figure 43. These samples were calcinated at temperatures starting from 300 °C to 1000 °C every 100 °C making a total of 8 samples of 20 mol% vanadium. The positions of bands in samples calcinated at 300 °C, 400 °C and 500 °C correspond to anatase TiO_2, while those ibn samples calcinated at temperatures above 700 °C to rutile TiO_2. In contrast, samples heat treated at 500 °C, 600 °C and 700 °C showed more complex spectra. Three new unassigned bands appeared at 281 cm^{-1}, 300 cm^{-1} and 696 cm^{-1}, which can be connected to the unassigned XRD peaks in Figure 41. We notice in this connection, that (Ren F. *et al.*, 2015) have observed in V-TiO_2 a weak peak in the frequency range ~280 cm^{-1} attributed to V_2O_5 with an increased vanadium contents up to 5 and 10 mol%; however, the applied method does not guarantee perfect V-elemental dispersion in the host matrix, which may result in the vanadium oxide clustering at high loadings. In contrast, segregation

of titania and vanadia materials seems unlikely in our preparation conditions, which allows us to disregard (at least, at this state of studies) this hypothesis. More work is required to understand the new phase appearance.

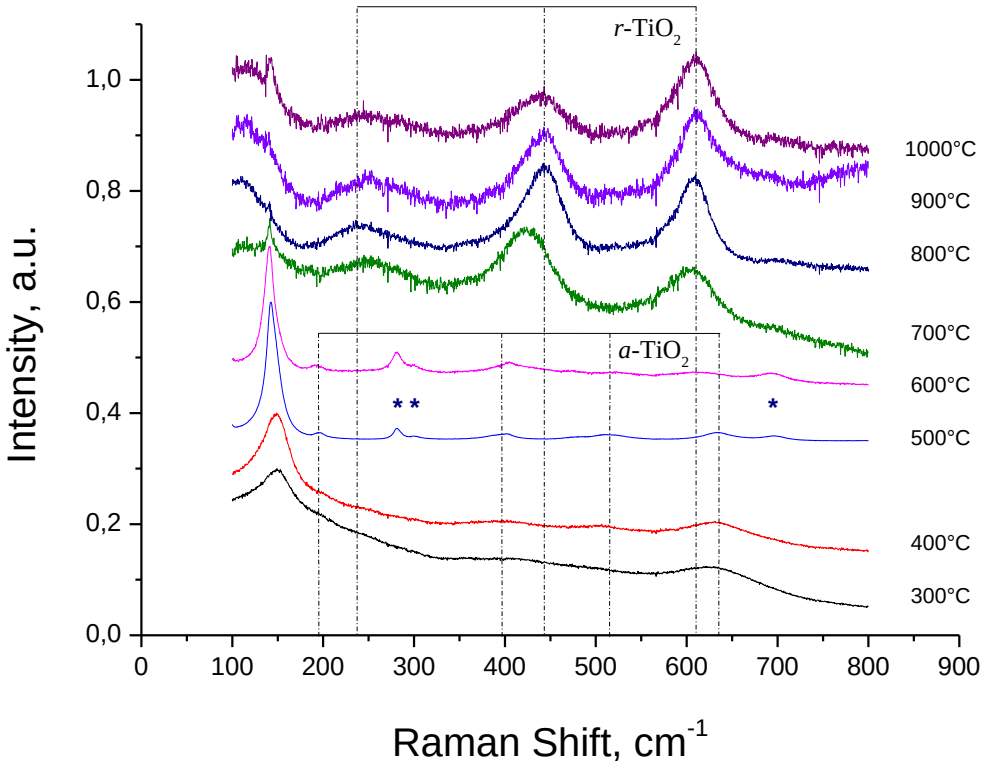

Figure 43 Raman spectra of V-TiO_2 samples with 20 mol% vanadium content heat treated at different temperatures for 4 hoirs. Positions of anatase and rutile TiO_2 bands are indicated by vertical dashed lines. Stars indicate unassigned bands.

4.3 Conclusions

In this Chapter, the structure of V-TiO_2 samples in form of nanopowders with different vanadium content from 0 to 20 mol% was studied. The TGA-TDA measurements showed a complex behavior of the material resulting in a significant dependence of the anatase phase transition temperature with the V content, which evidenced perfect insertion of V into the host TiO_2 matrix. The heat treatment at 450 °C of V-TiO_2 nanoparticles with the vanadium content below 20 mol% resulted in the

formation of anatase crystalline structure, which is identical to that of pure TiO_2; the Rietveld analysis of XRD patterns evidenced no significant deviation of the anatase structure parameters. Furthermore, traces of brookite titania were observed at 2-3 mol% V loading. An interesting trend can be also observed in the anatase crystalline size evolution with vanadium content within the solubility range: the size sharply increased at 2-3 mol% V, where brookite phase appeared, and remained twice smaller at the higher and lower vanadium contents. Furthermore, for 20 mol% V, which corresponds to the TiO_2/V_2O_5 phase segregation phenomenon, the particles coarsen to attain the size of ~18 nm. Concerning the α-V_2O_5 particles size, it appears to be far bigger than that of TiO_2, which supports our previous conclusions about the precursor VTOA species nucleation in the sol-gel process (see Chapter 3).

An increase of the heat treatment temperature showed a progressive transformation of anatase to rutile structure, as confirmed by XRD and Raman measurements. In contrast, new unassigned peaks (XRD) and bands (Raman) appeared at the intermediate temperatures between those characteristics of anatase and rutile phases crystallization: T_c = 600 $\pm$ 100 °C. There peaks may belong to a metastable phase of $V_xTi_yO_z$ solid decaying after formation at high temperatures. More work is required to identify this phase and relate it to the preparation method, which is specific to small size (nanoscale) and elemental homogeneity (due to micromixing conditions in chemical reactor).

Chapter V Photocatalytic Experiments with UV-VIS and Visible Light

In this Chapter, photocatalytic activity of mixed oxide V-TiO_2 nanoparticulate coatings, which preparation was described in previous chapters, will be analyzed under UV and Visible light illumination.

5.1 Experimental Setup

The photocatalytic experiments are described in the following sub-chapters, in order to understand the different steps of the experiments involving photocatalytic activity. We will start by describing the reactor on which the experiments were performed, we will describe the different lamps used during the experiments, then the preparation of the methylene blue solution and for last how the coated glass beads were prepared.

5.1.1 Photocatalytic Reactor

The experimental reactor consisted of an immersion well reactor made of Quartz glass tubes. The artificial light was fixed inside the inner tube while 90 grams of 4 mm in diameter glass beads coated with the photocatalyste were put in the annular space between the external and internal tube. An aqueous solution containing 5 ppm of methylene blue (MB) used as pollutant was prepared for each run. In every run a volume of 400 mL was used, A peristaltic pump was used to circulate this solution in a close loop by the bottom of reactor to submit it to the photocatalytic action of the coated beads under the light shining from the inner tube. Tests were performed to determine that this tube absorb negligible part of the photons. An electric DC generator was used to apply the constant electric power to the lamp inside the reactor. During each run the liquid passed through a heat exchanger inside a temperature-controlled bath to maintain the liquid temperature at constant level. Before returning to the photocatalytic reactor the solution passed in a buffer reservoir where 10 mL sample solutions for analytical purpose are collected. This reactor setup was made in the frame of a PhD work by F. Moosavi (Moosavi F., planned on October 2022)

The principal schema of the experimental installation is shown in Figure 44.

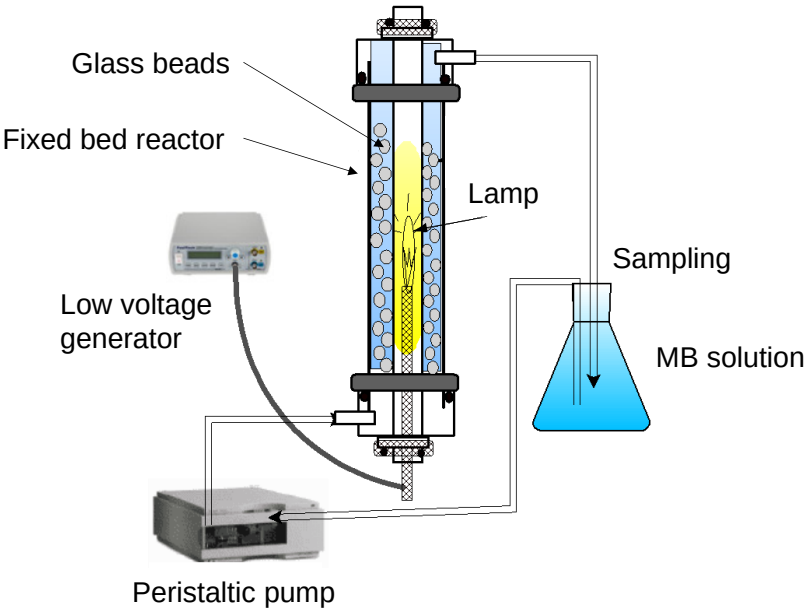

Figure 44 Scheme of photocatalytic reactor (Moosavi F., planned on October 2022).

The coated glass beads (m=90 g, N≈1050 pieces) were freely placed in a gap of 6 mm width between two-cylinder quartz tubes of lengths 395 mm. The inner tube of 34 mm external diameter contained the lamp of 16 mm diameter and 395 mm length, which is equal to that of the surrounding quartz tubes. The reactor body had the following geometry:

- External Diameter of the outside tube: 49.8 mm,
- Internal Diameter of the outside tube: 46.15 mm,
- Length of the Tube: 395 mm,
- External Diameter of the internal tube: 34.10 mm,
- Internal Diameter of the internal tube: 30.43 mm.

5.1.2 Lamps as light sources

The light source lamp is introduced inside the reactor, depending on the photocatalytic test, but throughout the project3 different lamps were used:

- UVA lamp Phillips TL BLB of 8 Watts, emitting at 365 nm with full width at half maximum $\Delta\lambda_{1/2}$=15 nm
- Visible lamp Phillips O5 of 8 W, having a broad-band spectrum with $\lambda \geq 380$ nm
- Visible Lamp OSRAM HLX 64610 BRL of 50 W, having a broad-band spectrum with spectral maximum at ~700 nm

The photocatalytic experiments were organized as following:

1) Solution containing the pollutant was pushed with the peristaltic pump through the main reactor tube containing the photocatalyst in dark (lamp "off") for about 3 hours duration. During this time, equilibrium was established between the adsorbed and free pollutant molecules in the reactive solution.
2) After the equilibrium was attained, the lamp was set "on" and the experiment (without interruption) was continued for 3 hours longer.
3) The pollutant concentration was permanently monitored on the 1st and 2nd periods via sampling of the reactive solution and absorbance measurements using PC-plugged AvaSpec-Mini UV/VIS/NIR Spectrometer.

Since visible lamps could have a non-negligible UVA component in the emission, capable activating anatase TiO_2 photocatalyst, we made an additional verification of the emission spectra shown in Figure 45. Indeed, we observed a considerable intensity in the UVA spectral range between 300 and 400 nm. Because of this, a UV filter with cutoff wavelength of 390 nm, in form of a film was introduced in the inner tube of the reactor containing the lamp. The resulting emission spectrum shown in Figure 45 shows an excellent elimination of the UVA component, with no light of photons energy above that of the anatase TiO_2 band gap: $h\nu < E_g = 3.2$ eV.

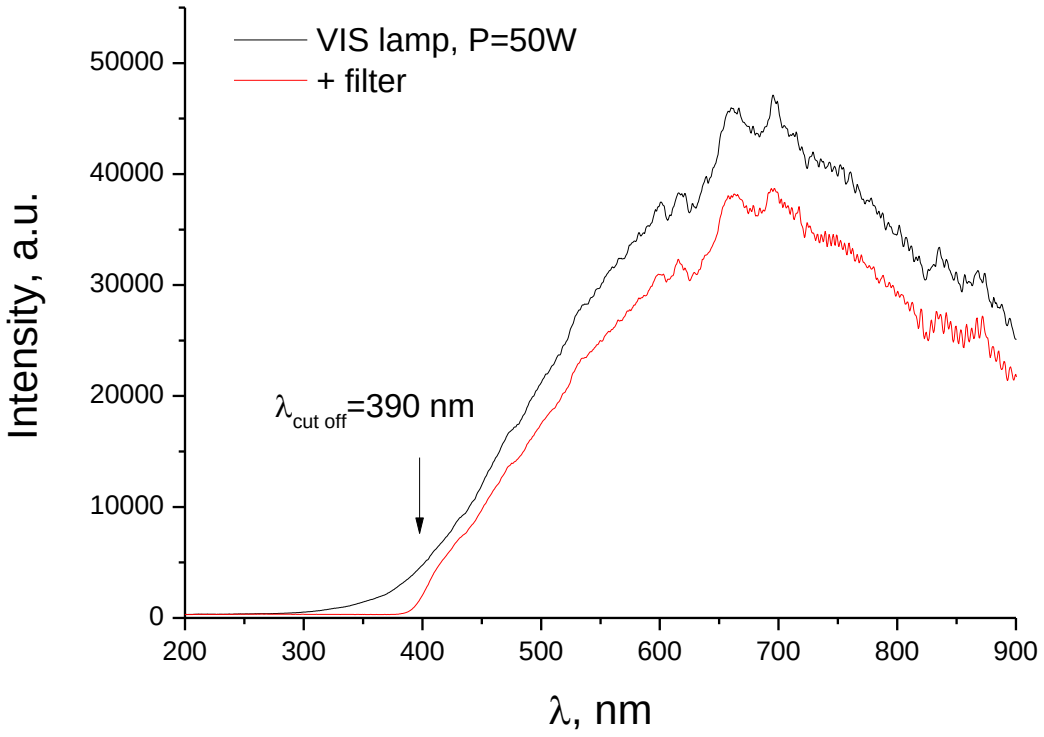

Figure 45 Absorbance of the Light with and without Filter.

5.1.3 Methylene blue preparation

The effectiveness of the prepared materials in photocatalysis was tested on degradation of methylene blue (MB) in an aqueous solution. The MB is a blue substance that can be easy to detect by a naked eye. In these experiments, lots of 1 liter of MB were prepared by using following relations: C=n/V and n=m/M, which conduct to the required mass via the following equation: m = C*V*M, where C is the molar concentration of the MB (10^{-5} mol*l^{-1}), M is the molar mass of MB (319.85 g/mol) and the volume calculated, in this case 1 Liter. The mass of MB of 0.0031985 g was used to prepare 1 liter solution. The calibration curve (Figure 46) of MB solutions was measured at in the maximum of visible absorption at λ=664 nm. An illustrative example of the different MB solutions is in Figure 47.

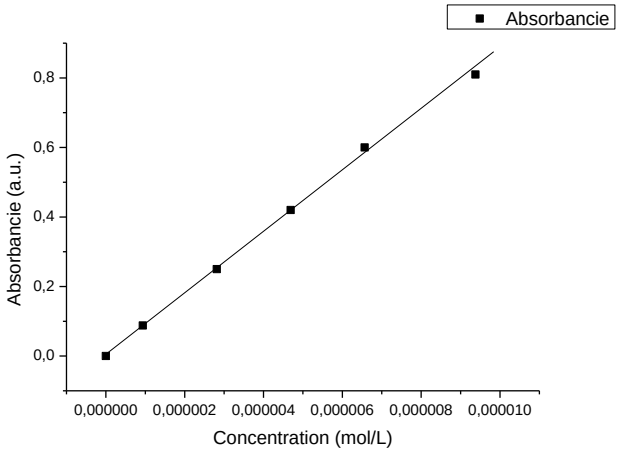

Figure 46 Calibration curve for the BM solution measured at 664 nm.

Figure 47 Solution of MB.

5.1.4 Preparation of the beads

The substrate used for the current experiments was Glass Beads (Supelco Merck) of 4 mm diameter

To have a better quality of beads, they underwent a strict process of cleaning specified below:

- Cleaning of the beads with concentrated sulfuric acid
- Rinsing the beads to remove any trace of sulfuric acid for 24 hours.
- Checking the pH of the beads to be on ± 7

- Drying the beads in the oven at 80°C for 12 hours to remove any trace of humidity

Every photocatalytic experiment was performed with 90 g glass beads coated with V-TiO_2 nanoparticles; the volume of metallic precursor solution is fixed to 100 mL. [Ti^{4+}] is fixed to 0.15 M. The volumes of vanadium precursor and isopropanol are adjusted to reach the following Ti/V molar ratios. The Hydrolysis rate is fixed to 1.5. The activity of V-TiO_2 coating with different vanadium content prepared according to the following procedure:

- The solution of V-TiO_2 was deposited on the already prepared beads inside the Glove Box, during a contact time not exceeding the solution stability (several hours).
- The coated beads were separated from the solution and dried.
- The coated beads were transferred to an oven for heat treatment at 450°C for 4 hours.
- The beads were kept in a closed glass box for a photocatalytic test.

5.2 Photocatalytic activity of V-TiO_2 photocatalyst under UVA light

5.2.1 Adsorption of methylene blue

During the preliminary investigations, we observed that the vessels during MB circulation turn in a blue color indicating that the surfaces were covered with MB molecules. This effectively decreased the local concentration of free MB in the reactive solution and, in counterpart, enriched photocatalyst surface with the pollutant molecules. To separate the role of adsorption from that of photocatalytic reactions, the liquid circulated in the reactor for about 3 hours. The adsorption measurements of the selected samples are shown in Figure 48. Two groups of the curves can be distinguished in these experiments. In fact, the uncoated glass beads at equilibrium adsorbed ~50 mol% of MB, while between 20 and 30 mol% MB were adsorbed by the coated beads depending on the composition of the coated V-TiO_2 nanoparticulate material.

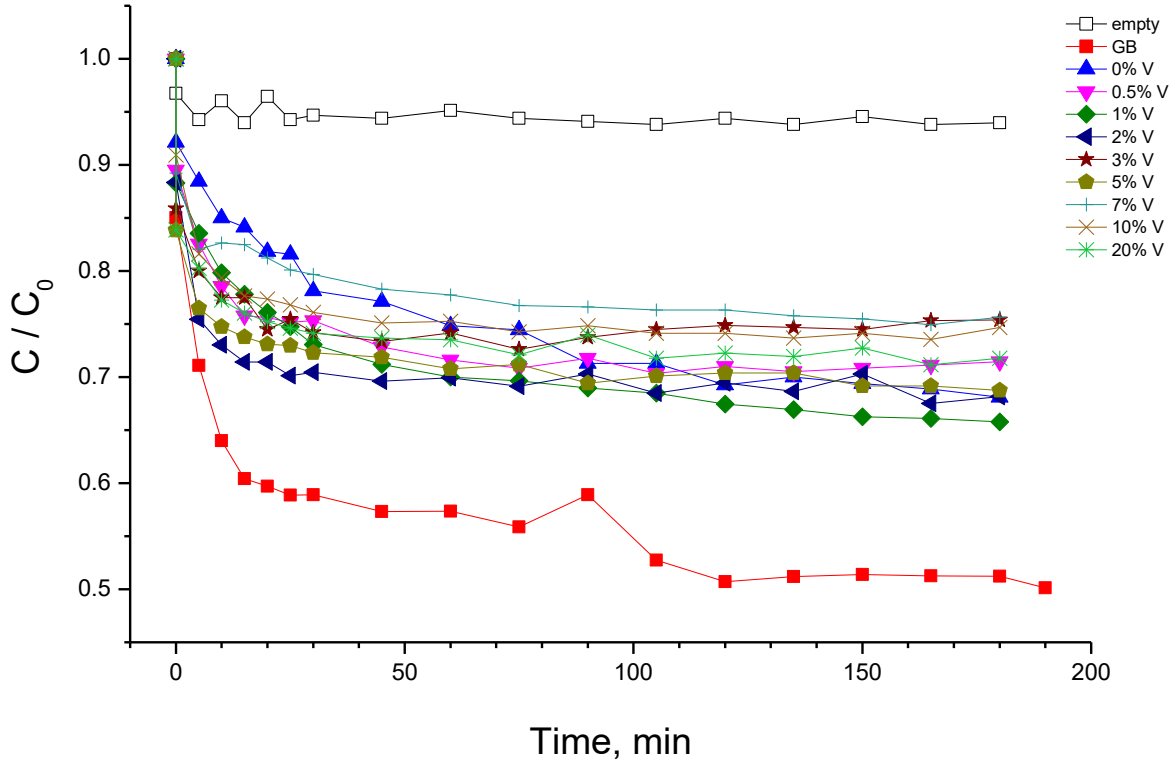

Figure 48 MB adsorption measurements with UV lamp "off" using uncoated and V-TiO_2 coated glass beads (GB). Adsorption curve in empty reactor is also shown. Vanadium content is indicated in mol%. Experimental conditions: No lamp, Initial concentration of MB 10^{-5} mol*l^{-1}, 400 mL.

5.2.2 Photocatalytic activity under UVA light illumination

The adsorption measurements permitted distinguishing free and adsorbed MB exposed to UVA illumination in the photocatalytic tests and, consequently, their respective contributions to the MB photolysis and photocatalytic decomposition. The kinetics of MB decomposition under UVA illumination in the empty reactor and that filled with uncoated and coated glass beads with V-TiO_2 nanoparticles with different vanadium content is presented in Figure 49. One can see from these data that the photolysis of solvated MB molecules (empty reactor) is almost negligible in our experimental conditions. In contrast, adsorbed MB molecules onto uncoated glass beads underwent an appreciable photolytic decomposition. Consequently, we assumed that MB decomposition

kinetics due to photolysis is directly proportional to the adsorbed MB quantity at equilibrium obtained from Figure 48. As a result, we conclude that the photolytic rate in presence of the prepared photocatalysts was about a half of that in presence of uncoated glass beads. We also notice that a significant deactivation of TiO_2 photocatalyst takes place by the MB decomposition (second use).

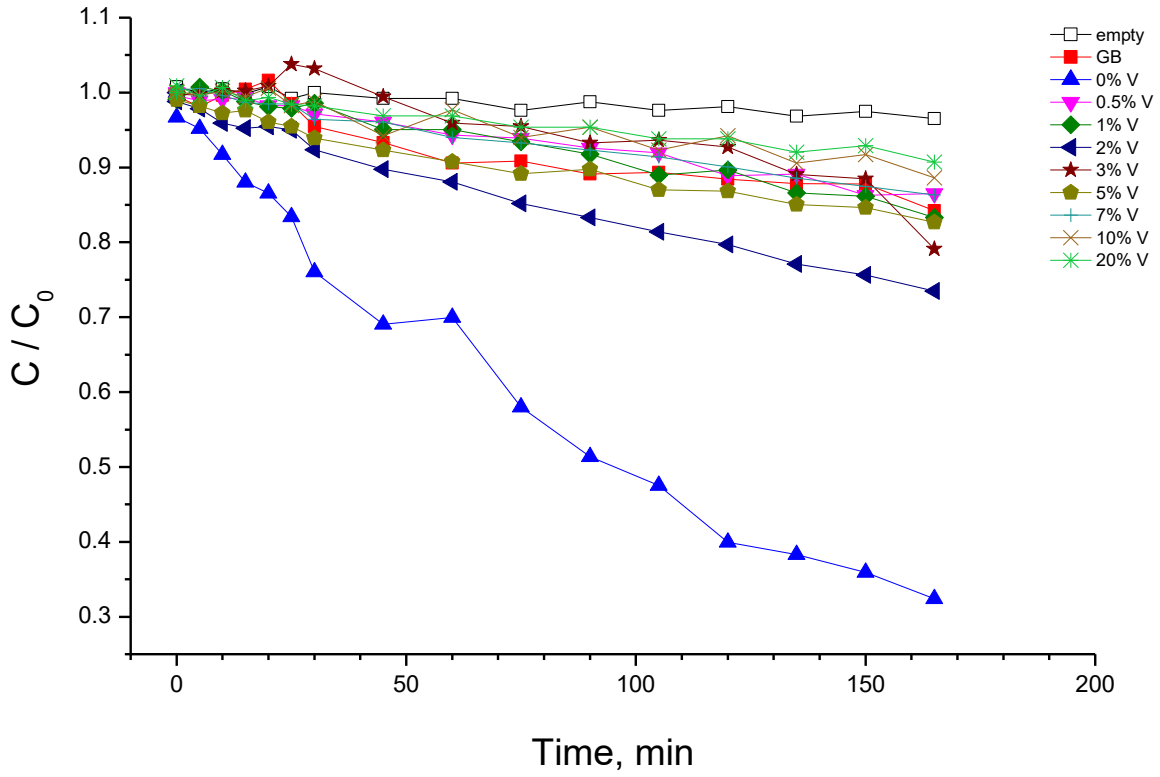

Figure 49 Photocatalytic measurements with UV lamp "on" using V-TiO_2 coated glass beads (GB). Vanadium content (in mol%) is indicated. Experimental conditions: UV Lamp, Initial concentration of MB 10^{-5} mol*l^{-1}, 400 mL

The measured kinetic curves followed the first-order process kinetics, which permits evaluation of the intrinsic material activity (Cheng *et al.*, 2018). As a result, the data were linearly fitted in semi-logarithmic frame and the obtained reaction rate constants k (in min^{-1}) are shown in Figure 50 as a function of vanadium content in the photocatalyst. The results clearly evidenced that the reactivity varied with an increase of V content: the kinetic constant K increased from 0.8 to 4.2 min^{-1} when the

vanadium content increased from 0.5 mol% to 2 mol% and vanished to almost zero at 20 mol% of vanadium.

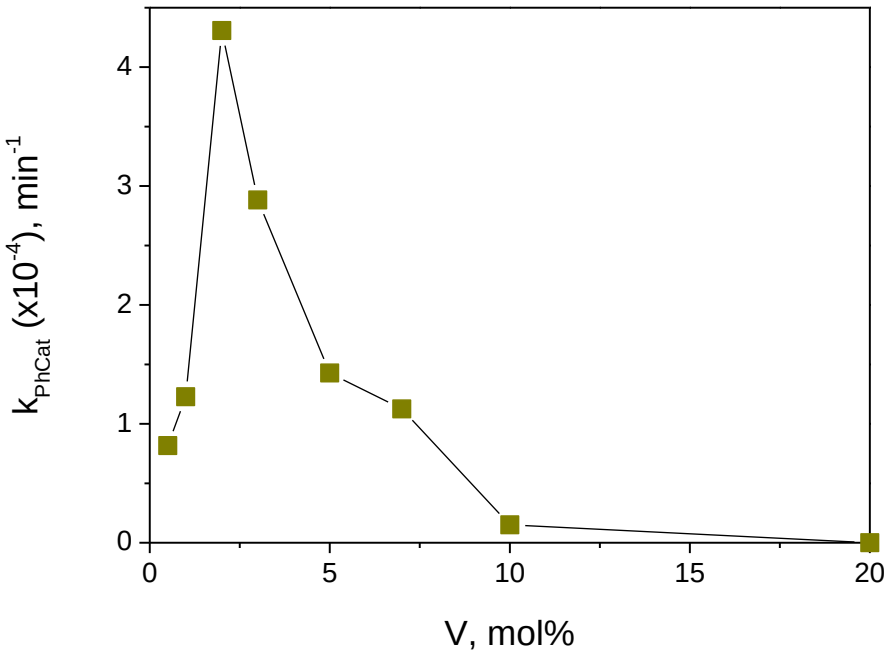

Figure 50. Photocatalytic decomposition rate constant of MB with UV lamp (360 nm) versus vanadium content in V-TiO_2 coated glass beads.

Although the direct comparison with literature data is not possible, (Chang P-Y. *et al.*, 2009) have shown that insertion of vanadium ions decreases photocatalytic activity of TiO_2 nanoparticles under UV light (305 nm) illumination toward MB decomposition. On the other hand, (Zhang Z. *et al.*, 2010) have reported that the maximum rate of the MB decomposition of V-doped TiO_2 nanofibers is attained at 5.0 wt% V under UV light illumination (50 W high-pressure Hg-lamp, $\lambda \geq 330$ nm). Furthermore, maximum activity of 1 mol% V-doped TiO_2 nanoparticles has been reported by (Liu B. *et al.*, 2009) in degradation of methyl orange in aqueous solutions under UVA lamp (365 nm) illumination. This spread of data may be explained by material elemental homogeneity. In fact, (Liu S. *et al.*, 2009) have proposed that the photocatalytic activity under UV illumination (365 nm) of evenly V-doped TiO_2 photocatalysts attains the maximum at low dopant level ~0.002 mol% and decreases

with further increase of the V content; in contrast, the unevenly doped V-TiO_2 photocatalysts possess a higher photocatalytic activity, which can be ascribed to an effective electrostatic-field-driven electron-hole separation. (Chang S. and Liu W., 2011) have rationalized these results by concluding that the bulk doping caused detrimental effects on the UV photocatalytic activity (λ=305 nm, Rhodamine B degradation), since V^{3+}/V^{4+} ions in titania lattice inhibit charges diffusion to the surface through deep trapping; in contrast, the surface impurities facilitate interfacial charge transfer to adsorbates. In particular, the activity of bulk V-doped TiO_2 decreased upon increasing V/Ti ratio up to V/Ti=1.2 %; in contrast, activity of the surface V-doped TiO_2 increased upon increasing the concentration of V ions up to V/Ti=0.3. These results evidence the key role of the preparation method on the V-TiO_2 material activity.

Because of the similar light absorbance of V-TiO_2 coatings (Figure 48, see also discussion of TDA-TGA measurements of V-TiO_2 nanopowders in Chapter 4.2) the specific surface area is not expected to be responsible for the observed effect. The anatase crystalline cell was also preserved at the vanadium content below 20 mol%. We, therefore, relate it to the material morphology and electronic structure. In fact, our particular method of the controlled V-TiO_2 nucleation (Sanchez Mendez M. *et al.*, 2021) suggests the formation of particles enriched with surface vanadium, which according to (Bettinelli M. *et al.*, 2007) promotes the photocatalytic activity because of a modification of the adsorption capacity of the material surface; we notice that a complex interaction between Ti^{3+}/Ti^{4+} and V^{4+}/V^{5+} in mixed metal oxides has been investigated earlier by (Trifiro F., 1998). However, this explanation is not supported by our MB adsorption measurements, which showed a small variation of the adsorption capacity of anatase TiO_2 with vanadium loading, in agreement with earlier results of (Khan H. and and Berk D., 2013), who reported the specific surface area (BET) of V-doped TiO_2 with V/Ti ratio of 1-5 mol% synthesized by hydrothermal method ranged between 140 and 168 m^2/g. We therefore suggest that the reason of the activity modification could be found in the electronic structure of the materials and in the intraband states produced via vanadium insertion into the host anatase matrix. Furthermore, we notice an interesting correlation: the maximum activity

corresponds to the composition, in which, according to our Rietveld analysis, brookite phase appeared and crystalline domains increased. The last may strengthen charge separation efficiency at the anatase-brookite interface, improving the activity.

5.3 Photocatalytic activity of V-TiO_2 photocatalyst under visible light illumination

The V-TiO_2 tested with the UVA light source were also used in complementary photocatalytic experiments with the visible illumination. The experimental procedure is described in Chapter 5.1. After establishment of equilibrium of the MB adsorption/desorption on the photocatalyst (Figure 48), the visible 50-W lamp was switched “on” and sampling was periodically taken on the solution for the evaluation of the MB concentration decrease. The film filter described in the previous section was used in the experiments to avoid material activation with the UVA component. The kinetics of MB decomposition on glass beads coated with V-TiO_2 nanoparticles with different vanadium content are shown in Figure 51.

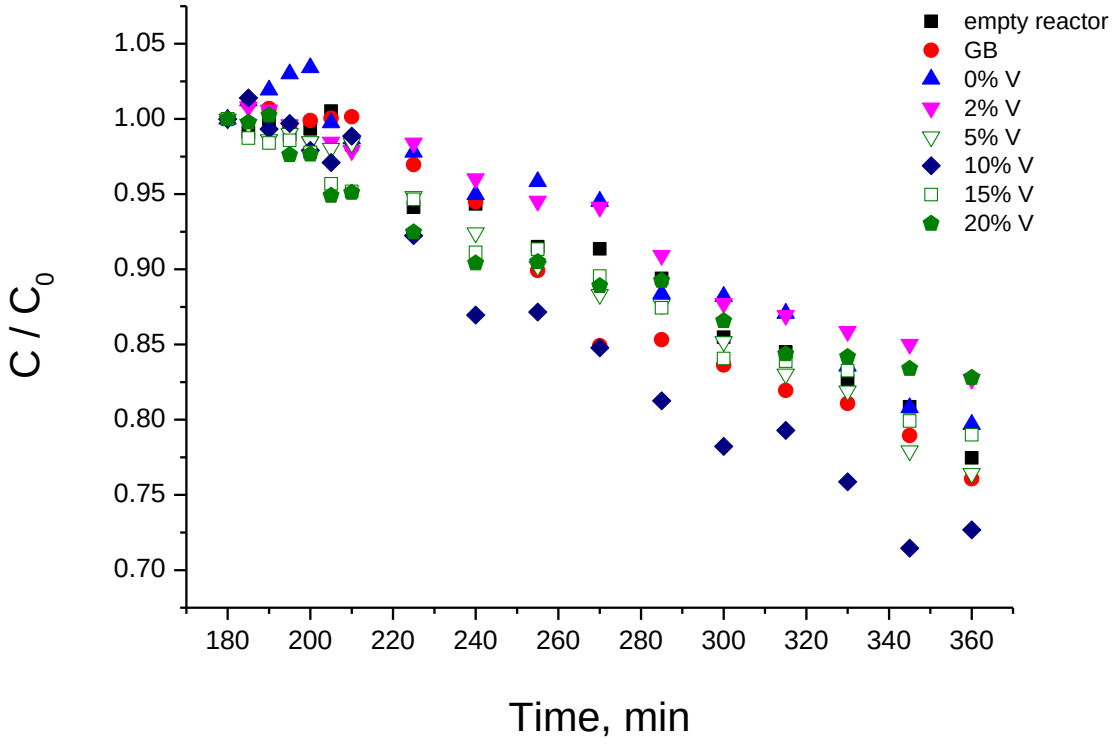

Figure 51 Kinetics of MB photocatalytic decomposition using V-TiO_2 coated glass beads with different vanadium content (in mol%). Experimental conditions: Visible Light Lamp, Initial concentration of MB 10^{-5} mol*l^{-1}, 400 mL.

The experimental data in Figure 51 followed the first-order kinetics and, by analogy with the UVA photocatalytic data (see Chapter 5.2), were linearly fitted in semi-logarithmic frame to obtain the reaction rate constants k (in min^{-1}). These k values are presented in Figure 50 as a function of vanadium content in the photocatalyst.

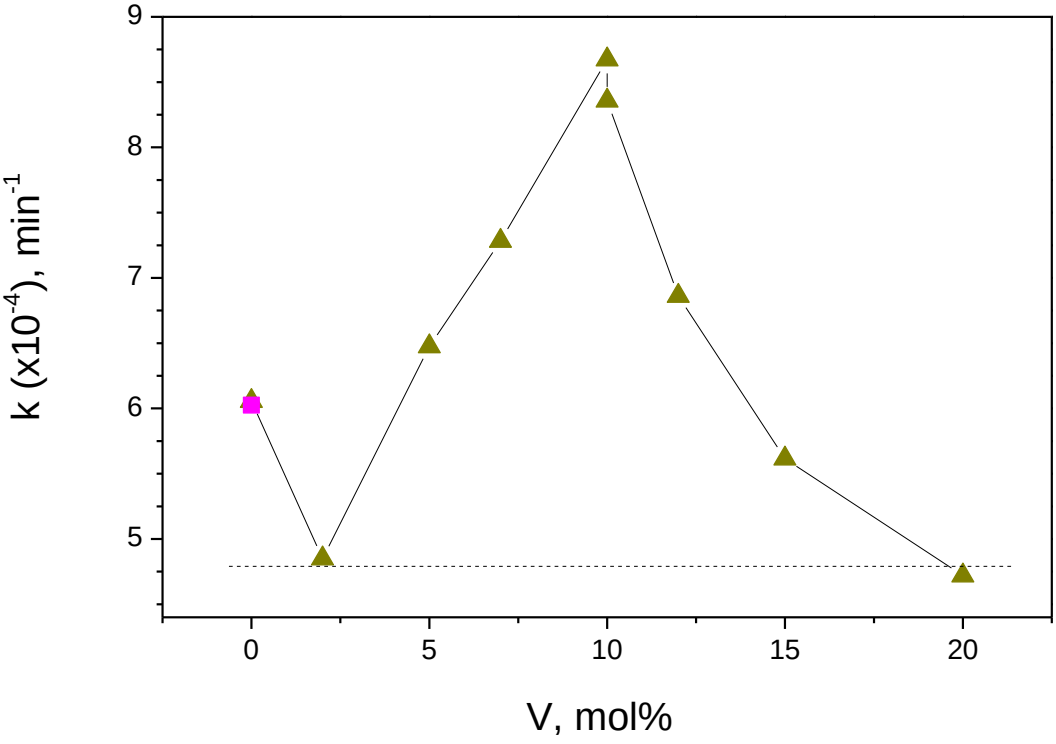

Figure 52 Photocatalytic decomposition rate constant of MB with VIS lamp (λ>390 nm) versus vanadium content in V-TiO_2 coated glass beads. Rate in empty reactor (due to photolysis) is shown by "filled square" symbol.

According to these data, the activity of the V-TiO_2 anatase coatings increased with the increase of vanadium content reaching maximum at 10 mol% V and decreasing afterwards. We notice that the level of k=1.25 min^{-1} in empty reactor belongs to the direct photolysis, which remains the main route of the MB decomposition with pure anatase TiO_2 (0 mol% V) under the visible light illumination. Because of somewhat weaker adsorption capacity of the V-doped coatings, the rate of direct photolysis slightly decreased (k=1.0 min^{-1}) over 2 mol% V doped material. By consequence, the following increase of the activity was purely attributed to photocatalysis. At 20 mol% V doping, the MB decomposition rate decreased to the direct photolysis level confirming evanescent photocatalytic contribution. We conclude therefore that the photocatalytic activity of the V-doped anatase TiO_2 has maximum at 10 mol% V content and disappeared in pure TiO_2 as well in heavily dopped V-TiO_2 material with the vanadium content of 20 mol% and higher (not shown here).

The last might be connected to a non-complete crystallization of the material. To verify this point, the 20 mol% V photocatalysts after heat treatment with higher temperatures of 500 °C and 600 °C were additionally prepared and tested. Figure 53 shows series of the MB decomposition kinetics under visible light illumination (λ > 390 nm) using heat treated V-TiO_2 coatings at different temperatures. The results show no appreciable difference in the kinetics rate constants (correspondent to the slopes of curves): consequently, the MB decomposition was entirely due to photolysis and the 20 mol% V coatings remained inert under the visible light illumination.

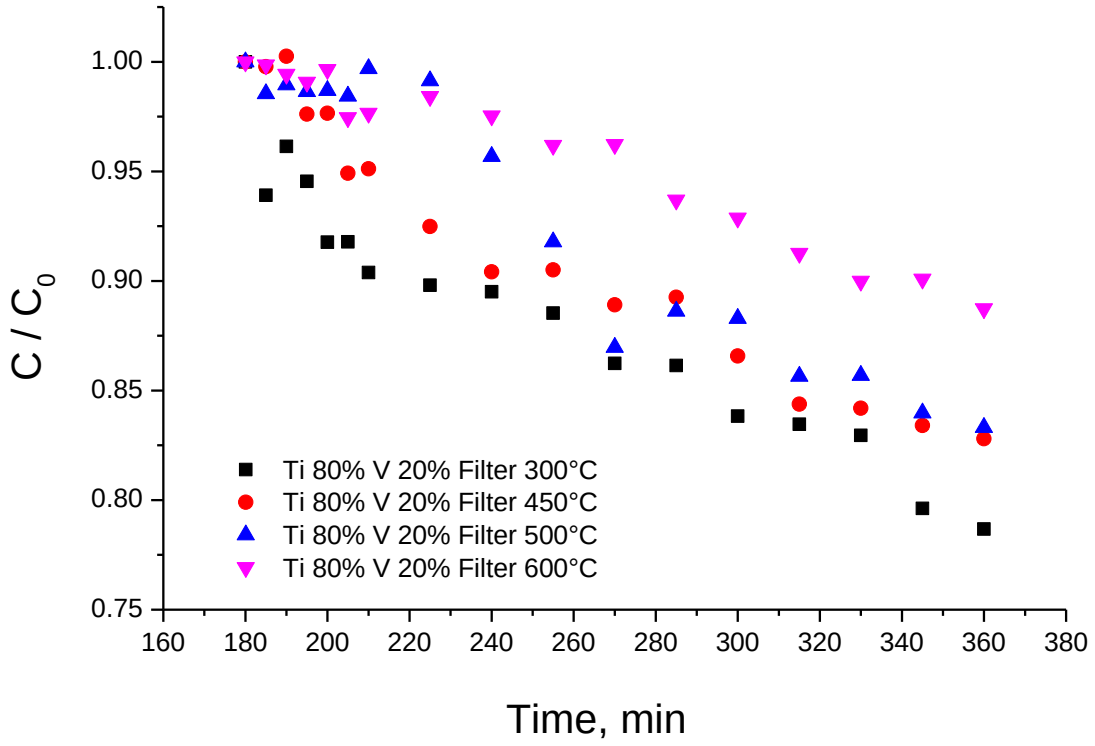

Figure 53 Kinetics of the MB decomposition under visible light illumination () using V-TiO_2 nanocoatings with 20 mol% V heat treated at different temperatures.

To clear up the nature of material activity, we underwent the measurements of photocatalytic kinetics with different intensities of the visible lamp. The resulting dependence of the photocatalytic rate constants in empty reactor (photolysis) and in reactor filled with V-TiO_2 coated glass beads

(photocatalysis) on the visible lamp power is shown in Figure 54 for V-TiO_2 coatings with 10 mol% V content.

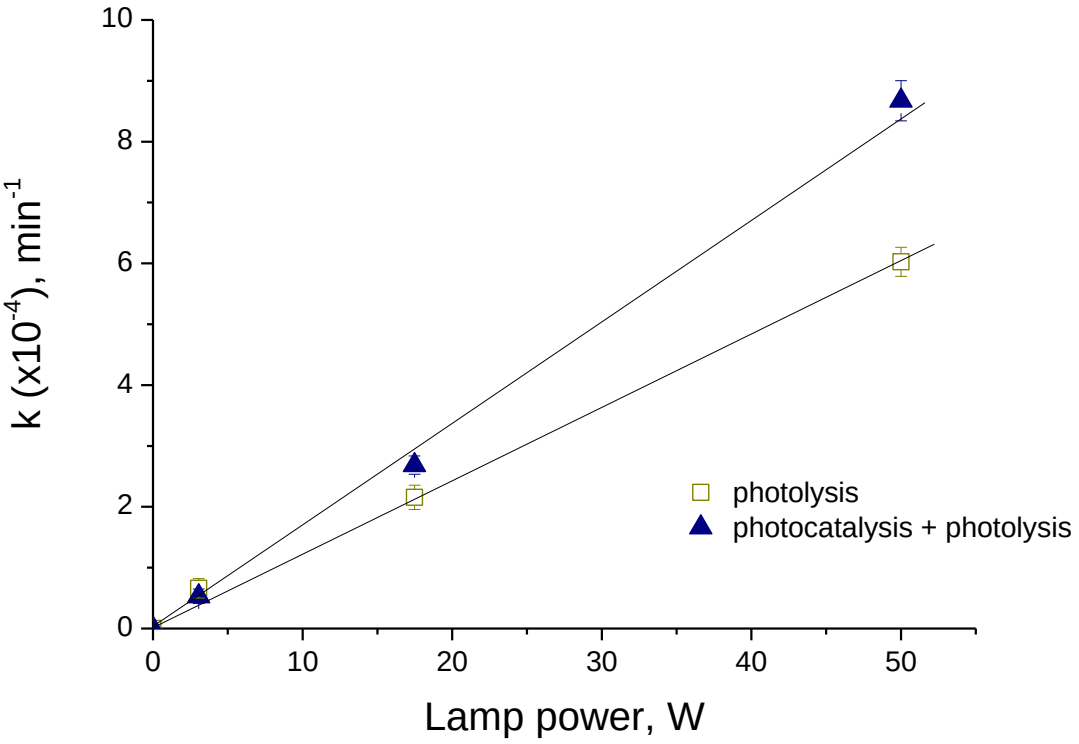

Figure 54 MB degradation rate versus visible lamp power (λ>390 nm).

The analysis of the experimental data showed that photocatalytic rates k_{ph} of MB decomposition have an evident linear component $k_{ph} \propto W$, which confirms that the process is far from saturation phenomena.

The electronic properties of vanadium-doped rutile TiO_2 are investigated theoretically with a Hartree–Fock/DFT hybrid approach by (Islam M. M. *et al.*, 2011). The energetic and electronic properties are converged with dopant concentrations in the range of 0.9 to 3.2%, which is compatible with the experimentally accessible range of the V-TiO_2 compositions. The results of this study confirmed the creation of occupied and unoccupied V^{4+} states in the band gap and V^{5+} unoccupied states at the bottom of the conduction band. These conclusions have been confirmed by

(Khan H. and Berk D., 2013), who showed that V 3d states are introduced below the conduction band minimum suggesting that the combined effect of V^{5+}/V^{4+} centers is helpful for the reduction of recombination rates of photoinduced charge carriers by trapping. Recently, position of the V dopant-induced intra-gap levels has been estimated as 2.2 eV below the conduction band minimum by (Rossi G. *et al.*, 2018), permitted the transfer of electrons into the CB on electronic transitions from intra-gap levels associated with V^{4+} cations, by absorbing 530-nm photons. Furthermore, a precision on the intraband defect states has been given by (Ren F. *et al.*, 2015) suggesting a synergistic effect of V and single-electron-trapped oxygen vacancy (SETOV) $V_o^{\bullet}$ centers. They showed that this deep donor level hybridized by the Ti 3d and O 2p states within the band gap disappeared in V + V_o^{2+}-TiO_2 moving to the top of the valence band, while V_3d at the bottom of the CB also disappeared and new electronic states consisted of Ti_3d, V_3d, and O_2p appeared on the bottom of the CB. All these results confirmed the existence of the impurity/defect states capable of receiving a photoinduced electron enabling the photocatalytic activity of the material.

The previously reported studies have attributed the maximum photocatalytic activity under visible light illumination to the V-TiO_2 materials with the vanadium content about 1-2 mol% (Gu D. E. *et al.*, 2007) (Chang P-Y. *et al.*, 2009) (Liu B. *et al.*, 2009) (Khan M. *et al.*, 2013) (Ren F. *et al.*, 2015), although a significant activity has been extended up to 5 mol% V and dropped only at 10 mol% V (Ren F. *et al.*, 2015). A comparison with our results indicated maximum activity of V-TiO_2 at 10 mol% V (Figure 52), however, is not straightforward. First at all, because a complex interplay between the surface and bulk states (Chang S. and Liu W.., 2011) are responsible for the final response of material and controls the photocatalytic process. In fact, cations occupy almost 50% of surface sites in the elementary V-TiO_2 nuclei (Sanchez Mendez M. *et al.*, 2021), which compose our nanocoatings. In small V-TiO_2 nanoparticles no distinct separation between surface and bulk states could be expected, which both can affect the charge diffusion process, by simultaneously improving (surface sites) and inhibiting (bulk sites) the interfacial charge transfer to adsorbates. However, the variation of the material activity under UVA illumination (Figure 50) could be rationalized by assuming first filling of

bulk states (which initially reduced the activity of V-TiO_2 compared with pure titania), then filling of surface states (which subsequently reproduced an expected activity variation). The visible illumination does not result in any appreciable photocatalytic activity of pure titania: therefore, in contrast to UVA illumination (Figure 50), no initial reduction of the activity with small addition of vanadium can be observed in Figure 51. In the following, the activity increases with an increase of the vanadium content, apparently because the bulk states weakly participate in the excitation process. The reason of that remains unanswered and requires more studies.

Anyway, by comparing in Figure 55 the activity curves after UVA and VIS lamp illuminations, one can suggest the existence of specific active sites X1 and X2 in the respective 2 mol% V and 10 mol% V materials.

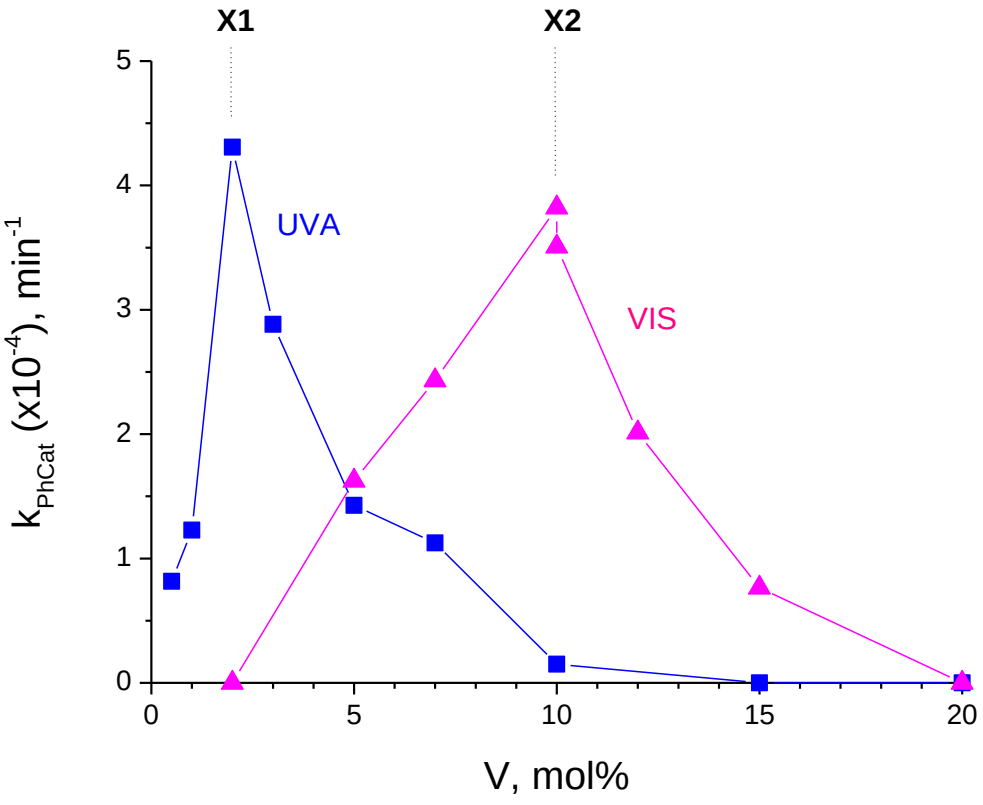

Figure 55 Comparison of the photocatalytic activities towards MB degradation under UVA (λ=365 nm) and VIS (λ>390 nm) lamps illuminations. Participation of active sites X1 and X2 in respective materials can be suggested.

The site X1 can be populated after the photoinduced CB/VB charges relaxation (UVA lamp). In contrast, the direct intragap excitation (VIS lamp) cannot reach these states, which makes the activity of 2 mol% V material low. On the other hand, the direct intragap excitation (VIS lamp) populates active site X2, which population after CB/VB charges relaxation (UVA lamp) is not effective. Since the CB electrons appear in V-TiO_2 materials under both ultraviolet and visible light illuminations (Rossi *et al.*, 2018) the hypothetical states X1 and X2 can be attributed to the hole (h^+) localization at the nanoparticles surface. Their natures remain still unclear.

5.4 Photocatalysis with combined excitation by UVA and visible light sources

The following experiments were undertaken to check if combination of UVA and visible photons could improve the photocatalytic activity of the V-TiO_2 material. In this series, the visible 50-W lamp was placed inside the reactor main tubing (covered or not with the cut-off filter: $\lambda \geq 390$ nm) and external 8-W UVA lamp, as shown in Figure 56.

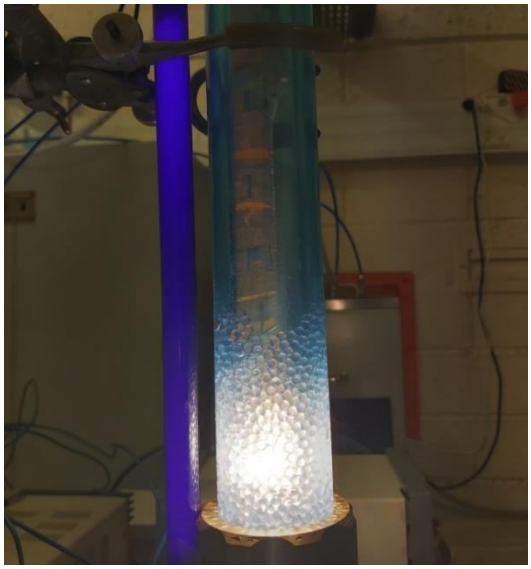

Figure 56 Experimental Setup with LV and UV lamps.

The glass beads coated with V-TiO_2 nanoparticles containing 10 mol% vanadium, which are most efficient under visible light illumination, were used as photocatalyst in these experiments. The kinetics of the MB decomposition in the reactor is shown in Figure 57. The results reveal an unexpected result: presence of UV photons seems to lower the activity of the photocatalysts activated by visible light.

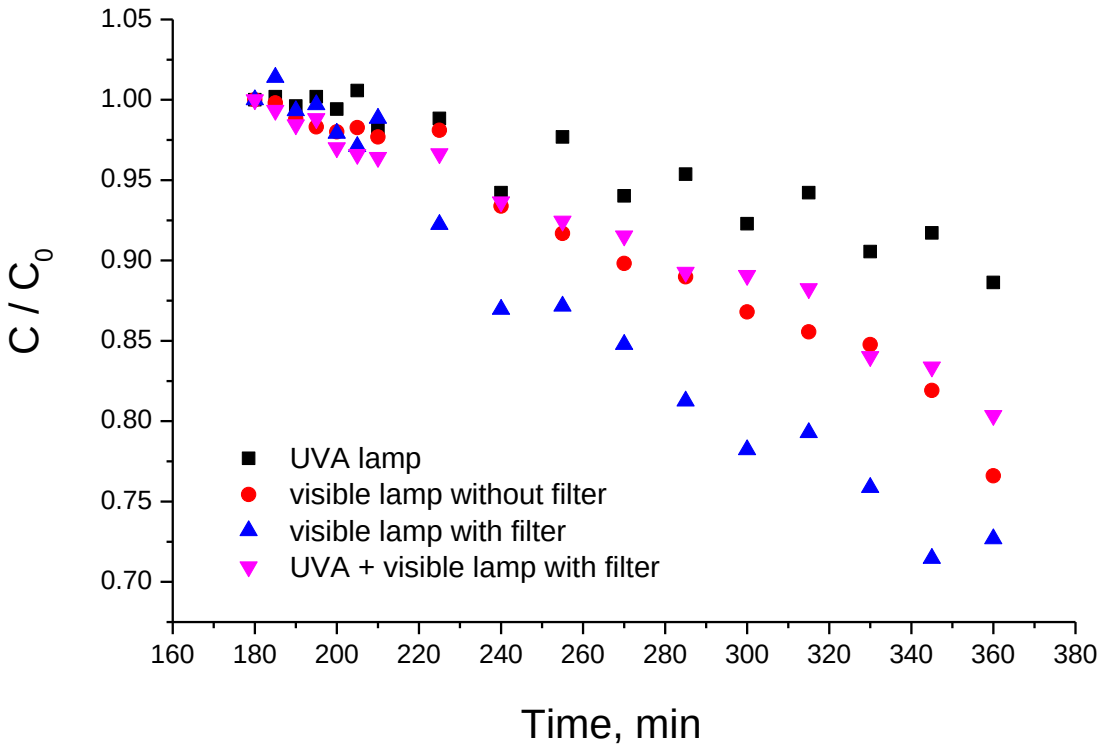

Figure 57 Kinetics of MB decomposition under UVA lamp (365 nm), visible lamp (without filter), visible lamp (with 390-nm filter) and both UVA and visible lamp (with 390-nm filter) illuminations, using V-TiO_2 (10 mol% V) coated glass beads.

The results showed no synergy of the combined illumination and confirmed that (i) UVA light illumination provide the lowest decomposition rate of the 10 mol% V material, which according to Figures 49-50 is mostly related to the MB photolysis, while (ii) visible light illumination provide the highest MB decomposition rate. Unusually, the combined UV and visible lamps illumination resulted in intermediate MB decomposition rates, which may signify partial inhibition of the photocatalytic activity by UV photons in the range of $300 \leq \lambda \leq 390$ nm. This destructive contribution of UV photons requires further understanding.

5.5 Conclusions

In Chapter 5, photocatalytic activities of nanocoatings made of size-selective V-TiO_2 with different vanadium content and heat-treated at 450 °C (for 4 hours) were investigated. The photocatalytic experiments were conducted under illuminations with UVA (λ=365 nm) and visible (λ>390 nm) lamps. The MB kinetics were continuously monitored (i) in dark for 3 hours until attaining the equilibrium of the adsorption-desorption process on the catalyst surface and (ii) under lamp illumination during 3 hours for an observation of the photolytic and photocatalytic processes. The photolytic and photocatalytic processes were distinguished. We showed that the activity of 20 mol% V coatings vanished and could not be improved via heat treatment at higher temperatures of heat treatment up to 600 °C, which improved material crystallinity.

The best performance under UVA and Visible light illuminations showed V-TiO_2 photocatalysts with respectively 2 mol% and 10 mol% vanadium. In contrast, combined illumination of the 10 mol% V photocatalyst with the visible and UV photons ($300 \leq \lambda \leq 390$ nm) resulted in the activity inhibition, which reason requires an understanding. We tentatively assigned this finding to the population of specific active sites X1 and X2 in the respective 2 mol% V and 10 mol% V materials. The site X1 can be populated after the photoinduced CB/VB charges relaxation (UVA lamp) and cannot be reached via the direct intragap excitation (VIS lamp). On the other hand, the state X2 can be accessed via direct intragap excitation (VIS lamp), while its population via the CB/VB charges relaxation (UVA lamp) not effective.

Chapter VI General Conclusions and Perspectives

General Conclusions

In this work, the mixed vanadium-titanium oxo-alkoxy (VTOA) nanoparticles were synthesized via sol-gel method in a rapid laboratory-scale micromixing reactor, permitting point-like reaction conditions and narrowest particle size distribution. The particles nucleation and growth kinetics were monitored in situ via home-made monomode optical fibre probe, using static and dynamic light scattering methods. The vanadium addition worsened the coherent component of the scattered light prohibiting the particle size analysis at high vanadium content >20 mol%. However, at relatively low vanadium content of ≤10 mol% the analysis of experimental data permitted to conclude about nucleation of the mixed VTOA particles of 2.1 nm radius. We showed that titanium oxo-alkoxy (TOA) species appear first and serve to be centers of attraction for hydrolyzed vanadium oxo-alkoxy (VOA) species at the nucleation stage. In contrast, at high vanadium content VOA species percolate by imprisoning sub-nucleus TOA species prohibiting the nanoparticles appearance. This is connected to stronger hydrolysis and weaker condensation abilities of VOA species compared to TOA. The experimental VTOA kinetics at the induction stage agreed with the Rivallin's model (Rivallin M. *et al.*, 2004) (Rivallin M. *et al.*, 2005) and extended it to the case of non-conservation of the nucleus number density (at fixed total mass of the nuclei). The analysis of the experimental data validated an increase of the VTOA nucleus size with an increase of hydrolysis ratio (weak) and vanadium content (strong); this corresponds to a decrease of the nucleus number density in the reactive solution resulting in the unusual induction time lengthening. The experimental data support the new paradigm of the sol-gel process proposed by (Kessler V.G. *et al.*, 2009), which assumes a profound restructuring of oxometallic species during their association at the nucleation stage. This restructuring, quite appreciable in heterocationic species M1M2OA (M1≠M2=Zr, Ti, V, etc.), can be followed at the particle's nucleation stage as a function of the elemental composition.

Based on the results of the VTOA nanoparticles stability, the structure of V-TiO_2 nanopowders with different vanadium content varied from 0 to 20 mol% was studied after heat treatment in the range of temperatures 300-1000 °C for 4 hours. The TGA-TDA measurements showed a complex behavior

of the material resulting in a significant dependence of the anatase phase transition temperature with the vanadium content, which support perfect insertion of V atoms into host TiO_2 matrix. We showed that the heat treatment at 450 °C of VTOA nanoparticles with the vanadium content below 20 mol% resulted in the formation of anatase crystalline structure, which is identical to that of pure TiO_2; the Rietveld analysis of XRD patterns evidenced no significant deviation of the anatase structure parameters.

An interesting trend can be also observed in the anatase crystalline size evolution with vanadium content within the solubility range: the size sharply increased at 2-3 mol% V, where brookite phase appeared, and remained twice smaller at the higher and lower vanadium contents. Furthermore, for 20 mol% V, which corresponds to the TiO_2/V_2O_5 phase segregation phenomenon, the particles coarsen to attain the size of ~18 nm. Concerning the α-V_2O_5 particles size, it appears to be far bigger than that of TiO_2, which supports our previous conclusions about the precursor VTOA species nucleation in the sol-gel process (see Chapter 3).

An increase of the heat treatment temperature showed a progressive transformation of anatase to rutile structure, as confirmed by XRD and Raman measurements. In contrast, new peaks (XRD) and bands (Raman) appeared at the intermediate temperatures between those characteristic of anatase and rutile phases crystallization: $T_c = 600 \pm 100$ °C (20 mol% V). These peaks/band may belong to the orthorhombic α-V_2O_5 phase, which would indicate the material segregation at intermediate heat treatment temperatures; in contrast, vanadium dissolution in anatase and rutile titania takes place at respectively lower and higher temperatures. Alternatively, these peaks may be due to a metastable $V_xTi_yO_z$ solid, which decays after its formation at high temperatures [If true, the preparation method specific to the nanoscale and elemental homogeneity (due to the micromixing conditions) could be of key importance for the novel materials realization.]

Following the first stage of the size selected VTOA nanoparticles mass fabrication and structural characterization after the heat treatment, we have prepared photocatalytic nanocoatings with the vanadium content $0 \leq V / (V+Ti) \leq 0.2$ by the VTOA chemical colloid deposition on glass beads with

the subsequent heat treatment at 450 °C for 4 hours. The photocatalytic activity of the prepared coatings was investigated under illuminations with UVA (λ=365 nm, 8 W) and visible (λ>390 nm, 50 W) lamps. The MB kinetics was continuously monitored (i) in dark for 3 hours until attaining the equilibrium of the MB adsorption-desorption process on the catalyst surface and (ii) under lamp illumination during 3 hours for quantification of the photolytic and photocatalytic reaction kinetics. The photolytic and photocatalytic processes were distinguished. We showed that the activity of 20 mol% V coatings vanished and could not be enhanced via heat treatment at higher temperatures up to 600 °C, which might improve material crystallinity. The best performance under UVA and Visible light illuminations showed V-TiO_2 photocatalysts with respectively 2 mol% and 10 mol% vanadium. In contrast, the combined illumination of the 10 mol% V photocatalyst with the visible and UV photons ($300 \leq \lambda \leq 390$ nm) resulted in the activity inhibition. We tentatively assigned this finding to the population of specific active sites X1 and X2 in the respective 2 mol% V and 10 mol% V materials. The site X1 can be populated after the photoinduced CB/VB charges relaxation (UVA lamp) and cannot be reached via the direct intragap excitation (VIS lamp). On the other hand, the state X2 can be accessed via direct intragap excitation (VIS lamp), while its population via the CB/VB charges relaxation (UVA lamp) not effective.

Perspectives

The applied method of the material preparation can be extended to other mixed oxide nanostructured solids. The actual maturity of the mass-fabrication method of size-selected nanoparticles with the controlled composition in the developed laboratory chemical reactor can permit considering its scale-up and technology transfer for large-scale applications.

The principal issue of the V-Ti-O phase stability at ambient Pressure-Temperature conditions (Yang Y. *et al.*, 2017) could be concerned by the proposed method of the material preparation. In fact, perfect homogeneity of the material composition at nanoscale (related to the nucleus size of R~2 nm) and size-specific material properties may lead to the unusual phase's stabilization. The unassigned XRD

peaks and Raman bands, observed in this study at the intermediate heat-treatment temperatures between those characteristics of anatase and rutile phases crystallization: T_c = 600 ± 100 °C, may belong to a metastable phase of $V_xTi_yO_z$ solid decaying after its formation at high temperatures. More work is required to identify this phase and relate it to a specific size of nanoscale solids and elemental composition during the nucleation process.

The photocatalytic decomposition of MB in aqueous solutions can involve specific surface states, noticed in this work as X1 and X2, which can be populated respectively via CB/VB charges relaxation (UVA lamp) and via intraband photon absorption (VIS lamp). Both these states (and population channels) are connected to the vanadium insertion into anatase TiO_2 lattice. Their nature and population mechanism could be of considerable interest in the environmental photocatalysis. The related studies could be pursued in a future, both experimentally and theoretically, to understand and, eventually, make it selective.

The observed photocatalytic activity inhibition under the combined illumination of the 10 mol% V photocatalyst with the visible and UV photons ($300 \leq \lambda \leq 390$ nm) also requires more verifications and understanding.

Chapter VII Publications and Conferences

Publications and conferences:

Publications:

1.- **M. Sanchez Mendez**, K. Cheng, K. Chhor, M. Traore, M. Ben Amar, A. Kanaev. "Novel Synthesis of Mixed Oxide Nanoparticles for Photocatalysis", Chem. Eng. Transactions, Chem. Eng. Trans. 74 (2019) 433-438.

2.- **M. Sanchez Mendez**, Z. Jia, M. Traore, M. Ben Amar, M. Nikravech, A. Kanaev. "Nucleation and growth of mixed vanadium-titanium oxo-alkoxy nanoparticles in sol-gel synthesis". Colloids and Surfaces A: Physicochemical and Engineering Aspects, 610 (2021) 125636.

3.- A. V. Svetlakova, **M. Sanchez Mendez**, E. S. Tuchina, A. N. Khodan, M. Traore, R. Azouani, A. Kanaev, V. V. Tuchin, "Investigation of photocatalytic antimicrobial activity of TiO_2-Al_2O_3 nanocomposites under LED illuminations at 405 nm against staphylococcus aureus", Opt. Spectroscopy 129 (2021) 736-740.

4.- **M. Sanchez Mendez**, A. Lemarchand, M. Traore, C. Perruchot, M. Nikravech, A. Kanaev, "Preparation and photocalytic activity of coatings based on size-selective V-TiO_2 nanoparticles", Chem. Eng. Trans. 84 (2021) 19-24.

5.- **M. Sanchez Mendez**, A. Lemarchand, M. Traore, C. Perruchot, M. Nikravech, M. Ben Amar, A. Kanaev, "Photocatalytic activity of nanocoatings based on mixed oxide V-TiO_2 nanoparticles with controlled composition and size", (2021) in preparation for submission.

Conferences:

1.- **M. Sánchez Méndez**, Khley Cheng, Khay Chhor, Mamadou Traore, Mounir Ben Amar, Andrei Kanaev, Novel Synthesis of Mixed Oxide Nanoparticles for Photocatalysis. ICheap 14, The 14th International Congress on Chemical and Process Engineering, Bologna, Italy. 26-29 May 2019.

2.- **M. Sánchez Méndez**, A. Lemarchand, M. Traore, C. Perruchot, M. Nikravech, A. Kanaev. "Preparation and Photocatalytic Activity of Coatings based on Size-selective V-TiO_2 Nanoparticles". Nano Technology Based Innovative Applications for the Environment, Salerno, Italy, March 28-30, 2021.

Chapter VIII References

References

1. **Al-Mamun M.R. Kader S., Islam M.S., Khan M.Z.H.** Photocatalytic activity improvement and application [Journal] // J. Environ. Chem. Eng.. - 2019. - 5 : Vol. 7. - p. 103248.

2. **Andersson G.** Studies on Vanadium Oxides [Journal] // Acta Chem. Scand. - 1954. - Vol. 8. - p. 1599.

3. **Andersson G.** Studies on Vanadium Oxides [Journal] // Acta Chem. Scand. - 1956. - Vol. 10. - p. 623.

4. **Artelt C. Schmid H.-J., Peukert W.** Modelling titania formation at typical industrial process conditions: effect of surface shielding and surface energy on relevant growth mechanisms [Journal] // Chemical Engineering Science. - 2006. - 1 : Vol. 61. - pp. 18-32.

5. **Azouani R. Michau A., Hassouni K., Chhor K., Bocquet J.-F., Vignes J.-L., Kanaev A.** Elaboration of pure and doped TiO_2 nanoparticles in sol–gel reactor with turbulent micromixing: Application to nanocoatings and photocatalysis [Journal] // Chemical Engineering Research and Design. - 2010. - 9 : Vol. 88. - pp. 1123-1130.

6. **Azouani R. Soloviev A., Benmami M., Chhor K., Bocquet J.-F., Kanaev A.** Stability and Growth of Titanium-oxo-alkoxy TixOy(OiPr)z Clusters [Journal] // J. Phys. Chem. C. - 2007. - 44 : Vol. 111. - pp. 16243-16248.

7. **Azouani R. Tieng S., Chhor K., Bocquet J.-F., Eloy P., Gaigneaux E. M., Klementiev K., Kanaev A. V.** TiO_2 doping by hydroxyurea at the nucleation stage: towards new photocatalyst in the visible spectral range [Journal]. - [s.l.] : Phys. Chem. Chem. Phys., 2010. - 113 : Vol. 12. - pp. 11325-11334.

8. **Azouani R. Tieng S., Michau A. , Hassouni K., Chhor K., Bocquet J.-F., Vignes J.-L., Kanaev A.** Elaboration of Doped and composite nano-TiO_2 [Journal] // Chem. Eng. Trans.. - 2009. - Vol. 17. - pp. 981-986.

9. **Balachandran U. Eror N. G.** Raman spectra of titanium dioxide [Journal] // J. Solid State Chem.. - 1982. - Vol. 42. - pp. 276-282.

10. **Bałdyga J. Pohorecki R.** Turbulent micromixing in chemical reactors — a review [Journal] // The Chemical Engineering Journal and the Biochemical Engineering Journal. - 1995. - 2 : Vol. 58. - pp. 183-195.

11. **Berne B. J. Pecora R.** Dynamic Light Scattering with Applications to Chemistry, Biology, and Physics [Journal] // J. Chem. Educ.. - 1977. - 10 : Vol. 54. - p. A430.

12. **Bettinelli M. Dallacasa V., Falcomer D., Fornasiero P., Gombac V., Montini T., Romano L., Speghini A.** Photocatalytic activity of TiO_2 doped with boron and vanadium [Journal] // J. Hazard. Mater. - 2007. - 146 : Vol. 3. - pp. 529-534.

13. **Boukhalfa S. Evanoffa K., Yushin G.** Atomic layer deposition of vanadium oxide on carbon nanotubes for high-power supercapacitor electrodes [Journal] // Energy Environ. Sci.. - 2012. - Vol. 5. - pp. 6872-6879.

14. **Brinker C. J. Scherer G. W.** Sol-Gel Science: The Physics and Chemistry of Sol-Gel Processing [Book]. - New-York : Academic Press, 1990.

15. **Cao Z. Li S., Xie W., Du G., Qiao Z.** Critical evaluation and thermodynamic optimization of the V–O system [Journal] // CALPHAD: Comput. Coupling Phase Diagrams. - 2015. - Vol. 51. - p. 241.

16. **Chan Y.-L. Pung S.-Y., Sreekantan S.** Synthesis of V_2O_5 Nanoflakes on PET Fiber as Visible-Light-Driven Photocatalysts for Degradation of RhB Dye [Journal] // Journal of Catalysts. - 2014. - Vol. 2014. - pp. 1-7.

17. **Chang P-Y. Huang C-H., Doong R-A.** Characterization and photocatalytic activity of vanadium doped titanium dioxide nanocatalysts. [Journal] // Water Sci. Technol.. - 2009. - Vol. 59. - pp. 523-530.

18. **Chang S. Liu W.** Surface doping is more beneficial than bulk doping to the photocatalytic activity of vanadium-doped TiO_2 [Journal] // Applied Catalysis B.. - 2011. - 3-4 : Vol. 101. - pp. 333-342.

19. **Chappell J. S. Procopio L. J., Birchall J. D.** Observations on modifying particle formation in the hydrolysis of titanium (IV) tetra-ethoxide [Journal] // Journal of Materials Science Letters. - 1990. - Vol. 9. - pp. 1329-1331.

20. **Chattaraj P.K. Guptaa K., Roya D.R., Subramanianb V.** Are strong Brønsted acids necessarily strong Lewis acids? [Journal] // Journal of Molecular Structure: THEOCHEM. - 2007. - 1-3 : Vol. 812. - pp. 12-24.

21. **ChemTube3D** ChemTube3D [Online]. - 2008-2021. - https://www.chemtube3d.com/ss-v2o5/.

22. **Chen J. Zhenga C., Chen G. A.** Interaction of macro- and micromixing on particle size distribution in reactive precipitation [Journal] // Chemical Engineering Science. - 1996. - 10 : Vol. 51. - pp. 1957-1966.

23. **Chen X. Liu L., Yu P. Y., Mao S. S.** Increasing Solar Absorption for Photocatalysis with Black Hydrogenated Titanium [Journal] // Science. - 2011. - 6018 : Vol. 331. - pp. 746-750.

24. **Cheng K. Chhor K., Brinza O., Vrel D., Kanaev A.** From nanoparticles to bulk crystalline solid: Nucleation, growth kinetics and crystallisation of mixed oxide $ZrxTi_1$-xO_2 nanoparticles [Journal] // Cryst. Eng. Comm.. - 2017. - Vol. 19. - pp. 3955-3965.

25. **Cheng K. Chhor K., Kanaev A.** Photocatalytic nanoparticulate $ZrxTi_1$-xO_2 coatings with controlled homogeneity of elemental composition [Journal] // Chem. Select. - 2018. - Vol. 3. - pp. 11118-11126.

26. **Cheng K. Chhor K., Kanaev A.** Solvent effect on nucleation-growth of titanium- oxo-alkoxy nanoparticles [Journal] // Chem. Phys. Lett. - 2017. - 672. - pp. 119-123.

27. **Cheng K.** Thesis "Elaboration of mixed metal oxide $ZrxTi_1$-xO_2 nano-photocatalysts" [Book]. - 2018.

28. **Chernova N. A. Roppolo M., Dillon A. C., Stanley Whittingham M.** Layered vanadium and molybdenum oxides: batteries and electrochromics [Journal] // J. Mater. Chem. - 2009. - Vol. 19. - pp. 2526-2552.

29. **Constantinides G.** Nanoscience and nanoengineering of cement-based materials [Journal] // Nanotechnol. Eco-Efficient Constr. - 2013. - pp. 9-37a.

30. **CrystallographyOpenDatabase** Crystallography Open Database [Online] // Crystallography Open Database. - 2010. - http://qiserver.ugr.es/cod/index.php.

31. **Dispersions Avantama Ltd - Nanoparticle** Azonano.com [Online]. - AzoNetwork Site, 200-2021. - 2021. - https://www.azonano.com/article.aspx?ArticleID=3364.

32. **Einstein A.** On the Movement of Small Particles Suspended in a Stationary Liquid Demanded by the Molecular-Kinetic Theory of Heat [Online]. - 1905. - http://users.physik.fu-berlin.de/~kleinert/files/eins_brownian.pdf.

33. **Enjalbert R. Galy J.** A refinement of the structure of V_2O_5 [Journal] // Acta Crystallogr.. - 1986. - Vol. 42. - pp. 1467-1469.

34. **Fiermans L. Clauws P., Lambrecht W., Vandenbroucke L., Vennik J.** Single crystal V_2O_5 and lower oxides. A survey of their electronic, optical, structural, and surface properties [Journal] // Physica Status Solidi (a). - 1980. - 2 : Vol. 59. - pp. 485-504.

35. **Fox M. A. Dulay M. T.** Heterogeneous photocatalysis [Journal] // Chemical Reviews. - 1993. - 1 : Vol. 93. - pp. 341-357.

36. **Fujishima A. Hashimoto K., Watanabe T.** TiO_2 photocatalysis: Fundamentals and applications [Book]. - Tokyo : BKC Inc., 1999.

37. **Glauber R. J.** Coherent and Incoherent States of the Radiation Field [Journal] // Phys. Rev. - 1963. - Vol. 131. - p. 2766.

38. **Gradl J. Schwarzer H.-C., Schwertfirm F., Manhart M., Peukert W.** Precipitation of nanoparticles in a T-mixer: Coupling the particle population dynamics with hydrodynamics through direct numerical simulation [Journal] // Chemical Engineering and Processing: Process Intensification. - 2006. - 10 : Vol. 45. - pp. 908-916.

39. **Gu D. E. Yang B. C., Hu Y. D.** A Novel method for preparing V-doped titanium dioxide thin film photocatalysts with high photocatalytic activity under visible light irradiation [Journal] // Catal. Lett.. - 2007. - Vol. 118. - pp. 254-259.

40. **Guo Y. Clark S. J., Robertson J.** Calculation of metallic and insulating phases of V_2O_3 by hybrid density functionals [Journal] // J. Chem. Phys.. - 2014. - Vol. 140. - p. 054702.

41. **Hashimoto K. Irie H., Fujishima A.** TiO_2 photocatalysis: A historical overview and future prospects [Journal] // Jap. J. Appl. Phys.. - 2005. - Vol. 44. - pp. 8269-8285.

42. **Hiraga K. Hirabayashi M.** Crystal Structure and Phase Transformation of the Vanadium-Oxygen System near VO [Journal] // Trans. Jpn. Inst. Met. - 1975. - Vol. 16. - p. 431.

43. **Intelligence HTF Market** Global Nanotechnology Market (by Component and Applications), Funding & Investment, Patent Analysis and 27 Companies Profile & Recent Developments - Forecast to 2024 [Book]. - United States : HTF Market Intelligence Consulting Private Limited, April 2018.

44. **Islam M. M. Bredow T., Gerson A.** Electronic properties of vanadium-doped TiO_2 [Journal] // ChemPhysChem. - 2011. - Vol. 17. - pp. 3467-3473.

45. **Jadhav S.D. Jadhav M.S., Jawale R.W.** Study of Chloride and Nitrate Concentration of Mula Mutha River in Pune City (Maharashtra) [Journal] // Int. J. Chem. and Life Sciences. - 2013. - Vol. 2. - pp. 1140-1142.

46. **Jianhua L. Rong Y., Songmei L.** Preparation and characterization of the TiO_2-V_2O_5 photocatalyst with visible-light activity [Journal] // Rare Metals. - 2006. - 6 : Vol. 25. - pp. 636-642.

47. **Jinfeng Z. Peng Z., Jianjun L., Jiaguo Y.** New understanding of the diference of photocatalytic activity among anatase, rutile and brookite TiO_2 [Journal] // Physical Chemistry Chemical Physics. - 2014. - 38 : Vol. 16. - pp. 20382-20386.

48. **Jouanny I. Labdi S., Aubert P., Buscema C., Maciejak O., Berger M.-H., Guipont V., Jeandin M.** Structural and mechanical properties of titanium oxide thin films for biomedical application [Journal] // Thin Solid Films. - 2010. - 12 : Vol. 518. - pp. 3212-3217.

49. **Kahattha C. Wongpisutpaisan N., Vittayakorn N., Pecharapa W.** Physical properties of V-doped TiO_2 nanoparticles synthesized by sonochemical-assisted process [Journal] // Ceramics International. - 2013. - Vol. 39. - pp. S389-S393.

50. **Kakihana M.** Invited review “sol-gel” preparation of high temperature superconducting oxides." [Journal] // Journal of Sol-Gel Science and Technology. - 1996. - Vol. 6(1). - pp. 7-55.

51. **Kenny N. Kennewurf C.R., Whitmore D.H.** Optical absorption coefcients of vanadium pentoxide single crystals [Journal] // J. Phys. Chem. Solids. - 1966. - Vol. 27. - pp. 1237–1246.

52. **Kessler V.G.** The chemistry behind the sol-gel synthesis of complex oxide, nanoparticles for bio-imaging applications [Journal] // J. Solgel Sci. Technol. - 2009. - Vol. 51. - p. 264.

53. **Khan H. Berk D.** Sol–gel synthesized vanadium doped TiO_2 photocatalyst: physicochemical properties [Journal] // J. Sol-Gel Sci. Technol.. - 2013. - Vol. 68. - pp. 180-192.

54. **Khan M. Song Y., Chen N., Cao W.** Effect of V doping concentration on the electronic structure, optical and photocatalytic properties of nano-sized V-doped anatase TiO_2 [Journal] // Material Chemistry and Physics. - 2013. - Vol. 142(1). - pp. 148-153.

55. **Konstantoinou Ioannis K. and Albanis Triantafyllos A.** TiO_2-assisted photocatalytic degradation of azo dyes in aqueous solution: Kinetic and mechanistic investigations: A review [Journal] // Applied Catalysis B: Environmental. - 2004. - 1 : Vol. 49. - pp. 1-14.

56. **Kosuge K.** The phase diagram and phase transition of the V_2O_3–V_2O_5, system [Journal] // Journal of Physics and Chemistry of Solids. - 1967. - 8 : Vol. 28. - pp. 1613-1621.

57. **Kuroda N. Fan H.Y.** Raman scattering and phase transitions of V_2O_3 [Journal] // Phys. Rev., B. - 1977. - Vol. 16. - p. 5003.

58. **Labidi S.** Elaboration des nanoparticules d'oxyde de zirconium par voie sol-gel: Mise en forme et application pour la synthèse de biodiesel [Journal] // Thesis. - 2015.

59. **Labidi S. Jia Z., Ben Amar M., Chhor K., Kanaev A.** Nucleation and growth kinetics of zirconium-oxo-alkoxy nanoparticles [Journal] // Physical Chemistry Chemical Physics. - 2015. - Vol. 17. - pp. 2651-2659.

60. **LaMer V. K. R. H. Dinegar** Theory, Production and Mechanism of Formation of Monodispersed Hydrosols [Journal] // J. Am. Chem. Soc. - 1950. - 11 : Vol. 72. - pp. 4847-4854.

61. **Le Roy D. Valloppilly S., Skomski R., Liou S.-H., Sellmyer D. J.** Magnetism and structure of anatase (Ti_1–xVx)O2 films. [Journal] // J. Appl. Phys.. - 2012. - Vol. 111. - p. 07C118.

62. **Lee S. Meyer T. L., Sohn C., Lee D., Nichols J., Lee D., Ambrose Seo S. S., Freeland J. W., Noh T. W., Lee H. N.** Electronic structure and insulating gap in epitaxial VO_2 polymorphs [Journal] // APL Materials. - 2015. - Vol. 3. - p. 126109.

63. **Li K. T. Toor H. L.** Chemical indicators as mixing probes. A possible way to measure micromixing simply [Journal] // Ind. Eng. Chem. Fundamen. - 1986. - 4 : Vol. 25. - pp. 719-723.

64. **Lin W-C. Lin Y-J.** Effect of vanadium(IV)-doping on the visible light-induced catalytic activity of titanium [Journal] // Environ. Eng. Sci. - 2012. - Vol. 29. - pp. 447-452.

65. **Liu B. Wang X., Cai., Wen L., Song Y., Zhao X.** Low temperature fabrication of V-doped TiO_2 nanoparticles, structure and photocatalytic studies [Journal] // J. Hazard. Mater. - 2009. - Vols. 169(1-3). - pp. 1112-1118.

66. **Liu S. Xie T., Chen Z., Wu J.** Highly active V–TiO_2 for photocatalytic degradation of methyl orange [Journal] // Appl. Surf. Sci.. - 2009. - Vol. 255. - pp. 8587-8592.

67. **Livage J. Henry M., Sanchez C.** Sol-gel chemistry of transition metal oxides [Journal] // Progress in Solid State Chemistry. - 1988. - 4 : Vol. 18. - pp. 259-341.

68. **Marchisio D. L. Rivautella L., Barresi A. A.** Design and scale-up of chemical reactors for nanoparticle precipitation [Journal] // Aiche Journal. - 2006. - 5 : Vol. 52. - pp. 1877-1887.

69. **Mattheiss L. F.** Band properties of metallic corundum-phase V_2O_3 [Journal] // J. Phys.: Condens. Matter. - 1994. - Vol. 6. - p. 6477.

70. **Meramo S. I. Bonfante-Alvarez H., Avila-Montiel G. D., Herrera-Barros A, Gonzales-Delgado A. D.** Environmental assessement of a large-scale production of TiO_2 nanoparticles via green chemistry [Journal] // Chem. Eng. Trans.. - 2018. - Vol. 70. - pp. 1063-1068.

71. **Miller H. Rigelhof F., Marquart L., Prakash A., Kanter M.** Antioxidant Content of Whole Grain Breakfast Cereals, Fruits and Vegetables [Journal] // Journal of the American College of Nutrition. - 2000. - 3 : Vol. 19. - pp. 312S-319S.

72. **Min C. Hyenmi C., Wonyong C., Yoon J.** Linear correlation between inactivation of E-coli and OH radical concentration in TiO_2 photocatalytic disinfection [Journal] // Water Research. - 2004. - 4 : Vol. 38. - pp. 1069-1077.

73. **Moosavi F.** Développement de matériaux avancés pour le traitement de polluants pharmaceutiques dans les eaux par photo catalyse solaire [Journal] // Thesis. - Planned on October 2022.

74. **Mousumi S.** Intechopen.com [Online]. - Nanocomposite Materials, June 2020. - https://www.intechopen.com/books/nanotechnology-and-the-environment/nanocomposite-materials.

75. **Nguyen T. B. Hwang M. J., Ryu K. S.** High adsorption capacity of V-doped TiO_2 for decolorization of methylene blue [Journal] // Appl. Surf. Sci.. - 2012. - 19 : Vol. 258. - pp. 7299-7305.

76. **Oualha K. Ben Amar M., Michau A., Kanaev A.** Observation of cavitation in exocentric T-mixer [Journal] // Chemical Engineering Journal. - 2017. - C : Vol. 321. - pp. 146-150.

77. **Patila S. S. Shedbalkar U. U., Truskewycz A., Chopade B. A., Ball A. S.** Nanoparticles for environmental clean-up: A review of potential risks and emerging solutions [Journal] // Environmental Technology & Innovation. - 2016. - Vol. 5. - pp. 10-21.

78. **Pecora R.** Dynamic Light Scattering Measurement of Nanometer Particles in Liquids [Journal] // Journal of Nanoparticle Research. - 2000. - Vol. 2. - pp. 123-131.

79. **Pham V.-H. Quan D. H., Manh N. T., Ngoc Minh V. T., Thang C. X., Tam P. D., Van Thiet D., Van H. N.** Microstructure and luminescence of VO_2 (B) nanoparticle synthesis by hydrothermal method [Journal] // Green Processing and Synthesis. - 2019. - 1 : Vol. 8.

80. **Pierre A. C.** Introduction to Sol-Gel Processing [Book]. - Boston : Kluwer Int. Ser. in Sol-Gel Processing: Technology and Applications, 1998.

81. **Pike H. Z. Cummins E. R.** [Book Section] // Photon Correlation and Light Beating Spectroscopy. - [s.l.] : Springer, 1974.

82. **Pohorecki R. Baldyga J.** New model of micromixing in chemical reactors. 2. Application to a stirred tank reactor [Journal] // Ind. Eng. Chem. Fundamen. - 1983. - 4 : Vol. 22. - pp. 398-405.

83. **Ramimoghadam D. Bagheri S., Abd Hamid S. B.** Biotemplated synthesis of anatase titanium dioxide nanoparticles via lignocellulosic waste material [Journal] // Biomed Res. Int.. - 2014. - Vol. 2014. - p. 205636.

84. **Rempel D. A. Davydov A. A.** Refinement of the V-O phase diagram in the range 25–50 at % oxygen [Journal] // Inorganic Materials. - 2009. - Vol. 45. - pp. 47-54.

85. **Ren F. Li H., Wang Y., Yang J.** Enhanced photocatalytic oxidation of propylene over V-doped TiO_2 photocatalyst: Reaction mechanism between V5+ and single-electron-trapped oxygen vacancy [Journal] // Appl. Catal. B: Environmental. - 2015. - Vols. 176-177. - pp. 160-172.

86. **Reyes-Coronado D. Rodríguez-Gattorno G., Espinosa-Pesqueira M. E., Cab C., de Coss R., Oskam G.** Phase-pure TiO_2 nanoparticles: anatase, brookite and rutile [Journal] // Nanotechnology. - 2008. - 14 : Vol. 19. - p. 145605.

87. **Rezaee M. Khoie S. M. M., Liu K. H.** The role of brookite in mechanical activation of anatase-to-rutile transformation of nanocrystalline TiO_2: An XRD and Raman spectroscopy investigation [Journal] // CrystEngComm. - 2011. - Vol. 13. - pp. 5055-5061.

88. **Rietveld H. M.** A profile refinement method for nuclear and magnetic structures [Journal] // J. Appl. Crystallogr. - 1969. - 2 : Vol. 2. - pp. 65-71.

89. **Rivallin M. Benmami M., Gaunand A., Kanaev A.** Temperature dependence of the titanium oxide sols precipitation kinetics in the sol-gel process [Journal] // Chemical Physics Letters. - 2004. - Vol. 398. - pp. 157-162.

90. **Rivallin M. Benmami M., Kanaev A., Gaunand A.** Sol-gel reactor with rapid micromixing: modelling and measurements of titanium oxide nano-particles growth [Journal] // Chem. Eng. Res. Des.. - 2005. - Vol. 81 (A1). - pp. 67-74.

91. **Rodríguez-Carvajal J.** Recent advances in magnetic structure determination by neutron powder diffraction [Journal] // Phys. B Condens. Matter.. - 1993. - Vol. 192. - pp. 55-69.

92. **Rossi G. Pasquini L., Catone D., Piccioni A., Patelli N., Paladini A., Molinari A., Caramori S., O'Keeffe P., Boscherini F.** Charge carrier dynamics and visible light photocatalysis in vanadium-doped TiO_2 nanoparticles [Journal] // Appl. Catal. B-Environmental. - 2018. - Vol. 237. - pp. 603-612.

93. **Sanchez Mendez M. Cheng K., Traore M., Ben Amar M., Kanaev A.** Elaboration of mixed oxide photocatalysts [Journal] // Chem. Eng. Trans. - 2019. - Vol. 74. - pp. 433-438.

94. **Sanchez Mendez M. Jia Z., Traore M., Ben Amar M., Nikravech M., Kanaev A.** Nucleation and growth of mixed vanadium-titanium oxo-alkoxy nanoparticles in sol-gel synthesis [Journal] // Colloids and Surfaces A: Physicochemical and Engineering Aspects. - 2021. - Vol. 610. - p. 125636.

95. **Schneider J. Matsuoka M., Takeuchi M., Zhang J., Horiuchi Y., Anpo M., Bahnemann D. W.** Understanding TiO_2 photocatalysis: Mechanisms and materials [Journal] // Chem. Rev.. - 2014. - Vol. 114. - pp. 9919–9986.

96. **Schwarzer H. C. Peukert W.** Combined experimental/numerical study on the precipitation of nanoparticles [Journal] // Aiche Journal. - 2004. - 12 : Vol. 50. - pp. 3234-3247.

97. **Schwarzer H. C. Schwertfirm F., Manhart M., Schmid H. J., Peukert W.** Predictive simulation of nanoparticle precipitation based on the population balance equation [Journal] // Chemical Engineering Science. - 2006. - 1 : Vol. 61. - pp. 167-181.

98. **Shao G. N. Imran S.M., Jeon S. J., Kang S. J., Haider S.M., Kim H. T.** Sol–gel synthesis of vanadium doped titania: Effect of the synthetic routes and investigation of their photocatalytic properties in the presence of natural sunlight [Journal] // App. Surf. Sci.. - 2015. - Vol. 351. - pp. 1213-1223.

99. **Shvets P. Dikaya O., Maksimova K., Goikhman A.** A review of Raman spectroscopy of vanadium oxides [Journal] // Journal of Raman Spectroscopy. - 2019. - 8 : Vol. 50. - pp. 1226-1244.

100. **Soloviev A. Ivanov D., Tufeu R., Kanaev A. V.** Nanoparticle growth during the induction period of the sol-gel process [Journal] // Journal of Materials Science Letters. - 2001. - Vol. 20. - pp. 905-906.

101. **Soloviev A. Jensen H., Søgaard E. G., Kanaev A. V.** Aggregation kinetics of sol-gel process based on titanium tetraisopropoxide [Journal] // Journal of Materials Science. - 2003. - Vol. 38. - pp. 3315-3318.

102. **Soloviev A.** PhD thesis [Book]. - Villetaneuse, France : University Paris 13, 2000.

103. **Soloviev A. Tufeu R., Sanchez C., Kanaev A. V.** Nucleation Stage in the Ti(OPri)4 Sol-Gel Process [Journal] // J. Phys. Chem. B. - 2001. - 19 : Vol. 105. - pp. 4175-4180.

104. **Son M. Lee J., Park J., Shin J., Choi G., Jung S., Lee W., Kim S., Park S., Hwang H.** Excellent Selector Characteristics of Nanoscale VO_2 for High-Density Bipolar ReRAM Applications [Journal] // IEEE Electron Device Letters. - 2011. - 11 : Vol. 32. - p. 1579.

105. **Steunou N. Kickelbick G., Boubekeur K., Sanchez C.** A new polyoxo–alkoxo titanium cluster of the Keggin family: synthesis and characterization by X-ray diffraction and NMR spectroscopy [Journal] // J. Chem. Soc., Dalton Trans.. - 1999. - 21. - pp. 3653-3655.

106. **Stoller M. Vuppala S., Cheng K., Traore M., Marchetti A., Kanaev A., Chiavola A.** Design of novel equipment capable to quickly produce efficient nanomaterials for use in environmental and sanitary emergencies [Journal] // Chem. Eng. Trans.. - 2019. - Vol. 73. - pp. 187-192.

107. **Takashi T. Tetsuro M.** Single-molecule fluorescence imaging of TiO_2 photocatalytic reactions [Journal] // American Chemical Society. - 2009. - 25 : Vol. 14. - pp. 7791-7802.

108. **Tieng S. Brinza O., Chhor K., Kanaev A.** Nucleation and fractal growth of zirconium oxo-alkoxy nanoparticles at the induction stage of sol–gel process [Journal] // Journal of Sol-Gel Science and Technology. - 2012. - Vol. 64. - pp. 145-148.

109. **Trifiro F.** The chemistry of oxidation catalysts based on mixed oxides [Journal] // Catal. Today. - 1998. - 1-3 : Vol. 41. - pp. 21-35.

110. **Vennila R. Kamaraj P., Arthanareeswari M., Deepika J.** Evaluation of The Biological Activities of Ag Doped Bismuth Oxide Nanoparticles [Journal] // Indian Journal of Applied Research. - 2014. - 6 : Vol. 4. - pp. 53-56.

111. **Verrelli R. Black A.P., Pattanathummasid C., Tchitchekova D.S., Ponrouch A., Oró-Solé J., Frontera C., Bardé F., Rozierb P., Palacín M.R.** On the strange case of divalent ions intercalation in V_2O_5 [Journal] // Journal of Power Sources. - 2018. - Vol. 407. - pp. 162-172.

112. **Vinu R. Madras G.** Photocatalytic Degradation of Water Pollutants Using Nano-TiO_2 [Journal] // Energy Efficiency and Renewable Energy Through Nanotechnology. Green Energy and Technology Springer London. - 2011. - Vol. 33. - pp. 625-677.

113. **Wachs I.E. Chen Y., Jehng J.-M., Briand L.E., Tanaka T.** Molecular structure and reactivity of the Group V metal oxides [Journal] // Catal. Today. - 2003. - Vol. 78. - p. p. 13.

114. **Wang L. Fox R. O.** Comparison of micromixing models for CFD simulation of nanoparticle formation [Journal] // Aiche Journal. - 2004. - 9 : Vol. 50. - pp. 2217-2232.

115. **Yang Y. Mao H.,Chen H.-L., Selleby M.** An assessment of the Ti-V-O system [Journal] // J. Alloys Compounds. - 2017. - Vol. 722. - pp. 365-374.

116. **Young R. A.** The Rietveld Method [Book]. - [s.l.] : Oxford University Press, 1995.

117. **Zaleska A.** Doped-TiO_2: A review [Journal] // Recent Patents Eng. - 2008. - Vol. 2. - pp. 157-164.

118. **Zhang H. Chen G., Bahnemann W. D.** Photoelectrocatalytic materials for environmental applications [Journal] // Journal of Materials Chemistry. - 2009. - 19 : Vol. 29. - pp. 5089-5121.

119. **Zhang Z. Chen J., Guo Y., Robertson J.** Band alignment calculation of dielectric films on VO_2 [Journal] // Microelectronic Engineering. - 2019. - Vol. 216. - p. 111057.

120. **Zhang Z. Shao C., Zhang L., Li X., Liu Y.** Electrospun nanofibers of V-doped TiO_2 with high photocatalytic activity [Journal] // J. Colloid Interface Sci.. - 2010. - 1 : Vol. 351. - pp. 57-62.

121. **Zhou W. Liu Q., Zhu Z., Zhang J.,** Preparation and properties of vanadium-doped TiO_2 photocatalysts [Journal] // J. Phys. D.. - 2010. - Vol. 43. - p. 035301.

Title:

Elaboration of mixed metal oxide nanoparticles for applications in photocatalysis.

Abstract:

The PhD study is focused on synthesis of mixed vanadium-titanium oxo-alkoxy (VTOA) nanoparticles with size and composition control, preparation of photocatalytic coatings of these nanoparticles and study of their photocatalytic properties. The synthesis was carried out via sol-gel method in a laboratory chemical reactor with ultra-rapid micromixing. The particles size was monitored in-situ using dynamic/static light scattering methods. At relatively low vanadium content ≤10 mol% the analysis showed the nucleation of mixed VTOA particles of 2.1 nm radius. We showed that titanium oxo-alkoxy (TOA) species appear first and serve to be centers of attraction for hydrolyzed vanadium oxo-alkoxy (VOA) species at the nucleation stage. In contrast, at high vanadium content >20 mol%, VOA species percolate by imprisoning sub-nucleus TOA species prohibiting the nanoparticles appearance: this is connected to stronger hydrolysis and weaker condensation abilities of VOA species compared to TOA. The heat treatment of VTOA powders was studied in the range of temperatures 300-1000 °C. The TGA-TDA analysis showed a significant dependence of the anatase phase onset temperature on vanadium content, which supports perfect insertion of V atoms into host TiO_2 matrix. The XRD and Raman analyses evidenced the appearance of orthorhombic α-V_2O_5, which could indicate the V-TiO_2 material segregation phenomenon. The Rietveld analysis of XRD patterns evidenced no significant deviation of the anatase structure parameters. The photocatalytic nanocoating on glass beads were prepared by liquid colloid deposition of VTOA nanoparticles followed by their appropriate heat treatment (450 °C, 4 h). The photocatalytic activity was studied under illuminations with UVA (λ=365 nm, 8 W) and visible (λ>390 nm, 50 W) lamps: the methylene blue decomposition kinetics was monitored. The photolytic and photocatalytic processes were distinguished. The best performance under UVA and Visible light illuminations showed V-TiO_2 photocatalysts with respectively 2 mol% and 10 mol% vanadium.

Keywords:

Vanadium-titanium oxo-alkoxy nanoparticles, rapid micromixing reactor, nucleation-growth process, in situ size measurements, anatase V-TiO_2 nanocoatings, photocatalysis, UVA / visible lamp illumination

Titre :

Elaboration de nanoparticules d'oxydes métalliques mixtes pour des applications en photocatalyse

Résumé

Ce travail de thèse porte sur la synthèse de nanoparticules d'oxo-alcoxy mixtes de vanadium et de titane (VTOA) de taille et de composition chimique contrôlées, la préparation de dépôts (film mince) photocatalytiques à partir de ces nanoparticules et l'étude de leurs propriétés photocatalytiques. La synthèse a été réalisée par la méthode sol-gel dans un réacteur chimique de laboratoire à micromélange ultra-rapide. La taille des particules a été contrôlée *in situ* par des méthodes de diffusion dynamique/statique de la lumière. À une teneur relativement faible en vanadium ≤10 % molaire, l'analyse a montré la nucléation de particules mixtes VTOA de 2,1 nm de rayon. Nous avons montré que les espèces oxo-alcoxy de titane (TOA) apparaissent en premier et servent de centres d'attraction pour les espèces oxo-alcoxy de vanadium (VOA) hydrolysées au stade de la nucléation. En revanche, à une teneur élevée en vanadium >20 mol%, les espèces VOA percolent en emprisonnant les *subnuclei* de TOA, empêchant ainsi l'apparition de nanoparticules : ceci est lié aux capacités d'hydrolyse plus fortes et de condensation plus faibles des espèces VOA par rapport aux TOA. Le traitement thermique des poudres de VTOA a été étudié dans la gamme de températures 300-1000 °C. L'analyse ATG-ATD a montré une dépendance significative de la température d'apparition de la phase anatase par rapport à la teneur en vanadium, ce qui soutient l'insertion parfaite des atomes de Vanadium dans la matrice hôte TiO_2. Les analyses DRX et Raman ont mis en évidence l'apparition de la phase α-V_2O_5 orthorhombique, ce qui pourrait indiquer un phénomène de ségrégation du matériau V-TiO_2. L'analyse Rietveld des diffractogrammes n'a mis en évidence aucune déviation significative des paramètres structuraux de l'anatase. Les nano-films photocatalytiques sur les billes de verre ont été préparés par une méthode de déposition en phase liquide à partir des suspensions colloïdales de nanoparticules VTOA, suivi par un traitement thermique approprié (450 °C, 4 h). L'activité photocatalytique des dépôts a été étudiée dans l'UV et dans le visible sous illumination par une lampe UVA (=365 nm, 8 W) et visible (>390 nm, 50 W) : la cinétique de décomposition du bleu de méthylène a été suivie. Les processus photolytiques et photocatalytiques ont été distingués. Les meilleures performances sous les éclairages UVA et Visible ont été montrées pour des photocatalyseurs V-TiO_2 avec respectivement 2 mol% et 10 mol% de vanadium.

Mots Clés

Nanoparticules d'oxo-alcoxy de vanadium-titane, réacteur à micromélange rapide, processus de nucléation-croissance, mesures de taille in situ, nano-films de V-TiO_2 anatase, photocatalyse, illumination par lampe UVA / visible